Università Politecnica delle Marche
Scuola di Dottorato di Ricerca in Scienze dell'Ingegneria
Corso di Dottorato in Ingegneria Civile, Ambientale, Edile e Architettura

---

Observation and modeling of the estuarine and coastal hydro-morphodynamics: the Misa River case study

Ph.D. Dissertation of:
Agnese Baldoni

Supervisor:
Prof. Maurizio Brocchini

Ph.D. Course coordinator:
Prof. Francesco Fatone

XXXV edition - New series

Università Politecnica delle Marche
Dipartimento di Ingegneria Civile, Edile e Architettura (DICEA)
Via Brecce Bianche - 60131 - Ancona, Italy

Acknowledgements

I would like to acknowledge my advisor Prof. Maurizio Brocchini, who assisted and guided me throughout this experience. I sincerely thank also Luciano Soldini, Pierluigi Penna, Joseph Calantoni and Luca Parlagreco for contributing to my research project in terms of data sharing and supervision of the work.

I am especially grateful to Eleonora Perugini for her patience, help and knowledge sharing since the first day of my PhD.

I am deeply grateful to Fondazione Cariverona for their financial support through the 2019 PhD scholarship "OSservazione e MODellazione dell'idromorfoDINamica estuarina e costiera (OSMODIN)" (2019.0294 - D.R. n. 603 of May 28, 2019). The financial support from the Office of Naval Research Global (UK) MORSE Project (Research Grant N62909-17-1-2148) is also gratefully acknowledged. I wish to extend my sincere thanks to all the colleagues of the Hydraulic and Maritime Constructions area of the DICEA for their availability to offer me assistance whenever I needed it.

My sincere thanks to my parents, my sister, my whole family and my friends for believing in me and for supporting me in this important experience. Finally, my heartful gratitude goes to Giacomo for always being by my side, encouraging me to believe in myself.

Abstract

The present thesis studies phenomena of importance for the estuarine dynamics of small-scale river systems, characterized by torrential regimes, flowing into micro-tidal environments. Specific focus is on the Misa River estuary (Senigallia, Italy) as representative of such sites. The complex morphodynamics of the site, in particular the long-term evolution of an inner mouth bar and the generation and spreading of the river plume, was studied by integrating different sources of information. Video-monitoring products, allowing to capture the dynamical evolution of the estuary, were used to retrieve some features of the investigated phenomena that were correlated with the forcing acting at the river mouth in order to understand the physical mechanisms controlling the observed dynamics. The outcomes of such correlation work showed the complexity of the events, characterized by the interaction of multiple forces acting in a combined way. Therefore, a numerical model, Delft3D, was used to distinguish the role of each forcing, since it provides the possibility of switching off some processes, focusing on one single forcing at a time. Furthermore, the study of the river plume was completed through the implementation of some Particle Tracking Velocimetry analyses.

Due to the reduced precipitation and discharges of the recent years, a persistent inner mouth bar formed inside the most downriver stretch of the highly engineered Misa River estuary. The bar size reached, at times, the whole width of the river section, causing concern about the inhibition of the fluxes of water and sediments from the river to the sea. The study showed that the main forces affecting the migration of the bar along the channel are the river discharge and the waves. Moderate river discharges (1-year return period) cause downriver bar migrations larger than the upriver migrations triggered by severe sea storms (10-years return period). Such result highlights the dominance of river discharge-induced sediment expulsion out of the river mouth over the upriver transport by the waves. Therefore, the presence of an inner mouth bar does not impede the sediment outflow to sea, but it can only obstacle the outflow during low-flow conditions. Considering this, the evolution of the bar should be monitored to programme the channel maintenance in periods when the natural dredging of the riverbed cannot be done by the river itself.

The dominant role of the river also emerged from the study of the plume generation and transport mechanisms. Notwithstanding its small dimension, the Misa River exports large quantities of sediment to sea. The river plume flowing out of the estuary also transports substances other than sediment, such as pollutants and nutrients, which spread along the coast, possibly reaching the surrounding beaches. Results showed that the river discharge generates the densest and most extended plumes, but also waves can stir, suspend, and drag plume sediments. The spreading of the plume in the alongshore direction is greatly affected by the wind that transports the sediments mainly towards the south-east, reaching distances up to some kilometers from the river mouth. This means that the sediments originating from the river basin likely contribute to some nourishment of the beaches to the south of the Misa River estuary. Moreover, a power law linking the plume offshore extension with the plume velocity components was also found. It reveals that the plume offshore extension is directly proportional to the plume alongriver velocity, mainly determined by the river speed, while it decreases because of the action of the transport mechanisms that contribute to the alongshore plume velocity.

Contents

List of symbols

Δ	Submerged specific gravity
δ	Normalized entrainment velocity
δ_i	Scale parameter for the Gaussian filter
Δ_r	Wave-induced ripple height
Δ_ρ	Difference between the river mouth density and the offshore water density
Δ_{bar}	Non-dimesional bar displacement
ϵ_s	Sediment eddy diffusivity
η	Water level with respect to the mean sea level
γ	Breaker index
γ_b	Critical value of the breaker index
λ	Wavelength
ν	Kinematic viscosity of water
ν_H	Horizontal eddy viscosity
ρ	Water density at the river mouth
ρ_0	Offshore water density
ρ_s	Sediment density
ρ_w	Water density
σ	Frequency
τ	Bed shear stress
$\tau_{cr,d}$	Critical deposition shear stress
$\tau_{cr,e}$	Critical erosion shear stress
τ_{cr}	Critical shear stress for bedload
τ_{wc}	Maximum bed shear stress due to current and waves
θ	Direction
θ_{cr}	Shileds parameter
a	Wave amplitude
a_s	van Rijn reference height
B	River width
C	Chézy coefficient

c	Concentration
c_b	Average sediment concentration in the near bottom computational layer
c_f	Friction factor
c_w	Phase speed
c_σ	Propagation velocity in σ-direction
c_θ	Propagation velocity in θ-direction
c_{g0}	Offshore group velocity
c_{kmx}	Average concentration through the bottom of the reference layer (kmx-layer)
c_{ref}	Reference concentration for the Northern Adriatic environment
D	Deposition flux for cohesive sediment
D^*	Non-dimensional grain size
d_b	Depth at breaking
D_{50}	Sediment median diameter
D_{nc}	Deposition flux for non-cohesive sediment
E	Erosion flux for cohesive sediment
e	Plume offshore extension
E_{nc}	Erosion flux for non-cohesive sediment
F_s	Wave induced force per unit area
g	Gravity acceleration
g'	Reduced gravity
H	Wave height
h	Water depth
H_0	Offshore wave height
H_b	Height of breaking waves
h_p	Plume depth at the river mouth
H_s	Wave significant height
I_q	Discharge index
k	Wave number
k_s	Current-related effective roughness height
L	Distance between the model river section and the river mouth
L_C	Cross-shore extent of the channel
L_{NF}	Near-field plume length
L_{SZ}	Surf zone width
M	Erosion parameter
M_e	Excess sediment mobility number
M_s	Sediment mobility number due to waves and currents

N Action density spectrum

n Manning coefficient

R Fluvial dominance ratio

r Correlation coefficient

R^2 Determination coefficient

Re_B "River mouth" Reynolds number

S Source term

$S(\tau_{wc}, \tau_{cr,d})$ Step function for deposition

$S(\tau_{wc}, \tau_{cr,e})$ Step function for erosion

S_b Magnitude of the bedload transport

S_n Stability number

S_w Wave stress ratio

T Wave period

t Time

T_p Wave peak period

U River depth-averaged velocity

U_0 Cross section-averaged velocity at the river mouth

u_{plume} Plume surface velocity

u_{river} River contribution to the plume surface velocity

u_{waves} Waves contribution to the plume surface velocity

u_{wind} Wind contribution to the plume surface velocity

v_{mod} Modeled, depth-averaged velocity

$v_{obs,1.3}$ Velocity measured during the EsCoSed field experiment, projected in the along-river direction

$v_{obs,drift}$ Mean velocity over the total water depth, computed from extrapolated, vertical velocity profiles (EsCoSed)

v_{obs} Measured velocity (EsCoSed), modified to be compared to the modeled, depth-averaged velocity

$v_{surface}$ River surface velocity

w_e Entrainment velocity

w_s Hindered settling velocity

y_{start} Initial bar location

(α, β) Calibration factors for the sediment rating curve

(C_u, C_v) Chézy coefficients in x- and y-directions

(c_x, c_y) Propagation velocities in x- and y-directions

(M_x, M_y) External source/sink of momentum in x- and y-directions

(u, v) Flow velocity components in x- and y-directions

$(u_{plume,x}, u_{plume,y})$ Alongriver and alongshore components of u_{plume}

$(u_{waves,x}, u_{waves,y})$ Alongriver and alongshore components of u_{waves}

$(u_{wind,x}, u_{wind,y})$ Alongriver and alongshore components of u_{wind}

(x, y, z) Cartesian coordinates

IG Infragravity

MR Misa River

MRE Misa River Estuary

PTV Particle Tracking Velocimetry

Q River discharge

R Identifies river discharge-driven events

RD River Discharge

RTR Relative tidal range

SGS Sena Gallica Speculator

SSC Suspended sediment concentration

W Identifies wave-driven events

List of Figures

List of Tables

Chapter 1

Introduction

1.1 Objectives and thesis outline

The overall goal of this work is to improve the knowledge of the hydro-morphodynamics of a micro-tidal estuary. The study area is the mouth of the Misa River (MR hereinafter), that originates from the Apennines and debouches into the Adriatic Sea after flowing through the city of Senigallia (Marche, Italy). Such site is representative of those small-scale, micro-tidal river systems characterized by torrential regimes and large sediment transport despite their small dimension.

An estuary is a complex area where the interaction between the sea forces (wave and tide) and the river discharge takes place, affecting different hydro-morphodynamical processes. Two main phenomena, evolving under such interplay of forces, have been investigated:

1. the behavior of an inner mouth bar, persistently emerging in the final stretch of the MR during the last years;

2. the formation and following alongshore spreading of the MR plume.

The complexity of the studied processes due to the combined action of multiple factors has made it necessary to rely on different sources of data. Optical images and videos from shore-based stations are useful to observe the dynamical evolution of both the bar and the plume, which could develop on small timescales (hours to days). They also allow to have continuous data even during bed meteorological conditions at a moderate cost. Field data are essential for the correlation of the information derived from the video-monitoring products with the estuarine forces. They were provided both by the MORSE monitoring system[1], specifically developed for observing the Misa River Estuary (MRE hereinafter) and managed by the Università Politecnica delle Marche, and by some instruments managed by the Civil Protection of the Marche Region, the National Research Council (CNR) and the Italian Institute for Environmental Protection and Research (ISPRA). Notwithstanding the importance of such data, the large number of factors involved in the studied processes makes the role of each force difficult to understand. The need to separate the single contributions leads to the use of numerical models, capable of simulating different scenarios activating the wanted forcing terms.

The thesis is organized in six chapters.

Chapter 1 (*Introduction*) introduces the main aspects and gives a literature overview of the investigated processes, with focus on the novelties introduced by this study.

Chapter 2 (*The study area*) describes the main hydrodynamic features and the morphological characteristics of the observed area. A description of the field data used in the study is also given in the second section of the chapter.

Chapter 3 (*Study of the MR mouth bar*) concerns the analysis of the MR inner mouth bar evolution. Section 3.1 presents the code used to identify the bar on the images and obtain its geometric characteristics. Section 3.2 introduces the Delft3D

[1] http://www.morse.univpm.it

numerical solver and describes the set of simulations performed. The outcomes of the correlation between the image analysis and the field data are given in Section 3.3, while Section 3.4 reports on the simulation results, after giving some model calibration results.

Chapter 4 (*Study of the MR plume*) deals with the investigation of the mechanisms responsible for the MR plume generation and transport. Section 4.1 describes the processing of the video-monitoring products, included the Particle Tracking Velocimetry (PTV) analyses. Section 4.2 presents the implemented numerical model and simulations, whose results and calibration are exposed in Section 4.4. Section 4.3 gives the results derived from observations, while PTV outcomes are summarized in Section 4.5.

Chapters 5 (*Discussion*) and 6 (*Conclusions*) provide a discussion of the results, some final considerations, general conclusions and suggests some possible future development.

1.2 River mouth bars

When a river discharge debouches into the sea, it spreads, decelerates, and deposits its sediment load. The resulting morphological patterns are determined by the combination of river-mouth processes that involve the interaction between riverine and marine waters. Wright [93] provides an excellent review of river-mouth variability by considering it as a result of contributions from primary and modifying forces.

The primary forces include i) inertia, ii) bed friction and iii) buoyancy, all driven by the river outflow. Lunate bars form due to inertial conditions occurring when an unbounded jet debouches into a deep basin; in friction-dominated flows, characterized by a large stability number, the effluent rapidly spreads with consequent diverging levee formation around a central mouth bar; where buoyancy is the dominant force, the effluent spreads and thins, allowing the progradation of straight subaqueous levees and infrequent bifurcations. Pronounced levees and elongated channels are also formed for low stability numbers [9]. Also, it has been shown that lateral advection and diffusion of suspended sediment are directly proportional to jet potential vorticity; large sediment potential vorticity fosters levee deposition (channel elongation in the sea), while small potential vorticity encourages mouth bar deposition [19].

Primary forces can be modified to varying degrees by tides and waves. Waves can either suppress mouth bar formation because of their intense seabed erosion and longshore transport or promote mouth bar growth [18]. Typically, large waves are associated with single-channel deltas without bifurcation, while small waves favor bar formation. Nardin et al. [58] showed that, in sheltered bays, locally generated waves ($H_s < 1$ m, $T < 10$ s), have two distinct effects on mouth bar evolution. First, they increase jet spreading, generating a wider deposition of sediment closer to the river mouth due to the rapid seaward deceleration of the effluent. Second, the shear stress produced by wave orbital velocities at the bottom adds to the current shear stress, this triggering bed load transport and sediment resuspension. Moreover, waves play also a role on sediment redistribution and reworking, especially during periods of low river discharges (a. o., [1, 4]).

The other modifying force is the tide (a.o., [12, 28]). In tide-dominated systems a transition zone exists where the interaction between the river flow, seaward decelerating, and the tidal currents, seaward increasing, takes place. The inner part of the transition zone is characterized by the dominance of river currents and consequent downriver net sediment transport; on the contrary, the prevalence of the tidal force in the outer portion of the transition zone causes a net landward transport of sediment. As a result, these transport trends develop a bedload convergence within the middle portion of all estuaries and in the distributary-mouth-bar area of deltas [12].

Previous studies largely focus on the formation of a typical mouth bar: sediments deposited by flow expansion out of the river mouth at a distance depending from the jet momentum flux [17, 18]. Such distance is between zero and two channel widths for stable jets and higher for unstable jets. However, the scenario of an inner mouth bar in a micro-tidal environment subject to strong wave action has not been extensively studied. The present work has been motivated by some recent detailed

Figure 1.1: Image of the bar formed inside the mouth of the Misa River.

video monitoring observations of the riverbed morphology at the MR (Senigallia, Italy), showing the presence of a persistent inner mouth bar (Figure 1.1). The bar is largely constituted by coarse sediments (very coarse sand and gravel) lying over a layer of much finer muddy sediments (silt and clay). Typically, the MR mouth bar evolves over an annual cycle characterized by i) the expulsion of sediment out of the river mouth because of the intense rain-driven riverine water jet, usually in winter, and ii) sediment accumulation, typically in summer, because of the weak river currents and continuous action of upriver flows due to waves and modulating tides [8]. Such cyclic behaviour has been modified over the last years due to the reduced precipitations that caused long periods of low river flows. Consequently, the bar started emerging permanently above the mean water level during such periods, also spanning much of the river mouth cross section. The aim of the work is to understand the mechanisms that characterize the evolution of the MR mouth bar.

1.3 River plumes

River plumes are a source of suspended and dissolved river-borne constituents that mix into sea water. Understanding of the structure, dynamics and evolution of river plumes is fundamental to comprehend the land-ocean exchanges. Plumes can be classified following different criteria. Among others, Garvine [24] distinguished between "large-scale" or "small-scale" plumes, respectively when large-scale rotational processes dominate over inertial processes or vice versa. Based on their vertical thickness, plumes have been divided in "surface-advected", i.e. relatively shallow plumes affected by surface dynamics, and "bottom-advected", i.e. plumes extending to the bottom, whose offshore extent and velocity structure are dictated by bottom Ekman dynamics and thermal wind balance [95]. Osadchiev and Zavialov [63] argued that the formation and spreading of river plumes are governed by both "intrinsic characteristics", such as local latitude, topography, morphology, and sediment characteristics, and "external forcing", including river discharge, local wind, tide, coastal circulation, and waves.

Notwithstanding the large amount of suspended sediment that small river plumes supply to the ocean, which represents around 40% of the total sediment influx [54], relatively small attention is paid to their evolution with respect to large and medium-size systems (a. o., [21, 45, 95]). Given their small spatial scale, the relatively low volume of river discharge and the intense mixing with ambient sea, small-scale buoyant plumes evolve in a short time, of hours and days. This contributes to make their spreading patterns different from those typical of large and medium-size rivers and largely influenced by the wind forcing [61]. In fact, the concentration of wind stress in a shallow freshened surface layer causes higher motion velocity and a quicker response of the plume dynamics to variability of wind forcing [64, 89], this resulting in a very energetic short-temporal variability of plume's position, shape, and area [61, 62].

Winds strongly affect also the pathways of sediment flowing in micro-tidal environments, where the tidal effects are negligible, as observed by Kombiadou and Krestenitis [39]. Moreover, the plume variability in micro-tidal sites is influenced by

the topography, the bottom slope and the river discharge [52], found to be linearly correlated with the plume area [42]. In contrast, in macro and meso-tidal environments, largely studied in literature, tides play a dominant role affecting the mixing and the water column stability and, therefore, the horizontal movement and spreading of plumes (a.o., [43, 80, 81]).

Lastly, waves can significantly alter the plume structure by interacting with the river current [77]. In fact, several authors argue that the ratio of the wave-to-outflow momentum fluxes is related to the sediment spreading and determines to which distance the plume can extend [38, 96]. While some recent studies focused on the effect of waves in altering the plume expansion, to the author's knowledge, the role of waves in resuspending riverbed sediment, generating a plume, has found little space in the literature. The present study aims at characterizing the mechanisms responsible for the formation and evolution of river plumes in a site representative of those small-scale, micro-tidal systems that largely contribute to the supply of sediment to the sea. Attention is paid to the role of waves, still not exhaustively understood. Furthermore, a relationship between the extension and the velocity of the plume is researched.

1.4 Techniques for river-mouth analysis

An overview of the techniques that have been used to study the above-mentioned estuarine processes is given here. Traditional "in-situ" surveys provide measurements of a site's topography and bathymetry, allowing to reach precise and detailed information. Two surveys carried out in summertime and wintertime conditions were used by Brocchini et al. [8] to compare the MR mouth morphology during such periods and to relate observations with numerical simulation results. Notwithstanding the high quality of such type of data, they present a major drawback; while they may be executed readily during dry periods, they are inhibited by the adverse conditions present during flood events. Moreover, "in-situ" surveys are quite expensive and, therefore, valuable when performing medium to long-term analyses that require a limited number of surveys to be made. On the other hand, in studies regarding the dynamical and rapid development of morphological features, mainly evolving during riverine floods or sea storms, such measurements are not the most suitable. However, they remain of great importance i) to understand the general behaviour and characteristics of the studied area and ii) as input for numerical models to generate the domain bathymetry and topography.

Numerical models allow one to investigate the river mouth morphodynamics and to test the validity of theoretical and analytical approaches. They represent a powerful tool that should be used in a conscious way and always keeping in mind the physics of the analyzed phenomena, in order to critically interpret the numerical results. One of the greatest advantages of using numerical modeling is the possibility of running a large number of scenarios simplifying the real conditions, this allowing a deeper understanding of the factors involved in the studied process. Among the numerical models, the coupled hydrodynamic-sediment transport model Delft3D [44, 78] is becoming an increasingly applied tool in morphodynamic studies, due to its numerical stability and ease of use compared to other platforms (a. o., [17, 96]. Delft3D has been used by several authors (a.o., [57, 58]) to investigate the morphodynamical effect of the interaction between currents and waves by coupling the hydrodynamic module with the SWAN (Simulating WAves Nearshore) wave module [5]. In this work, Delft3D is used, after some calibrations, to both i) reproduce real-life events to compare with observations and ii) run test cases to distinguish the role of each force involved in the investigated processes.

In the last decades, the use of remote sensing has been largely developed as an alternative to "in-situ" surveys. Even if remote sensing is typically associated with satellites, a number of other solutions is available, from airborne to shore-based sensors, installed on different types of platforms, lighthouses and towers [32]. The advantage of all these sensors is that they can be deployed away from severe marine conditions, thus sampling in each meteorological condition. Furthermore, they can observe a large spatial extent over long durations at a relatively low cost. Among the variety of sensors

and platforms, fixed optical cameras represent one of the best solutions to observe river-mouth processes that evolve rapidly (hours to days). In fact, both the MR bar and plume show a very dynamic evolution, difficult to capture with other widely diffuse remote sensing tools, such as the satellite images. Although they permit synoptic analyses over wide areas and long-time scales (a. o., [41, 82]), they have a limited temporal resolution and fail to provide data when cloud cover is present, commonly after a rainfall. On the contrary, video and images recorded by fixed stations provide data at a higher temporal resolution, appropriate for studying small-scale rapidly varying processes [56, 71]. Moreover, the high-resolution video cameras combined with well-known techniques for image analysis [33, 34, 70] permit the study of both emerged and submerged morphology. Finally, a PTV technique can be applied to the videos to study the hydrodynamics of the river mouth. In the end, the main advantages of fixed cameras are acquisition frequency flexibility, high spatial and temporal resolution, weak climate dependency, and low cost compared with commonly used remote-sensing techniques. On the other hand, their major drawbacks are both the limited field of view and the fact that they operate across the visual band, thus the acquisition is limited to daylight hours and can be disturbed by fog or rain drops on the camera lens.

A strength of the present study is the use of an integrated approach, which blends different sources of data: numerical simulations, video-monitoring products and field data. The analysis of the MR mouth is then carried out by combining the outcomes of multiple techniques, taking advantage of the potential of each of them. The detailed description of the methodology is given in the next chapters.

Chapter 2

The study area

2.1 Regional setting

The study area includes the estuary and the beach surrounding the Misa River, which originates in Arcevia, flows to the northeast, and enters the Middle Adriatic Sea in Senigallia after joining with the Nevola River (Figure 2.1).

The MR has a length of about 45 km and a watershed extension of 383 km^2; the river discharges associated to return periods of 50, 100, 200 years are of about 505, 541, and 591 m^3/s, respectively [48]. To interpret the results discussed in Chapters 3 and 4, the 1-year return period river discharge of 150 m^3/s is also reported here. The river width varies between 20 and 40 m in the last kilometer before reaching the mouth, where the water flows within a fixed engineered channel. Moreover, the final reach of the MR is highly monitored by the MORSE video-monitoring system, this making it comparable to a field-scale laboratory flume.[1]

Like other rivers originating in the Apennine Mountains, despite its small size and moderate discharge, the MR distributes large quantities of sediment because of the ease of erodibility of the brittle and fractured rocks that constitute the Apennine Mountains. This leads to the formation of mouth bars, as in all Adriatic rivers, even with very different geometrical configurations and structural constraints. In fact, the MR mouth is located at the end of two concrete jetties, about 300 m seaward of the shoreline, this generating a non-genuine prodelta region unlike natural estuaries.

The suspended sediment discharge from the MR is estimated to be between $4.7 \cdot 10^8$ kg/yr and $8.4 \cdot 10^8$ kg/yr [23, 54]. Sediment supply consists of limestone, shale, and sandstone. Moreover, the deposition of volcanic ash, transported from the southeast by winds during the Plinian and other volcanic eruptions [72, 79] has enhanced the cohesive nature of the sediments within the MR, by adding an abundant supply of montmorillonite clay minerals (2 - 5 μm in size). Cores of the alluvial layers underlying the town of Senigallia displayed layers of muddy sediments, interspersed with gravel, all of which overlie the bedrock of fractured and faulted mud-, silt- and sandstone [20]. More recently, thick layers of muddy sediments were found in the MR bed surface, with percentage of sand and gravel increasing while approaching the river mouth [8, 16].

The coast of Senigallia is characterized by a very mildly sloping sandy beach, defended by breakwaters to the north of the MR estuary, while part of a natural open coast to the south. The coastline has a NW–SE orientation and faces approximately 40° from the north. The beach is characterized by medium ($D_{50} = 0.25 - 0.5$ mm) to fine ($D_{50} = 0.125 - 0.25$ mm) sand in its emerged portion and by fine sand in its submerged profile, with the sediment size decreasing moving toward the south [75]. The submerged beach southward of the MRE is characterized by slopes ranging from 1:30 to 1:40 and usually features an array of three–four shore-parallel, shallow bars within 300 m from the shoreline, in water depths between 0 and 3 m (see Figure 2.2a).

A comparison between two bathymetries, derived from surveys run by the Municipality of Senigallia in 2020 and 2015, is shown in Figure 2.2b. The surveys cover a

[1] http://www.morse.univpm.it

Figure 2.1: View of the study area.

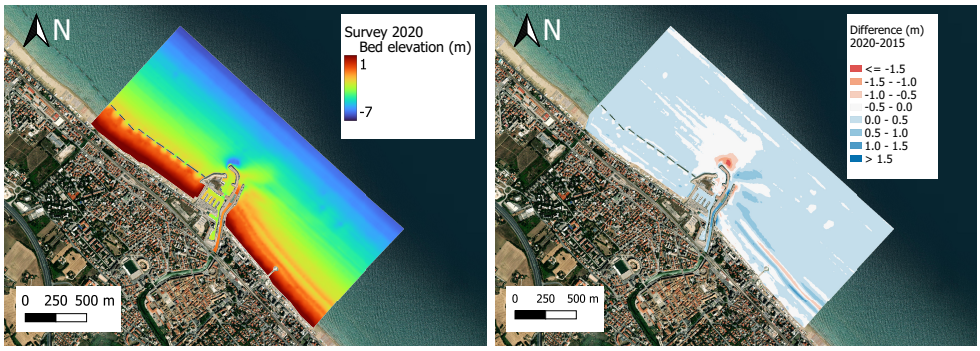

(a) (b)

Figure 2.2: a) Bathymetry reconstructed from the survey carried out in 2020; b) Bed elevation differences between the surveys of 2020 and 2015: positive and negative values show deposition and erosion, respectively.

longshore length of 2.5 km and extend up to the bathymetric of around -7 m. Their difference highlights some areas of major bed variation along the river, just out of the mouth and in the sandbar zone south of the estuary. Due to the reduced precipitation of the last years, the riverbed elevation has increased, leading to the emergence of the inner mouth bar, thus not sampled in the 2020 survey (see the missing data along the channel in Figure 2.2.

The coast of Senigallia is located in a micro-tidal environment, with maximum tidal excursion rarely exceeding 0.6 m [55].[2] The MRE is classified as a salt-wedge estuary, characterized by freshwater flowing out to the sea in the upper layer of the water column and a seawater intrusion occurring in the lower layer [84]. The freshwater discharge of the MR transports sediments down to the river mouth and to the nearshore region, especially during the wintertime [8], exiting in the sea about 300 m seaward of the shoreline, this affecting the plume evolution. The sediment transport of the Northern Adriatic Sea is influenced by both the wave motion and the Western Adriatic Coastal Current (WACC) that drives the sediment southward [25].

Previous studies [75] evaluated the overall wave climate on the bases of the significant wave height, peak period and direction provided every half hour by the Ancona Buoy, belonging to the Italian wave measurement network (RON).[2] The buoy worked from 1999 to 2006, from 2009 to 2013 and was restored in 2021. During these years, the waves mainly came from ESE, NNE and NW, the main events being induced by dominant and prevailing winds blowing on the Adriatic Sea, namely, Bora and Levante-Scirocco. The Bora is a cold NNE wind with a relatively short fetch since it

[2] http://www.mareografico.it

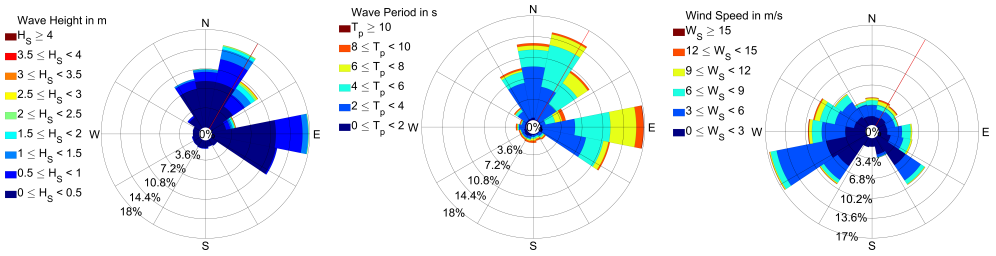

(a) (b) (c)

Figure 2.3: a) Wave rose for significant height; b) wave rose for peak period; c) wind rose. The red line in each rose identifies the orientation of the last stretch of the river, which is about 30°N.

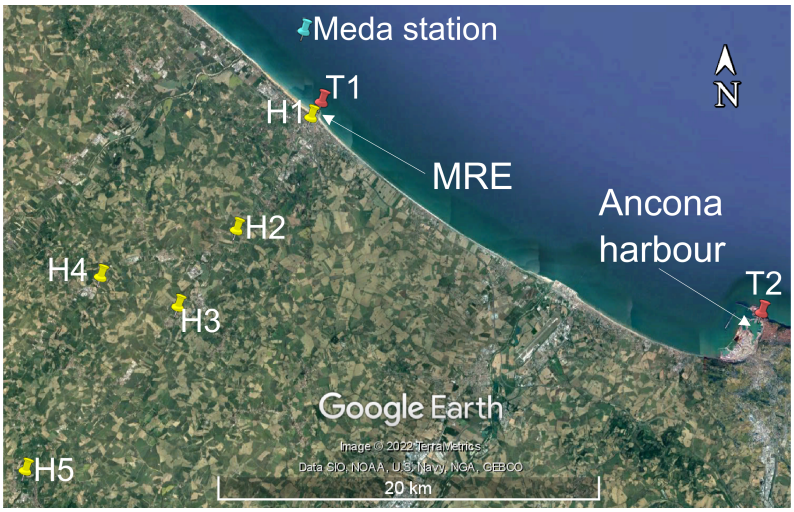

Figure 2.4: Location of the instruments used for the study.

flows along the minor axis of the narrow and elongated Adriatic basin. It generates short, steep and high waves that propagate almost perpendicular to the coast. On the contrary, the Levante-Scirocco is a warm wind that blows from ESE along the major axis of the Adriatic Sea, this resulting in a longer fetch and long and less steep waves. Moreover, the Scirocco wind triggers a storm surge larger than that typical of the Bora storms. These two wave regimes can occur during the same season; in general, the wintertime is characterized by severe storm events, while summertime has milder wave conditions. Both NNE and E waves can enter the river channel, but since the final stretch of the MR faces approximately 30° from the north, NNE waves penetrate more easily than E waves. In 2018, a new ADCP was installed at the Meda station [76], offshore of Senigallia, to measure wave characteristics. The wave roses of Figure 2.3a and 2.3b refer to such recent data and agree with the Ancona Buoy recordings. The Meda station also hosts a wind sensor that provided the data for the wind rose (Figure 2.3c), which shows that the most frequent wind comes from WSW and is associated with low speeds (3 - 6 m/s), while the most intense winds blow from NNE and W-WNW.

2.2 Field data collection

This section provides a description of the instruments used in this study to obtain the field data. They characterize the estuarine forcing typically involved in the river mouth hydro-morphodynamics and were correlated with the outcomes derived from the analysis of the video-monitoring products, described in Section 2.3. The analyses span from 2016 to 2019; Table 2.1 reports the time coverage of each instrument.

The main hydrometers used to retrieve river water level data are those located

at “Ponte Garibaldi” and “Bettolelle” (yellow pins H1 and H2 in Figure 2.4). They are installed, respectively, at a distance of about 1.5 km and 10 km upriver from the MR mouth. Both of them are located downstream of the junction of the MR with the Nevola River and acquire a datum of river water level every 30 minutes. For the hydrometer H2, rating curves are also available, from 23 March 2015 to 5 March 2018 and from 15 to 31 December 2019, to compute the river discharge. In order to fill the gap between such periods, discharge data were added from 6 March 2018 to 16 December 2019 using the curve valid until 5 March 2018. Moreover, to compensate for possible lacks of water level data and to better understand some plume events, other hydrometers were exploited (respectively yellow pins H3, H4 and H5 in Figure 2.4). All the hydrometers are deployed along the Misa and Nevola Rivers and managed by the Italian Civil Protection – Marche Region.

Data of sea current speed and direction were provided by the Sontek Argonaut XR Acoustic Doppler Current Profiler (ADCP), installed in May 2016 and deployed at the Meda TeleSenigallia station [76], which is about 1.5 nautical miles north of Senigallia and 1 nautical mile offshore (cyan pin in Figure 2.4), at a depth of 12.5 m. The up-looking, bottom-mounted ADCP recorded one datum every 10 minutes and used 3-m cells (blank is 1 m). This instrument was substituted with the Teledyne RDI WorkHorse Sentinel ADCP 300 kHz, managed by the CNR-IRBIM (National Research Council – Institute of Marine Biological Resources and Biotechnologies), in May 2018 within the MORSE project.[1] Such up-looking, bottom-mounted ADCP is still working, uses 1-m cells (blank is 70 cm), and measures one datum every 20 minutes. It was set to measure also wave climate data, providing one datum per hour. Sea current measurements are those collected at the most superficial cells, while the wave climate statistics (wave significant height, peak period and mean direction) were obtained employing cells number 1, 4, 7, 8 of the Teledyne ADCP, cell number 1 being the closest to the seabed.

The wave climate before May 2018 was derived from a multi-year wave hindcast from the Mediterranean Sea Waves oceanographic model by the E.U. Copernicus Marine Service (CMEMS) [40]. The model is based on WAM Cycle 4.5.4, which has been developed as a nested sequence of two computational grids (coarse and fine) to ensure that swell propagating from the North Atlantic towards the strait of Gibraltar is correctly entering the Mediterranean Sea. The database is composed of hourly-averaged wave parameters at $1/24^\circ$ horizontal resolution; the data closest to the Meda station, at a water depth of 10.5 m, have been collected.

Data of wind speed and direction were supplied by the Gill WindSonic ultrasonic sensor deployed at the Meda station and provided one datum every 10 minutes.

The sea water level was derived from a tide gauge installed during the MORSE project within a protected area close to the entrance of the Senigallia Harbour in 2018 (red pin T1 in Figure 2.4). For earlier periods, we used online data acquired by the ISPRA Tide Station located inside the Ancona Harbour (red pin T2 in Figure 2.4), about 25 km away from Senigallia.[1] The two signals are in good and continuous agreement. The Ancona and Senigallia tide gauges record water level data every 10 and 6 minutes, respectively, and their elevation datum is the mean sea level. In addition, the astronomical component of the tide was derived from the total signal recorded by the Ancona gauge using the tidal analysis of Delft3D Tide module.

Table 2.1 reports the complete list of instrumentation with their time coverage and resolution.

2.3 Remote sensing products

Remote sensing includes multiple techniques useful to integrate field data. In this study, the products acquired by two video-monitoring stations and satellite were used. The main station is called Sena Gallica Speculator (SGS) and is described in Section 2.3.1, while the ISPRA video system and the Sentinel-2 images are presented in Section 2.3.2.

Table 2.1: Instruments used for the analysis.

Data type	**Instruments**	**Time coverage**	**Temporal resolution**
Water level	Hydrometer H1	2014-2019	30 minutes
	Hydrometer H2	2015-2019	
	Hydrometer H3	2014-2019	
	Hydrometer H4	2014-2019	
River discharge	Rating curve of hydrometer H1	2014-2019	30 minutes
Wave parameters	ADCP (EsCoSed experiment)	Jan 2014	1 hour
	CMEMS	2016-2018	1 hour
	Teledyne ADCP (Meda station)	2018- 2019	1 hour
Sea water level	Ancona tide gauge T1	2014-2018	10 minutes
	Senigallia tide gauge T2	2018-2019	6 minutes
Astronomic tide	Delft3D tide module	2014-2019	same as the input signal
Wind	Weather station	Jan 2014	15 minutes
	Gill WindSonic sensor (Meda station)	2016-2019	10 minutes
Sea current	Sontek ADCP (Meda station)	2016-2018	10 minutes
	Teledyne ADCP (Meda station)	2018-2019	20 minutes

2.3.1 SGS station

The MRE is monitored since July 2015 by the SGS video-monitoring station, deployed at the north pier of the Senigallia harbour within the EStuarine COhesive SEDiments (EsCoSed) project framework [8]. The installation has been made possible thanks to the collaboration between the Department of Civil and Building Engineering and Architecture of the Università Politecnica delle Marche and the U.S. Naval Research Laboratory. The objective of the EsCoSed project was to better understand coastal, estuarine, and riverine processes at the MR mouth.

The SGS station is part of the Coastal Imaging Research Network (CIRN)[3]; its structure and functioning are similar to those of the classical Argus station system [34], even if it is not part of the Argus Network. The main differences with traditional Argus stations regard the type of data storage and the logistics of the archive. While only subsampled pixel time series are collected by traditional Argus systems, the SGS station collects full frame video data that are, then, elaborated in post-processing. This has the advantage of gathering more general information that can be processed in different ways depending on the application; on the other hand, this implies storing large data volumes.

SGS is composed of four cameras FLIR/Point Grey Grassopher3 with 9 Mpx resolution (3376 $\times$ 2704), located on the top of a tower, 25 m above the mean sea level, and oriented to frame both the MRE and the 500 m-long unprotected beach between the harbour southern jetty and the Rotonda pier. The field of view of each camera is 53°, for an overall angle of 200° (Figure 2.5a). The resolution is between 0.05 m and 0.50 m.

The four cameras collect a 10-minutes video, recorded at 2 Hz, during each daylight hour, from 5:00 AM to 5:00 PM (UTC). Furthermore, the first video frame is also saved as a snapshot, for a total of thirteen videos and thirteen snapshots a day, for each camera [68, 69].

The hourly videos and snapshots recorded from the SGS station are post-processed to create a range of remotely sensed products. The one used in this study is an orthorectified, time-exposure, stabilized plan-view image. First, the videos of each hour and each camera are used to create a 10-minute time-exposure image (Timex) by averaging the intensity values of each pixel over the 10-minute sampling period. Then, such images are stabilized using a geometric transformation that aligns them with a target image, which is the Timex image of the day when the cameras' geometry was calculated. Finally, the oblique and stabilized Timex images are merged and geo-rectified using a photogrammetric method [26], which allows for the transformation from image (2D) to world (3D) coordinates by fixing one of the real coordinates, generally the z-coordinate equal to the measured tidal level. In this case, since the MRE is micro-tidal, the z-coordinate is assumed to be equal to zero. For each hour, the four ortho-rectified Timex images are merged to obtain the plan view image (Figure 2.5b).

All the post-processing operations have generated a continuously updated database since July 2015, with some data loss due to malfunctioning of the station. The plan-view images were processed to detect the emerged part of the MR mouth bar (see Section 3.1) and for a quantitative analysis of the plume extension (see Section 4.1.1).

2.3.2 Other remote sensing data

The surrounding nearshore region of the MRE is contextually monitored by a second video system, deployed and maintained by ISPRA, in order to provide information on sand bar dynamics.[4] The monitoring station, located 2 km southward from the Senigallia harbour, shares a sampling strategy similar to that of SGS, collecting images of the nearshore zone at 2 Hz for ten minutes during each daylight hour through digital video-cameras [66]. Oblique images from the ISPRA video system (Figure 2.6a), available since May 2016, were used to qualitatively correlate with the findings from SGS and satellite images and to inspect the distance reached by the plume in the

[3]https://Coastal Imaging Research Network
[4]https://videomonitoraggio.isprambiente.it

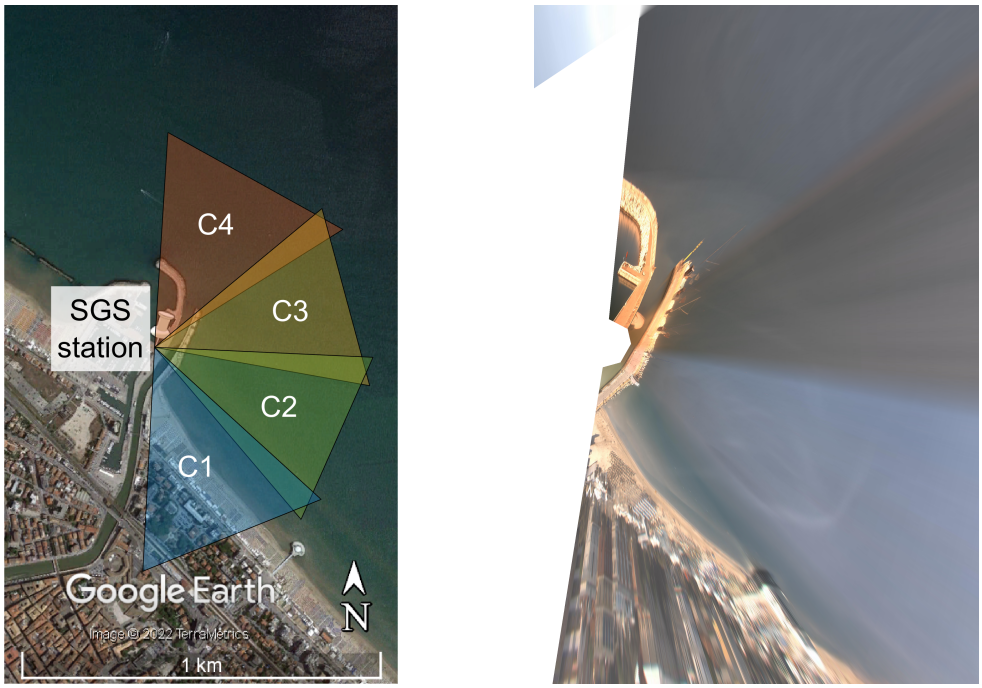

(a) (b)

Figure 2.5: a) General view of the Senigallia harbour showing the SGS station position and the cameras field of view (C1, C2, C3 and C4 are the camera names); b) Example of an orthorectified, stabilized, Timex plan-view image.

southeast direction. In most cases, we found that the plume extended to the location of the ISPRA video system and farther south.

To visualize a wider area and better observe the plume bending toward NW, the SGS dataset was integrated with Sentinel-2 images (Figure 2.6b). The available tiles were 100×100 km^2 ortho-images in UTM/WGS84 projection and had a temporal resolution of 5 days, this making them alone not suitable to capture the dynamical evolution of the MR plume. Therefore, such images were used to track the plume front and, for times when both SGS and Sentinel-2 images were available, the two fronts were compared, to find a good overlap.

(a) (b)

Figure 2.6: a) Snapshot acquired by the ISPRA video system, showing the MRE in the background; b) Sentinel-2 image of the studied area.

Chapter 3

Study of the MR mouth bar

The recent years have been characterized by a drastic reduction in the amount of precipitation with consequent decrease in the river discharge. This has modified the typical cyclic behaviour of the MR mouth bar [8], which was not pushed toward the sea, out of the river mouth, as frequently as before. Therefore, the river sediment continued to accumulate along the last stretch of the river channel and started emerging for long periods, reaching very large sizes at times, generating managing issues and concern. The objective of this study is to understand the factors affecting the inner mouth bar behaviour, in order to clarify the processes of the bar evolution and migration. Thus, besides a thorough understanding of the morphodynamical phenomenon, this analysis can be useful also for the future management of the harbour and estuarine area.

First the bar position and size were detected from the SGS images using a MATLAB code described in Section 3.1. Then, the geometric characteristics of the bar were correlated with the forcing acting at the river mouth to understand the physical processes involved in the bar evolution, which were further inspected using the Delft3D numerical suite (see Section 3.2). Sections 3.3 and 3.4 present the results of the analysis.

3.1 River Bar Toolbox

A MATLAB code was built to detect, using a sequence of image processing operations, the bar in the plan-view images and automatically measure its emerged area (hereinafter simply "area"), centre of mass and perimeter. The coordinates of the pixels included in the detected area are also stored, in order to allow for the reproduction of the shape of the deposit after the analysis. The code is available online, in the CIRN website, with the name *River Bar Toolbox*.[1]).

The code allows one to analyze each available image stored in a user-defined folder. In this case, all the images collected in the database, from 2017 to 2019, were processed. The first step of the procedure consists of cropping the images to focus on the river mouth (801×501 pixels). Then, the images are converted to grayscale to enable the application of some image processing operation that require the images to be grayscale. At this point, the code shows the image, called *Image A* in Figure 3.1, and the user has to choose among four options:

1. *visible bar*, meaning that the user can recognize the bar from the image;
2. *not visible*, meaning that, despite the good quality of the image, the user cannot see the bar;
3. *dark*, meaning that the image is dark because of either a system malfunctioning or bad meteorological-lighting conditions (fog, acquisition time during no-light hours, ecc.);

[1]CIRN - River Bar Toolbox

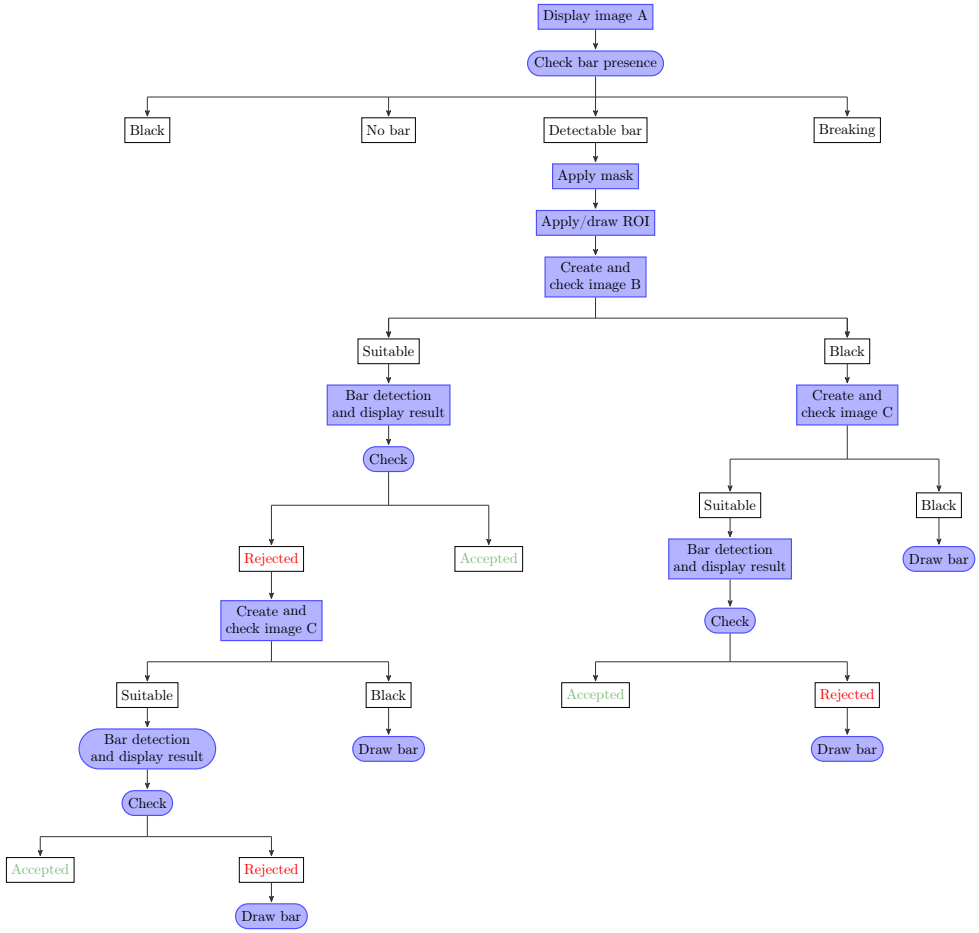

Figure 3.1: Flow-chart of the algorithm used by the River Bar Toolbox. Blue squared and rounded box report actions done by the code and the user, respectively. White boxes show user's and code's choice options.

4. *breaking*, meaning that the bar is not emerged but wave breaking is visible on the surface (this probably indicating the presence of a submerged deposit).

Only images that showed the presence of the bar are analyzed further. In all other cases, the code records the user's choice and proceeds to the next image. The next step consists in applying a mask to the cropped image to exclude all areas except for the river. In fact, the success of the code in identifying the bar depends mainly on the difference of colour between the bar and the water. Thus, the mask should cover the areas that have a colour similar to that of the bar, for example the river jetties, otherwise the code will recognize the jetties' pixels as belonging to the bar. Such mask is built one time at the beginning of the analysis and then used for all the processed images. Then, the user has to draw a Region Of Interest (ROI) around the bar to let the code know where to perform the detection. In this study, the ROI was changed and adapted for each analyzed day, thus every 13 images. At this point, the image is totally black apart from the ROI and the gradient is performed, using the Sobel gradient operator, which computes the gradient of a pixel as a weighted sum of pixels in its 3-by-3 neighbourhood. The weights for gradients in the vertical direction are:

$$\begin{bmatrix} 1 & 2 & 1 \\ 0 & 0 & 0 \\ -1 & -2 & -1 \end{bmatrix}$$

For the horizontal direction, the weights are transposed. The resulting gradient image is converted into binary format, this meaning that the pixels can have either a

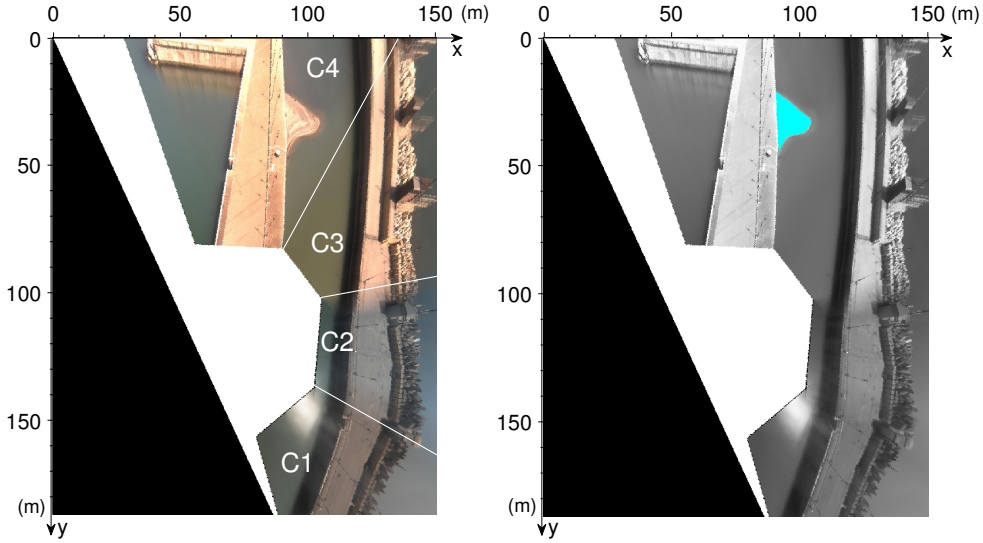

Figure 3.2: a) Reference frame (in meters) for the MR mouth bar analysis, with the cameras field of view reported. b) Grayscale image, with the result of the detection of the bar superimposed (cyan).

value equal to zero (black colour) or one (white colour). This image is called *Image B* in the flow-chart of the code shown in Figure 3.1 and is obtained by replacing all pixel values above a determined threshold with ones and setting all other values to zero. The threshold is computed using the Otsu's method [65], which minimizes the intraclass variance of the thresholded black and white pixels. *Image B* could be either i) suitable for identification of the bar (Figure 3.1) or ii) totally black, depending on the contrast of the starting image. In the first case, the bar is detected and overlaid on the grayscale image to allow the user to check the result (Figure 3.2b). In the second case, contrast enhancement is performed on the original image and the image gradient operation is repeated. In fact, the failure to make a suitable binary image usually results from insufficient image contrast, which prevents the gradient operation from identifying the bar. Thus, the contrast is improved using Contrast Limited Adaptive Histogram Equalization (CLAHE). Adaptive Histogram Equalization (AHE) differs from ordinary histogram equalization methods because it computes several histograms, each corresponding to a distinct section (or tile) of the image. Consequently, local contrast is improved by enhancing the definitions of edges in each region of the image. However, AHE tends to amplify the noise in relatively homogeneous regions of the image, therefore CLAHE is used to limit such amplification, by clipping the histogram at a predefined value [97]. The CLAHE algorithm is used whenever the first attempt to identify the bar fails and produces another binary image (*Image C* in Figure 3.1). So, the detection of the bar can be executed with two different sequences of image-processing operations, and the best result can be accepted. If both methods fail to recognize the bar, the user can discard both results and draw the bar shape manually. Once the bar boundaries are identified, the number of pixels that form the area and perimeter of the bar are counted and stored together with the pixel coordinates of the bar centre of mass.

The conversion between pixels and meters was done comparing the image and the world coordinates (WGS84-UTM) of the plan-view images that are stored with them; the resulting scale factor is 0.2999 m/pixel. The photogrammetric transformation between 3D world coordinates and 2D image coordinates is based on [26]. It uses a projection matrix that include 11 parameters, of which:

- 5 intrinsic parameters, depending only on the camera; characteristics and derived by a calibration in the laboratory;
- 6 extrinsic parameters, function of the camera installation, obtained using some

Ground Control Points (GCPs), that are visible points whose world locations are known by dedicated surveys and whose image locations can be found from the images.

For more details about the transformation between 3D world coordinates and 2D image coordinates, the reader can refer to [68].

Furthermore, the results discussed in this thesis refer to a reference frame, obtained by rotating the image of 24.8° in an anticlockwise direction, so that the y-axis is in the long-river direction, positive upriver, and the x-axis is in the cross-river direction, positive rightward (or eastward). The reference frame is shown in Figure 3.2a. Since the original aim of the SGS video-monitoring station was to observe the beach to the south of the MRE, the installation height and tilt of the cameras were decided based on such objective and with less attention on the river. Therefore, it can be noticed in Figure 3.2a that, for y>80 m, not the whole cross section is framed by the cameras.

The analysis led to a set of 13 data of bar characteristics for each day. It was observed that, during a day, the bar area was mainly influenced by the tidal variations, which simply caused a major/minor emergence of the bar during low/high tide, respectively. Since the main aim was to understand the bar evolution under events such as river floods and sea storms, which typically last for hours to days, the hourly effect of the tide was neglected by extracting a single datum per day. To obtain representative daily values of bar area and centre of mass, an arithmetic mean of the data from 5:00 AM to 5:00 PM was computed.

3.2 Numerical modeling

3.2.1 Delft3D numerical solver

Delft3D is a modeling suite developed by WL|Delft Hydraulics in close cooperation with Delft University of Technology. The Delft3D package consists of several integrated modules that allow for the simulation of hydrodynamic flow (under the shallow water assumption), computation of the transport of constituents (e.g., salinity and heat), short wave generation and propagation, sediment transport and morphology, and the modeling of ecological processes and water quality parameters [44]. The software is widely used and has proven his capabilities in relation to many test cases around the world; given the large number of processes that can be included, it can be applied to simulate a wide range of river, estuarine, and coastal situations.

The heart of the Delft3D modeling framework is the FLOW module, a multi-dimensional hydrodynamic simulation programme that calculates non-steady flows resulting from tidal and meteorological forcing on a curvilinear, boundary fitted grid or spherical coordinates. The calculation of the transport of water-borne constituents and sediment and the computation of morphological changes are performed simultaneously (or "online") within the FLOW module, this bringing many advantages. For example, i) sediment transport and morphological simulations are simpler to perform and do not require a large communication data file to share results between different modules, and ii) changes in bathymetry can be immediately fed back to the hydrodynamic calculations. The online sediment module allows one to compute the morphological changes due to the transport, erosion, and deposition of both cohesive and non-cohesive sediments, this making it suitable for investigating sedimentation and erosion problems in complex hydrodynamic situations.

The Delft3D-FLOW module is suitable for predicting the flow in shallow seas, coastal areas, estuaries, lagoons, rivers, and lakes. It solves the unsteady shallow-water equations in two (depth-averaged) or three dimensions. The horizontal momentum equations, the continuity equation, the transport equation, and a turbulence closure model form the system of equations. The vertical momentum equation is reduced to the hydrostatic pressure relation as vertical accelerations are assumed to be small compared to gravitational acceleration and are neglected. For depth-averaged simulations such as those performed in this work, the continuity and horizontal momentum equations

are [44]:

$$\frac{\partial \eta}{\partial t} + \frac{\partial hu}{\partial x} + \frac{\partial hv}{\partial y} = S \tag{3.1}$$

$$\frac{\partial u}{\partial t} + u\frac{\partial u}{\partial x} + v\frac{\partial u}{\partial y} = -g\frac{\partial \eta}{\partial x} + M_x + g\frac{u\sqrt{u^2+v^2}}{C_u^2 h} + \nu_H\left(\frac{\partial^2 u}{\partial x^2} + \frac{\partial^2 u}{\partial y^2}\right) \tag{3.2}$$

$$\frac{\partial v}{\partial t} + u\frac{\partial v}{\partial x} + v\frac{\partial v}{\partial y} = -g\frac{\partial \eta}{\partial y} + M_y + g\frac{v\sqrt{u^2+v^2}}{C_v^2 h} + \nu_H\left(\frac{\partial^2 v}{\partial x^2} + \frac{\partial^2 v}{\partial y^2}\right) \tag{3.3}$$

where η is the water level with respect to the mean sea level, t is time, h is the water depth, u and v are the flow velocity components in the x and y directions, respectively, S represents the source/sink of water mass and g is gravity acceleration. C_u^2 and C_v^2 are the Chézy roughness coefficients in the x and y directions, respectively, and are related with the Manning coefficient n using $C = \frac{h^{1/6}}{n}$. M_x and M_y represent the external sources or sink of momentum, whereas the last term in equations 3.2 and 3.3 represents the horizontal Reynold's stresses, in which ϵ_H is the horizontal eddy viscosity defined by the user. For more details on such equations, the reader is referred to [14, 44].

The Delft3D-WAVE module simulates the evolution of wind-generated waves in coastal waters using the phase-averaged, third-generation SWAN wave model [5]. SWAN accounts for (refractive) propagation due to current and depth and represents the processes of wave generation by wind, dissipation due to whitecapping, bottom friction and depth-induced wave breaking and non-linear wave-wave interactions [15]. It is based on the discrete spectral action balance equation [27] and is fully spectral:

$$\frac{\partial}{\partial t}N + \frac{\partial}{\partial x}c_x N + \frac{\partial}{\partial y}c_y N + \frac{\partial}{\partial \sigma}c_\sigma N + \frac{\partial}{\partial \theta}c_\theta N = \frac{S}{\sigma} \tag{3.4}$$

where $N(\sigma, \theta)$ is the action density spectrum and c_x, c_y, c_σ and c_θ are the propagation velocities in x-, y-, σ- (frequency) and θ- (directional) spaces, respectively. S is the source term in terms of energy density representing the effects of generation, dissipation and non-linear wave-wave interactions. The first term in the left-hand side of equation 3.4 represents the local rate of change of action density in time; the second and third terms give the propagation of action in the geographical space; the fourth term describes the shifting of the relative frequency due to variations in depths and currents; the fifth term represents the depth-induced and current-induced refraction.

Wave effects can be included in a Delft3D-FLOW simulation in different ways. In the following, only the online coupling of the two modules is described since it is the one used in this work. Every coupling time step, decided by the user, the latest bed elevations, water elevations and, if desired, current velocities are supplied from the FLOW module to the WAVE one. The computed wave field can thereby be updated accounting for the changing flow field and bathymetry. In an analogous way, the WAVE module provides information (e.g., RMS wave height, peak spectral period, wave direction, mass fluxes, etc.) to the FLOW module that includes them in flow calculations. Using this approach, the effect of currents on waves could be taken into account and vice versa. Some processes, currently available in DELFT3D, through which the wave action may influence morphology are i) wave forcing due to breaking, ii) enhanced bed shear stress, and iii) the additional turbulence production due to dissipation in the bottom wave boundary layer and due to wave whitecapping and breaking at the surface.

Different sediment fractions (up to five) can be defined in Delft3D. Each fraction must be classified as "mud" (cohesive), or "sand" (non-cohesive) as different formulations are used for the bed-exchange and settling velocity of these different types of sediment [14]. Moreover, both the bedload and the suspended transports are computed for the "sand" fractions, while only the suspended transport is calculated for the "mud" fractions.

For the suspended-sediment transport, the advection-diffusion equation is used:

$$\frac{\partial hc}{\partial t} + \frac{\partial huc}{\partial x} + \frac{\partial hvc}{\partial y} = h\left[\frac{\partial}{\partial x}(\epsilon_s \frac{\partial c}{\partial x}) + \frac{\partial}{\partial y}(\epsilon_s \frac{\partial c}{\partial y})\right] + hS \tag{3.5}$$

where c is the sediment concentration, ϵ_s is the sediment eddy diffusivity and S is the source term modeling the net mass flux between the water column and the bed. The local flow velocities and eddy diffusivity are based on the results of the hydrodynamic computations (for more details, the reader is referred to [14]).

The erosion (E) and deposition (D) fluxes for the cohesive sediment are calculated with the Partheniades-Krone formulations [67]:

$$E = MS(\tau_{wc}, \tau_{cr,e}) \tag{3.6}$$

$$D = w_s c_b S(\tau_{wc}, \tau_{cr,d}) \tag{3.7}$$

where M is a user-defined erosion parameter, $S(\tau_{wc}, \tau_{cr,e})$ is the erosion step function, w_s is the hindered settling velocity, c_b is the average sediment concentration in the near bottom computational layer, and $S(\tau_{wc}, \tau_{cr,d})$ is the deposition step function.

The step functions are defined as follows:

$$S(\tau_{wc}, \tau_{cr,e}) = \begin{cases} (\frac{\tau_{cw}}{\tau_{cr,e}} - 1), & \text{when } \tau_{cw} > \tau_{cr,e} \\ 0, & \text{when } \tau_{cw} \leq \tau_{cr,e} \end{cases} \tag{3.8}$$

$$S(\tau_{wc}, \tau_{cr,d}) = \begin{cases} (1 - \frac{\tau_{cw}}{\tau_{cr,d}}), & \text{when } \tau_{cw} < \tau_{cr,d} \\ 0, & \text{when } \tau_{cw} \geq \tau_{cr,d} \end{cases} \tag{3.9}$$

where τ_{cw} is the maximum bed shear stress due to current and waves, $\tau_{cr,e}$ is the user-defined critical erosion shear stress, and $\tau_{cr,d}$ is the user-defined critical deposition shear stress. Therefore, the erosion of cohesive sediments takes place when $\tau_{cw} > \tau_{cr,e}$, while deposition occurs if $\tau_{cw} < \tau_{cr,d}$.

For non-cohesive sediments, the approach of van Rijn [87] is used. It distinguishes between sediment transport below a reference height a_s, which is treated as bedload transport, and that above the same reference height, which is treated as suspended-load:

$$a_s = min\left[max\left\{k_s, \frac{\Delta_r}{2}, 0.01h\right\}, 0.2h\right] \tag{3.10}$$

where k_s is the current-related effective roughness height as determined in the Delft3D-FLOW module and Δ_r is the wave-induced ripple height, set to a constant value of 0.025 m. Sediment is entrained in the water column by imposing a reference concentration at the reference height. The erosive flux due to upward diffusion (E_{nc}) and the deposition flux due to sediment settling (D_{nc}) are defined as:

$$E_{nc} = \epsilon_s \frac{\partial c}{\partial z} \tag{3.11}$$

$$D_{nc} = w_s c_{kmx} \tag{3.12}$$

where z is the vertical coordinate and c_{kmx} is the average concentration through the bottom of the reference layer (kmx-layer) located above the reference height. The sinks and source terms derived form this two fluxes are further explained in the Delft3D-FLOW Manual [14]. The magnitude of the bedload transport for simulations including waves is computed as follows [88]:

$$S_b = 0.006\rho_s w_s D_{50} M_s^{0.5} M_e^{0.7} \tag{3.13}$$

where ρ_s is the sediment density, M_s is the sediment mobility number due to waves and currents and M_e is the excess sediment mobility number, for which the reader is referred to [14]. The bedload transport takes place when the shear stress at the bottom exceeds the critical shear stress:

$$\tau_{cr} = (\rho_s - \rho_w) g D_{50} \theta_{cr} \tag{3.14}$$

whit threshold parameter θ_{cr} calculated according to the classical Shields curve and modeled by van Rijn [87] as a function of the non-dimensional grain size $D^* = D_{50}(\frac{\Delta g}{\nu^2})^{1/3}$. In the latter equation, $\Delta = \frac{\rho_s - \rho_w}{\rho_w}$ is the submerged specific gravity of a

sediment with density ρ_s, ρ_w is the water density and ν is the kinematic viscosity of water.

The bed can be modeled as a unique layer or as a stratigraphy and the composition of each layer must be defined. In the former case, one uniformly mixed layer is implemented, where all sediments are available for erosion. In the latter case, only sediments in the top-most layer are available for erosion, while the deposited sediments are initially added to the top-most layer and then fill up the layers beneath it, up to a user-defined thickness. When such thickness is exceeded, a new layer is created until the number of layers reaches the maximum defined by the user; otherwise, layers at the bottom of the stratigraphy are merged. For more details on the sediment and morphology computations, the reader is sent back to [14, 44].

When modeling complex geometries, as the one of the MR mouth and adjacent harbor, the setting-up of an accurate and efficient model grid can be quite difficult due to the irregular domain boundaries. Moreover, in order to reduce the computational time without losing accuracy in some areas of the domain, the user may want to refine the grid gradually for gaining the appropriate resolution to adequately simulate physical processes in such areas. In Delft3D-FLOW, this can be achieved by using the domain decomposition approach, which consists in the subdivision of the model into non-overlapping domains, each covered by its own structured grid. Then, computations can be carried out separately on these domains that communicate through internal boundaries, the so-called DD-boundaries. According to Deltares, such technique is the numerical approach that meets best the demands of efficiency, accuracy and general applicability [14]. Domain decomposition uses a direct iterative solver, comparable to the single domain implementation, for the continuity equation; while the so-called additive Schwarz method, which allows for parallelism over the domains, is used for the momentum equations, the transport equation and the turbulence equations. This implementation has allowed the domain decomposition to have a similar robustness as the single domain Delft3D-FLOW code (for more details, see [14]).

Differently, the nesting technique is supported by the Delft3D-WAVE module. It allows for use of nested computational grids in one wave computation, so that it is possible to have a coarse grid for a large area and one or more finer grids for smaller areas. First, the coarse grid computation is executed; then, the finer grid computations use these results to determine their boundary conditions (for more details, see [15]).

3.2.2 Simulations set up

A two-dimensional (2D), depth-averaged, model was set-up using the Delft3D software suite to simulate an observed event and to analyze the effect of different forcing through parametric simulations. Three regular grids were created, rotated by 47.6° with respect to the North, to follow the coast orientation (Figure 3.3). The largest and the smallest grids (*grid 1* and *grid 3*, respectively) were nested in the WAVE module, while the domain decomposition approach was used in the FLOW module between the intermediate-size grid (*grid 2*) and the smallest grid (*grid 3*). *grid 1* covered the coastal area in front of the Senigallia Harbor; it had a resolution of about 30 m and extended around 7 km in the alongshore direction and 2.5 km in the offshore direction. *grid 2* was created from *grid 1* by cutting some cells at the offshore and lateral boundaries. It extended about 6 km in the alongshore direction and 2.4 km in the cross-shore direction. *grid 3* covered the final stretch and the mouth of the MR and expanded about 1 km in alongshore direction and 1.5 km in the offshore direction. It had a variable resolution ranging from around 8 m in the offshore region to around 3 m along the river. The reference system was Monte Mario / Italy Zone 2.

The bathymetry was built out of a multibeam echosounder survey performed in September-October 2018 by the municipality of Senigallia (Figure 3.4a). The survey has a resolution of 1 m and extends 1 km offshore from the coastline, up to around 6 m depth, and 2.5 km in the alongshore direction, being the MRE at the centre of the survey. It shows the presence of a submerged deposit, some 60 cm under the water surface (Figure 3.4b). This dataset was integrated, to complete the bathymetry of the offshore region, with the values of the EMODnet bathymetry, available online at a

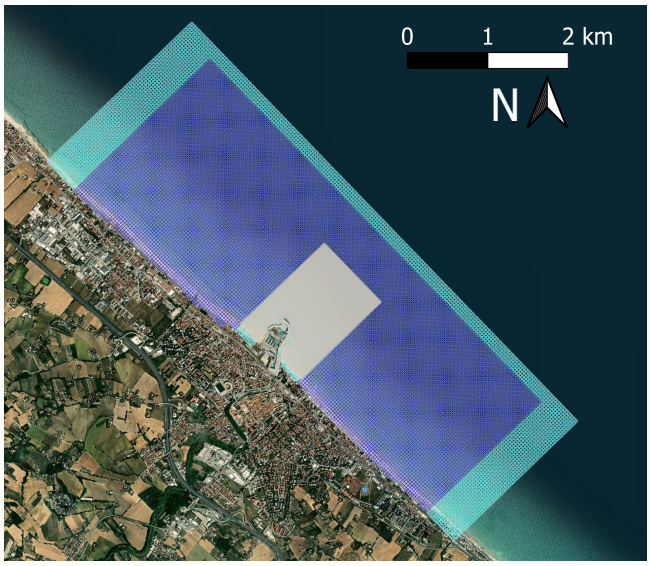

Figure 3.3: Grids for the MR bar numerical simulations: *grid 1* in cyan, *grid 2* in blue, and *grid 3* in gray.

resolution of about 115 m.

The sediment fractions were characterized on the basis of two monitoring campaigns, one of April 2019, interesting the final stretch of the MR, and one of February 2018, representative of the beach to the south of the MR [16]. The results of these campaigns show that the riverbed is mainly composed of silts and clays, with a progressive amount of sand moving toward the mouth, where also gravel is present. Considering this, three types of sediment were included in the simulations, one cohesive fraction and two non-cohesive fractions, namely sand and gravel. The median diameter of the sand was set to 180 μm, while the gravel was characterized by a D_{50} =6 mm. Therefore, the critical bed shear stress for the bedload transport initiation is around 0.05 N/m^2 and 0.06 N/m^2, respectively for sand and gravel. The cohesive fraction was characterized by a critical shear stress for erosion of 0.3 N/m^2, a critical shear stress for deposition of 0.4 N/m^2, a settling velocity of 0.1 mm/s and an erosion parameter of 10^{-4} kg/m^2/s. Such values fall within the ranges used in the literature (e.g., [86, 92]) and were chosen after a model calibration (see Sections 3.2.3 and 4.2.2).

The bed was modeled using two layers of sediments, the lower one with constant thickness, while the upper one with variable thickness to model the shape of the deposit. Both layers were characterized by 100% of sand in the sea region and 100% of cohesive sediment in the most upriver section (in the following "river section"), located around 600 m upstream from the river mouth. In between, the percentages of cohesive sediment and sand were progressively varied, as shown in Figure 3.5. Moreover, in correspondence of the bar, the upper layer had a 3% increase of gravel with an equivalent reduction of sand. This composition well-represented also the mixture of sediments found in the samples collected in the final 620 m of the MR during the EsCoSed project, showing highly heterogeneous sediments, with a mix of gravel, mud and sand [8].

The Delft3D-FLOW and WAVE modules were online coupled, apart from the simulations forced only with the river discharge, for which the FLOW module was run alone. The boundary conditions generally depended on the aim of the simulation; to simulate real-life events, observed timeseries of the forces were imposed, whenever available, while "parametric" inputs were created when running test cases. Just at the cross-shore edges of *grid 2*, the boundary condition remained the same for all the simulations, which is a Neumann-type condition of zero-water level gradient.

For test case-simulations, run to separately observe the effects of the river flow (R) and waves (W), "parametric" conditions were imposed. In the R cases, artificial flood hydrographs, reproducing the shape of typical MR flood hydrographs, were

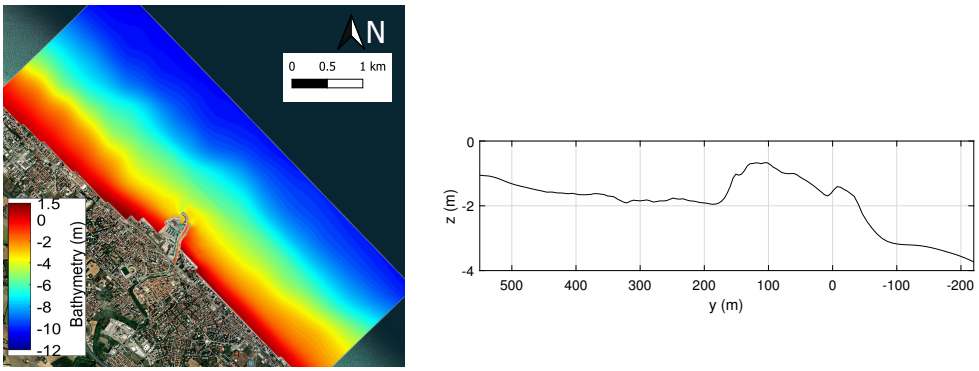

(a) (b)

Figure 3.4: a) Bathymetry used for the MR bar numerical simulations. b) Alongriver section near the left bank showing the submerged deposit; positive and negative y-values indicate, respectively, upriver and offshore locations.

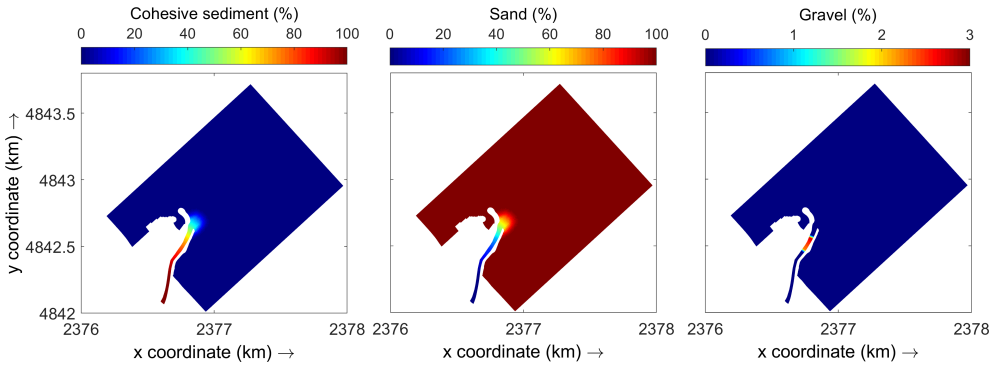

Figure 3.5: Percentages of each sediment volume fraction in the upper layer. The lower layer has no gravel and the sand distribution is complementary to the cohesive one.

Table 3.1: Overview of the test case-simulations run for the inner bar analysis. The values reported are: the river discharge peak; the wave significant height, peak period and mean direction at the storm peak; the tide simultaneous with the river discharge/storm peak.

Simulation ID	**River discharge**	**Waves**	**Tide**
–	m^3/s	m, s, °N	m
R10	10	–	–
R50	50	–	–
R100	100	–	–
R100H	100	–	0.3
R100L	100	–	−0.3
W2N	5	2, 8.1, 20	–
W5N	5	5, 8.4, 20	–
W5NH	5	2, 8.4, 20	0.3
W5NL	5	2, 8.4, 20	−0.3
W2E	5	2, 9.1, 90	–
W5E	5	5, 10.1, 90	–
W5EH	5	2, 10.1, 90	0.3
W5EL	5	2, 10.1, 90	−0.3

built and used at the river section of *grid 3*. Three river discharge peaks of 10, 50 and 100 m^3/s, comparable to the 1-year return period discharge, were tested (R10, R50, R100). The wave process was turned off. On the contrary, for the W cases, the river discharge was set to a very low constant value, 5 m^3/s, and four artificial storms were created, following the shape of typical sea storms, to observe the effects of the waves only. The peak storm significant wave height was varied between 2 m, a typical value for a storm interesting the Senigallia coast, and 5 m, comparable to the 10-years return period wave height. The wave direction was chosen on the basis of the most frequent wave storms occurring at Senigallia (see Figure 2.3a). Therefore, NNE (20°N) and E (90°N) waves were simulated (W2N, W5N, W2E, W5E). Finally, the wave period was set to typical values for such wave conditions, namely around 10 s and 8 s, respectively for E and NNE waves. It was also slightly varied depending on the wave height. Such timeseries of wave parameters (significant wave height, peak period and mean direction) were imposed at the offshore boundary of *grid 1*.

Cases R100, W5N and W5E were run with and without adding a tidal forcing. In particular, a semidiurnal sinusoidal tide of 0.3 m amplitude was used to force the offshore boundary of *grid 2*. The timeseries of the tide was temporally shifted to make the storm/river discharge peaks once simultaneous with the high tide and once with the low tide (R100H, R100L, W5NH, W5NL, W5EH, W5EL).

Table 3.1 summarizes the test case-simulations with their forcing conditions.

Finally, a real-life event, occurred between 18 March 2018 and 2 April 2018, was simulated to observe the evolution of the MR bar under a combination of forces and to compare the results with observations. Since at that time, the MEDA station was not equipped with the ADCP for the wave measurement, the WAVE module was forced with timeseries of wave height, period and direction, downloaded from the Copernicus Marine Service [40]. A discharge timeseries was computed through the rating curves of the Bettolelle hydrometer and then transported to the river section of the FLOW model using the HEC-RAS software package, while the offshore boundary was forced with a tidal timeseries recorded by the tide gauge of the Ancona Harbour. Figure 3.6 shows the described forcing conditions.

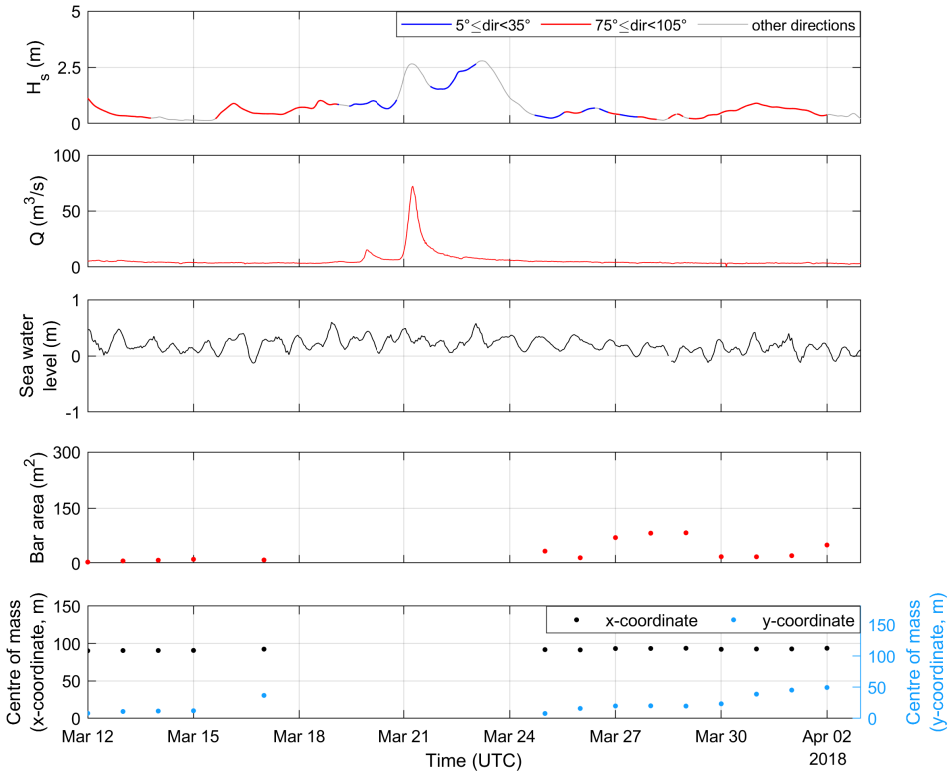

Figure 3.6: The first, second and third panels show, respectively, the timeseries of waves, river discharge and tide used for the real-life simulation. The waves from NNE and E are highlighted in blue and red, respectively. The fourth and fifth panels report the evolution of the bar area and centre of mass during the event.

3.2.3 Calibration of the model

The calibration of the model was done by tuning some user-defined parameters, shown in Table 3.2, and comparing the results with some available measures, coming from the EsCoSed field experiment carried out in January 2014 [8]. In particular, velocity timeseries recorded at two observation points, are used in the following, while turbidity measures taken along the river are discussed in Section 4.2.2.

The bathymetry was created by interpolating at the grid nodes the depth values coming from both the EMODnet bathymetry, available online, and a multibeam survey performed in the lower reach of the MRE before the experiment. The survey was conducted using an ODOM ES3 operating at 240 kHz and had a resolution of 0.7 m. It covered an area of about 400 m^2 around the estuary, up to around 4 m depth, and the final stretch of the river. Additional details can be found in [8].

The WAVE model was forced using wave property timeseries provided by an ADCP, deployed for the experiment and located 900 m offshore of the MRE. The FLOW model was forced using Neumann conditions at the two cross-shore boundaries, water level timeseries of the Ancona tide gauge at the offshore boundary and river discharge timeseries at the river section. First, the river discharge timeseries was computed from the river water level data measured at "Bettolelle" using the available rating curve. Then, since the Bettolelle station is 10 km upriver of the river section of our interest, where the discharge timeseries is imposed, we used the HEC-RAS software package to obtain the discharge timeseries at such section. Furthermore, an error was associated to the discharge timeseries due to the uncertainty in the rating curves. Such error was obtained by comparing the discharges computed through the rating curve with the available measured discharges provided by the Civil Protection. The mean error of 26.83% was added and subtracted to the original discharge timeseries to calculate two new timeseries, namely "inf" and "sup", respectively. Three simulations were run with: 1) the original timeseries, 2) the "inf" timeseries and 3) the "sup" timeseries to obtain the associated velocity timeseries. The velocity timeseries obtained using the original discharge timeseries (v_{mod}) at two observation points, QR2 and QR3 (see [8]), is shown in Figure 3.7 (blue line). The band of velocity obtained with both the "inf" and "sup" timeseries (blue band in Figure 3.7) was taken as the area where the measured velocities had to fall to satisfy the validation.

While the velocity provided by the simulations (v_{mod}) is averaged over the total water depth, that made available by the EsCoSed dataset was averaged from the riverbed to 1.3 m above the riverbed. Thus, we could not directly compare the modeled velocity with the measured one, but some extra elaborations were needed. First, we projected the measured velocities in the river current direction ($v_{obs,1.3}$, red line in Figure 3.7); then, we used such data and the surface velocities measured by the EsCoSed drifters (see [8]) to extrapolate some vertical velocity profiles at QR2 and QR3. We could extrapolate three and two profiles for QR2 and QR3, respectively. It was not possible to extrapolate profiles when the surface velocity was not available. Then, we computed the mean velocity over the total water depth for each profile ($v_{obs,drift}$, red diamonds in Figure 3.7) and the difference between such value and $v_{obs,1.3}$. Finally, we averaged the differences, obtaining 0.13 m/s and 0.11 m/s for QR2 and QR3, respectively. We added such values to $v_{obs,1.3}$ to obtain a datum (v_{obs}, red dashed line in Figure 3.7) more suitable for the comparison with the modeled depth-averaged velocity.

The best comparison, obtained using the parameters reported in Table 3.2, is shown in Figure 3.7.

3.3 Observation results

The evolution of the area and centre of mass of the emerged bar, detected by the images, was correlated with the river and nearshore forcing acting on the estuary. The analyzed period spans from 2016 to 2019, but except for several days in April 2016, the bar was not regularly emerged until 2017. In the following, significant periods are discussed as function of four main processes.

Table 3.2: Parameters used for the simulations.

Parameter	**Tested values**	**Model value**
Manning coefficient ($m^{-1/3}/s$)	0.008 - 0.03	0.015
Background horizontal eddy viscosity (m^2/s)	0.5 - 5	1
Background horizontal eddy diffusivity (m^2/s)	1 - 20	10
Critical shear stress for erosion (N/m^2)	0.1 – 0.5	0.3
Critical shear stress for sedimentation (N/m^2)	0.4 – 1000	0.4
Settling velocity (mm/s)	0.005 – 0.1	0.1
Erosion parameter ($kg/m^2/s$)	1e−5 – 1e−3	1e−4
Calibration factor for bedload by currents (-)	0.2 – 1	0.2
Calibration factor for suspended load by currents (-)	0.2 – 1	0.2
Calibration factor for bedload by waves (-)	0.2 – 1	0.4
Calibration factor for suspended load by waves (-)	0.2 – 1	0.4

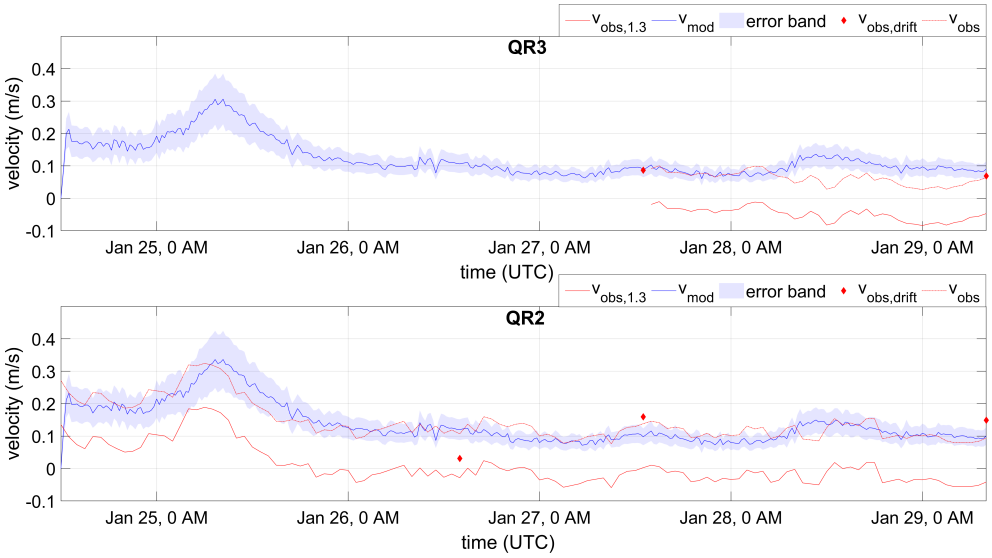

Figure 3.7: Results of the model calibration obtained using the parameters in Table 3.2.

Table 3.3: Overview of the forcing conditions, area and dimensionless displacement of the bar for events R1-R4.

	Event R1	**Event R2**	**Event R3**	**Event R4**
Q (m^3/s)	20.9	36.7	41.5; 88.4	72.3
H_s (m)	3.6	2.1	2.1; 1.7	2.6
Area (m^2)	200	97	81	9
y_{start} (m)	78.7	81.5	46.6	36.8
Δ_{bar} (-)	0.8	1.74	1.71	1.16

The panels of the plots reported in this section show:

1. the wave significant height and direction;
2. the river discharge;
3. the river and sea water levels and astronomic tide;
4. the area of the bar;
5. the x- and y-coordinates of the bar centre of mass.

Waves coming from NNE and E are highlighted in blue and red, respectively, being the most frequent waves approaching the coast of Senigallia (Figure 2.3a). The coordinates of the bar centre of mass refer to the rotated reference system of Figure 3.2a, where an increase of the x- and y- coordinates gives a displacement of the bar centre of mass toward the east riverbank and upriver, respectively.

The process of bar formation is due to the interaction of multiple mechanisms that govern downriver and upriver sediment transport. The bar mainly formed along the final 180 m stretch of the river, on the west bank, that is the inner bank of a mild river bend. Here, the downriver sediment transport, forced by the river discharge, finds a depositional area due to centrifugal actions. Furthermore, the local net alongshore sediment transport forced by waves is directed, in the mean, toward the NW. This brings some extra sediment in the bar area. Thus, in the final stretch of the river, some convergence occurs of river and sea driven sediment fluxes. This, added to the already rising riverbed level due to reduced precipitation and absence of flood discharges (see Figure 2.2a), led to the formation and emergence of the observed bar.

Results of the correlation of the observed data with the estuarine forcing show that the evolution of the bar is mainly driven by the river discharge and the waves. The sea water level also affects the emerged portion of the bar. Moreover, in 2019, a more complex system of bars appeared, allowing for the analysis of several forcing factors. Such factors and the related dynamics are illustrated in the following sub sections.

3.3.1 The river discharge forcing

The action of the river flow plays a fundamental role in the migration of the bar, causing rapid downriver displacements after the floods. The columns of Figure 3.8 show four events in which the bar was submerged and resurfaced downriver from where it was detected previously. Such events have been named R1, R2, R3 and R4, and were triggered by the river action, in fact peaks in the discharge and river water level timeseries were recorded in all these cases. Event R3 is characterized by two discharge peaks between which the bar did not resurface. The top panels of Figure 3.8 show the position of the bar before (blue) and after (red) the discharge occurrence, while the panels below report the estuarine forcing and the bar characteristics as explained in the previous section. Table 3.3 reports on the river discharge, the wave height, the bar area, the y-coordinate of the bar centre of mass before the occurrence of the discharge, and the bar downriver displacement made dimensionless using the river width (25 m).

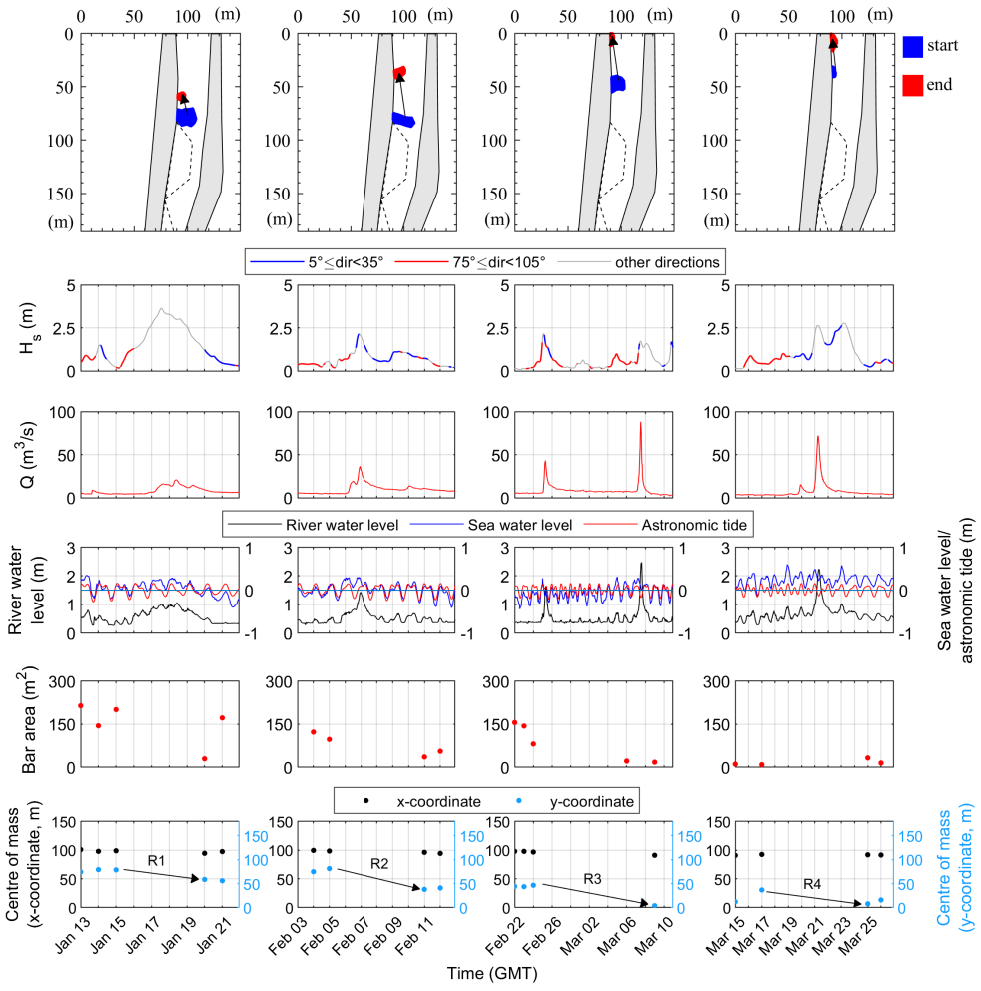

Figure 3.8: Events R1-R4 showing the downriver migration of the bar after the river discharge occurrence. The top panels represent the final stretch of the river, with the jetties coloured in gray and the dashed black line indicating the area not visible by the cameras. They illustrate the position and shape of the emerged part of the bar before (blue) and after (red) the occurrence of the river discharge. The panels below show: the wave significant height and direction, the river discharge, the river and sea water levels and astronomic tide; the area of the bar and the x- and y-coordinates of the bar centre of mass.

Table 3.4: Overview of the forcing conditions, area and dimensionless displacement of the bar for events W1-W4.

	Event W1	**Event W2**	**Event W3**	**Event W4**
H_s (m)	1.3	1	0.4	0.9
Dir (-)	NNE	NNE	E	NNE
Area (m^2)	140	172	174	81
y_{start} (m)	58.5	33.4	49.7	19.7
Δ_{bar} (-)	0.49	0.42	0.37	0.62

The comparison between the first and second events, where the bar was located at around 80 m along the y-axis of the channel (see Figure 3.2a), reveals that the extent of the bar displacement increases with the river discharge. In fact, the bar migrated farther downriver in event R2, which was characterized by a higher discharge. Furthermore, the concurrence of other two factors contributed to such result: i) the area of the bar in event R2 was half of that in event R1, favouring the mobilization of the sediment; ii) the waves were milder in event R2 and opposed less to the simultaneous river discharge.

A more interesting result can be observed looking at events R2 and R3 that were characterized by similar wave heights and bar areas. Since the third event was characterized by a maximum river discharge that was more than twice the discharge of the second event, one could have expected a larger bar displacement for event R3. However, this did not occur because the bar of event R2 was located about 35 m more upriver than the bar of the event R3, this exposing it more intensely to the action of the river. And, on the contrary, the bar of the third event was more intensively exposed to the action of the waves.

The fourth event confirms the important role of the bar location and simultaneous wave action. In fact, a discharge similar to that of event R3 produced a smaller displacement. This was due to the concurrent wave action, which was slightly stronger for event R4 than for event R3, and to the position of the bar, located around 10 m more downstream in the fourth event. Despite the very small area of the bar, the combination of all the other factors reduced the effect of the river discharge on the bar displacement.

3.3.2 The wave forcing

In the previous section, the action of the waves, as opposed to that of the simultaneous river current, has already been discussed: they reduce the effect of the river discharge, limiting the bar downriver migration.

Waves also act during longer periods (weeks to months) when the river discharge is very low, causing a gradual upriver migration of the bar. Examples of such behaviours can be observed in Figure 3.9, where the top panels give the bar centre of mass with different colors as function of the day they occurred, while the panels below show the estuarine forcing and the bar characteristics as explained in Section 3.3. The y-coordinate of the bar centre of mass, represented as light blue dots in the bottom panels, gradually increased within the analyzed periods, this meaning that the bar slowly migrated upriver. This is also clearly visible in the top panels, where the upstream displacements are highlighted by black arrows.

Furthermore, waves cause impulsive displacements of the bar that determine a "staircase behaviour" in the timeseries of the y-coordinate of the centre of mass together with a decrease of the bar area. These events are indicated as W1, W2, W3 and W4 in the bottom panels of Figure 3.9. They are associated with mild wave forcing (H_s of around 1 m) that cause upriver bar migrations usually smaller than one river width. Table 3.4 reports the wave significant height and direction, the bar area and position along the channel and the dimensionless upriver displacement for events W1-W4.

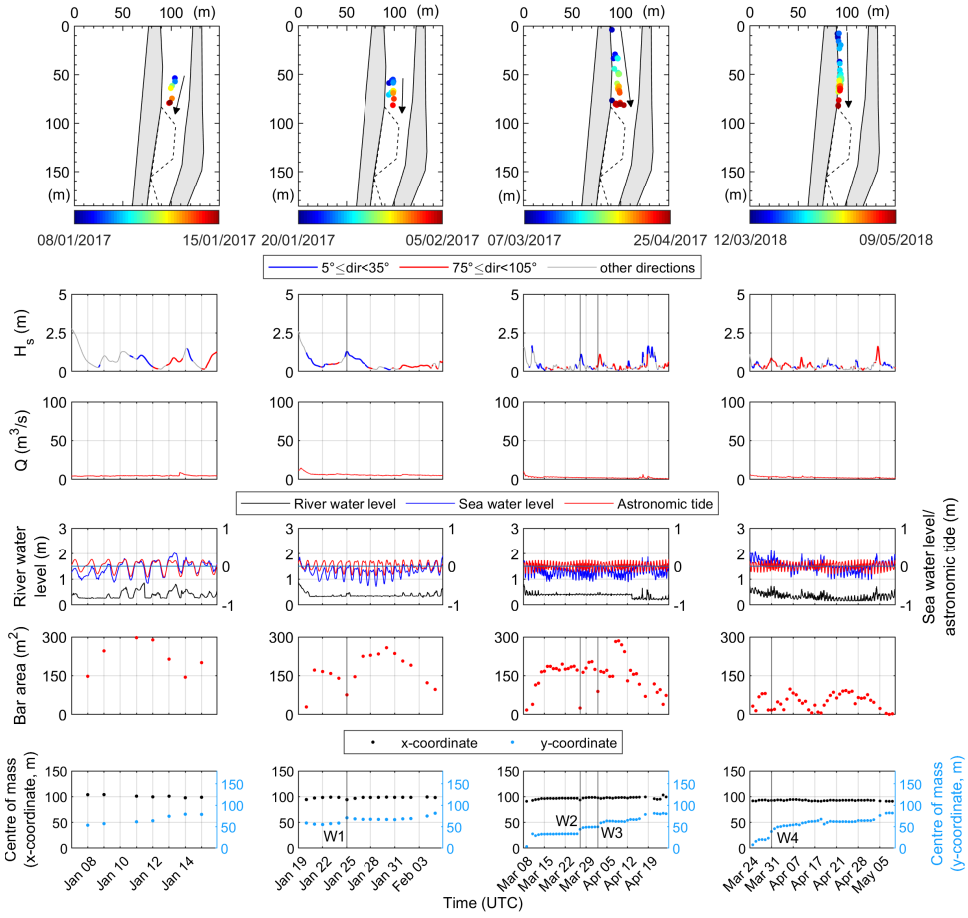

Figure 3.9: Plots showing the upriver migration of the bar due to the wave action during periods of low river discharge. The top panels represent the final stretch of the river, with the jetties coloured in gray and the dashed black line indicating the area not visible by the cameras. They illustrate the position of the bar centre of mass coloured depending on the day they occurred. The panels below show: the wave significant height and direction, the river discharge, the river and sea water levels and astronomic tide; the area of the bar and the x- and y-coordinates of the bar centre of mass.

Comparing the cases characterized by waves coming from NNE, thus directed almost perpendicularly to the estuary, the largest displacement occurred during event W4, when the bar had the smallest area and was located very close to the river mouth. Therefore, the area and the position of the bar along the channel also affect the upriver migration due to waves.

The displacements of events W1 and W2 are very similar: in fact, although the bar of the second event was located more downstream, i.e. was more exposed to the wave action, its area was larger than that of W1 and the waves were smaller. Thus, the combination of all these factors determined the entity of the bar migration.

Finally, the comparison between events W2 and W3, characterized by similar bar areas, confirms that the displacement is smaller if the bar is located more upstream and the waves are mild. Indeed, the bar migrated less during event W3 than during W2. Moreover, the third event was caused by waves coming from E, which do not enter the river mouth easily. In fact, given the shape of the MRE, oriented about 30°N, waves from NNE are those directed perpendicularly to the estuary and capable of causing the largest upriver migrations. The role of the wave direction is further analyzed in Section 3.4

3.3.3 System of two bars

In the first months of 2019, a second sediment mound was visible, downriver of the previously emerged bar. The two emerged deposits were part of the same large underwater shoal that emerged with a complex shape; however, the area of the river between these two deposits was not visible because of the limited field of view of the cameras. Thus, the hidden area was not extrapolated, but the two bars were left separated. Therefore, the last two panels of Figure 3.10a and Figure 3.10b show two different timeseries for the area and the centre of mass of the bar where full circles represent the main bar and empty diamonds represent the second emerged deposit.

Although this configuration made the analysis more complicated, some of the above-mentioned mechanisms for the evolution of the bar could be recognized. The effect of the waves could be seen in the event occurred on 23 February 2019, characterized by significant wave height of about 3.2 m coming from NNE. Before the storm, the area of the most downriver bar (red diamonds in the fourth panel of Figure 3.10a) had reached values of 534 m^2, also due to a maintenance operation carried out on 19 February 2019 to flatten the bar. The bar, already lowered by the maintenance operation, was submerged by the waves and its area abruptly decreased. However, it was not possible to observe the upriver displacement of the bar due to the wave action. This because the storm mobilized the sediment and remodeled the bar, letting it reappear with an irregular shape, which in turn caused the oscillation of the centre of mass. A decrease in the bar area occurred also for the most upriver bar (red circles in Figure 3.10a), whose centre of mass remained stable. Being the most upriver bar located very upstream, at about y=160 m, and sheltered by the most downstream bar, the waves affected only its area, lowering it because of an increase of the local water level.

Similar reductions of the area or submersions of the most upriver bar verified on 7-8 March, 18-19 March, 26 March and 4 April 2019, even under milder waves coming mainly form NNE and E. Being the area of the most downriver bar greatly reduced after the event of 23 February, its sheltering of the most upriver bar decreased, allowing also the milder waves to affect the emerged area of the upriver bar. The centre of mass of the upriver bar did not show significant migrations because the bar was located too upstream to be moved by the storms.

3.3.4 Water level induced modulation

The overall increase or decrease of the sea water level affected the emerged area of the bar, lowering or increasing it, respectively. For example, in November 2019 (Figure 3.11), the sea water level was permanently above the mean water level, this probably contributing to the reduction of the bar emerged area from 500 m^2 to 26 m^2. In contrast, during February 2019, the sea water level decreased from about 0.2 m to

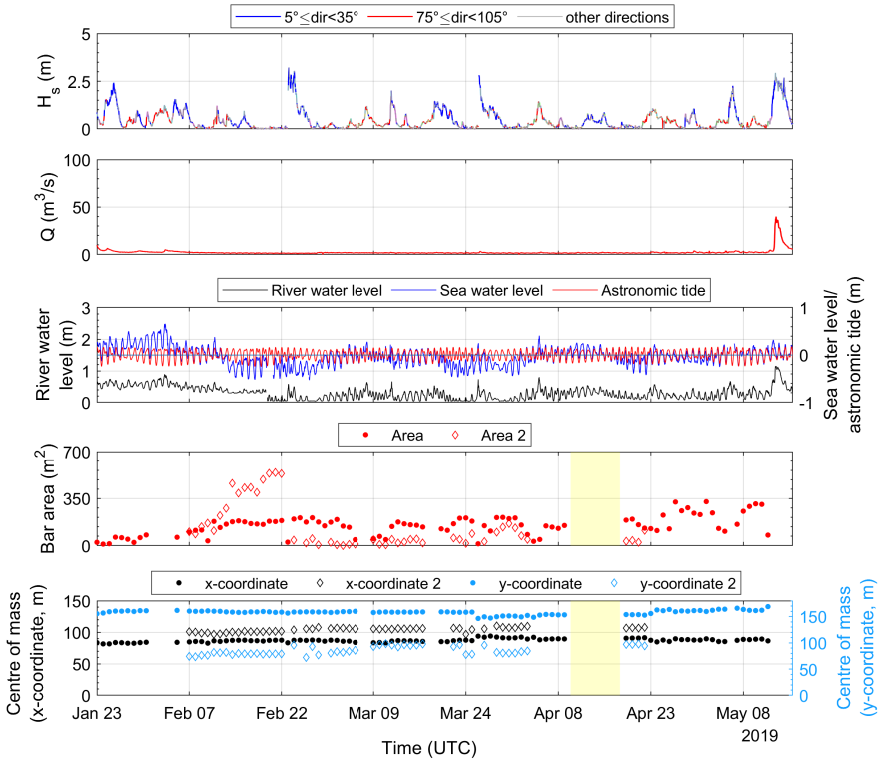

(a)

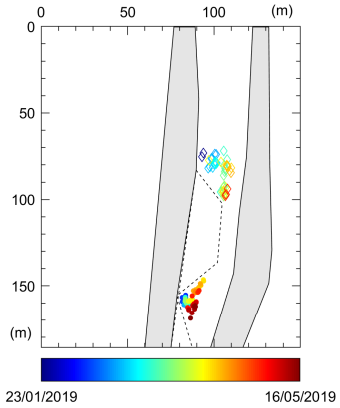

(b)

Figure 3.10: a) Plot showing the period of coexistence of two emerged deposit. The five panels show: the wave significant height and direction, the river discharge, the river and sea water levels and astronomic tide; the area of the bar and the x- and y-coordinates of the bar centre of mass. Periods of time when observations from the SGS station were unavailable are highlighted in yellow. b) Final stretch of the river, with the jetties coloured in gray and the dashed black line indicating the area not visible by the cameras. The positions of the bars' centre of mass are coloured depending on the day they occurred. Empty diamonds and full circles represent the most downriver and the most upriver bar, respectively.

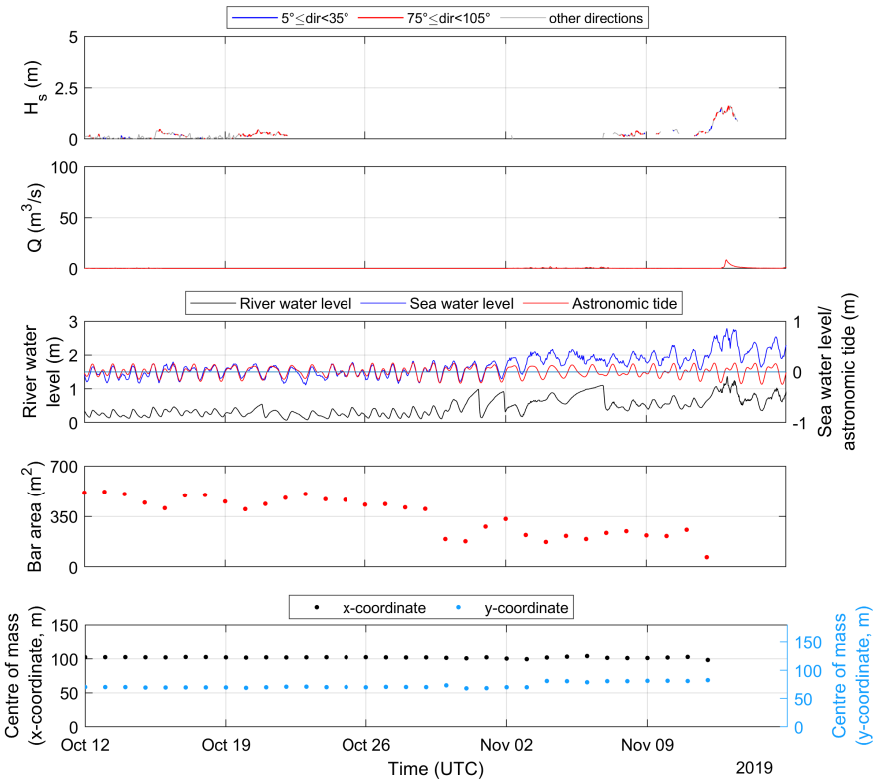

Figure 3.11: Plot showing the effect of a rising sea water level on the bar emerged area. The five panels show: the wave significant height and direction, the river discharge, the river and sea water levels and astronomic tide; the area of the bar and the x- and y-coordinates of the bar centre of mass.

about -0.5 m and the emerged area of the bar significantly increased from 41 m^2 to 534 m^2 (red diamonds in the fourth panel of Figure 3.10a).

The effect of the tide and, more precisely, of its phase shift to the other forcing peaks, is discussed in Sections 3.4.1 and 3.4.2.

3.4 Simulation results

3.4.1 Parametric simulations - hydrodynamics

The results of the simulations forced with increasing river discharges show that, as expected, the velocity inside the channel increases with the river discharge. Figure 3.12a reports the timeseries of the mean velocity in a cross section located in the area of the sediment deposit (solid lines). It also shows the mean bed shear stress (dashed lines) in the same section, highlighting the direct proportionality between the velocity and the stress. The bed shear stress represented in the figure was made dimensionless using the critical bed shear stress for erosion imposed in the simulations. Therefore, a value above 1 means that the cohesive sediment fraction is mobilized. The velocity produced by the 10 m^3/s river discharge does not cause the bed shear stress to exceed the critical one, thus it does not trigger any resuspension of cohesive sediment. For the R50 and R100 cases, instead, the bed shear stress reaches values 20 and 92 times higher than the critical one, respectively. Figure 3.12b shows the velocity and the dimensionless bed shear stress of the R50 case, at the river discharge peak, along a section spanning from 550 m upstream of the river mouth to 220 m offshore. The maximum current speed, and consequently the major stress, verifies in the area of the river channel where the bar is located (see also Figure 3.4b). Here, the section narrows causing some acceleration of the water.

When the peak of the river discharge is combined with high and low tide, both

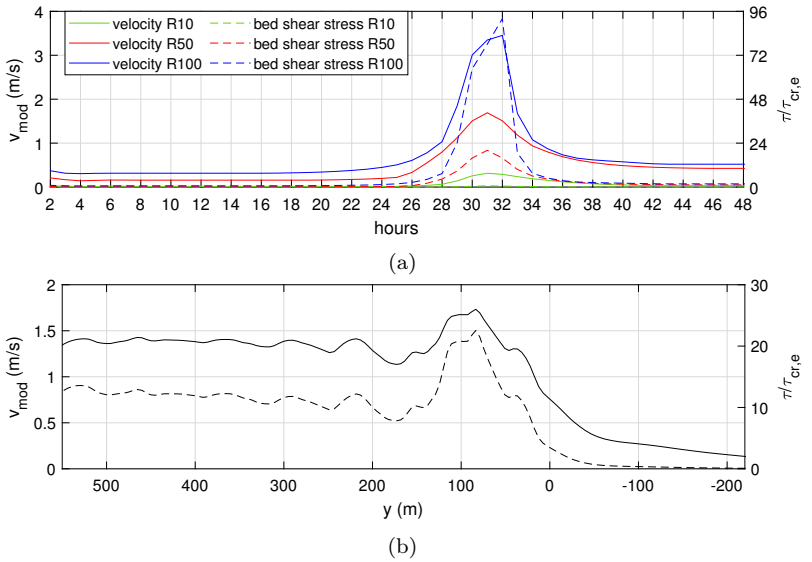

Figure 3.12: a) Mean velocity (solid lines) and mean dimensionless bed shear stress (dashed lines) in a cross section located over the bar. Green, red and blue colours identify the R10, R50 and R100 cases. b) Velocity (solid line) and dimensionless bed shear stress (dashed line) for the R50 case, at the river discharge peak, in a sections spanning from 550 m upstream of the river mouth (positive y-values) to 220 m offshore (negative y-values).

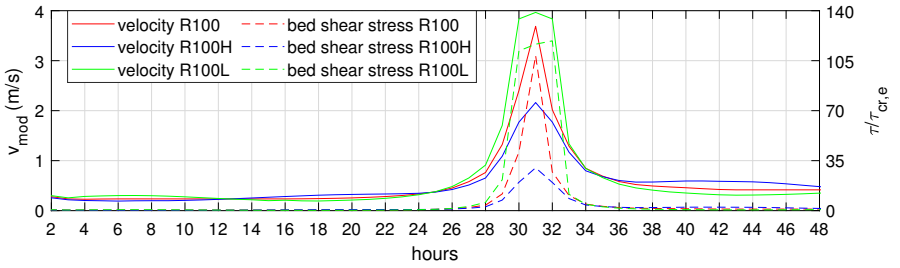

Figure 3.13: Mean velocity (solid lines) and mean dimensionless bed shear stress (dashed lines) in a cross section located just inside the river mouth. Red, blue and green colours identify the R100, R100H and R100L cases.

the flow velocity and the bed shear stress are affected (Figure 3.13). The increase in water levels due to the high tide caused the river flow to slow down from 3.7 m/s to 2.2 m/s. Consequently, the shear stress became less than a half of the shear stress without tide. On the contrary, the low tide forced lower water levels that speeded up the flow to values of 4 m/s, causing an increase in the shear stress.

The simulations with waves as unique forcing reveal that the waves can enter the estuary, as shown in Figure 3.14. The simulated storms are characterized by a wave height peak of 2 m, as many of the storms of medium intensity that hit the coast of Senigallia, and 5 m, comparable to the 10-years return period local waves. NNE waves, approaching the coast almost perpendicularly to the MRE, easily penetrate the river channel, with H_s >0.5 m up to 150 m upriver of the river mouth (right panels of Figure 3.14). The left panels of Figure 3.14 show that the fronts of E waves rotate due to the refraction process, becoming more and more parallel to the shoreline as the waves approach the coast. Hence, also E waves can propagate inside the estuary. The main difference between the two storm directions is not the extent up to which the waves propagate, but the wave height inside the channel, which is around 0.3 m higher for NNE waves than for E waves. Figure 3.15 shows that the wave-driven currents create a gyre inside the channel, with upriver and seaward velocities along the left and right riverbanks, respectively. The current intensity, similar for the two wave directions, reaches maximum values of 0.4 m/s adjacent to the west riverbank, just inside the river mouth. The gyre extends slightly more upriver for NNE waves.

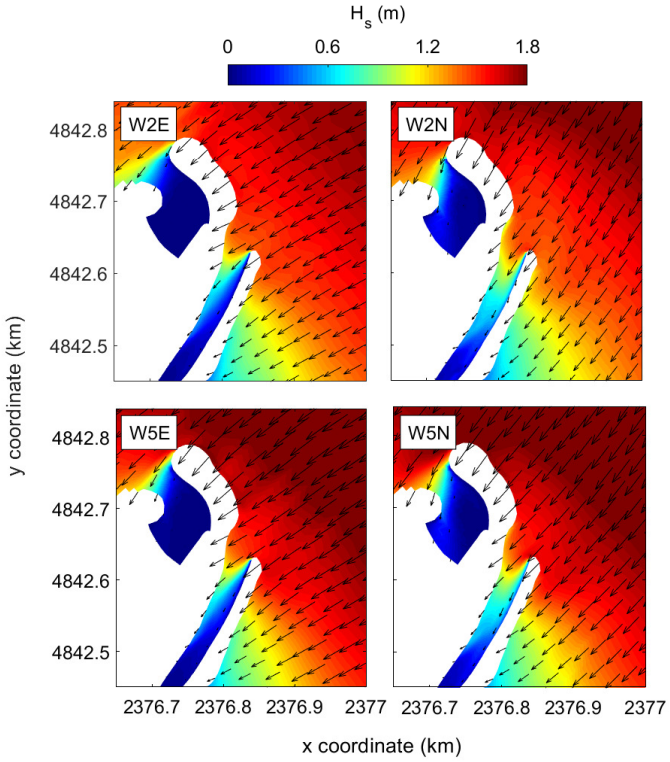

Figure 3.14: Maps of significant wave height for W2E (top-left), W5E (bottom-left), W2N (top-right) and W5N (bottom-right) simulations. Arrows give the wave direction.

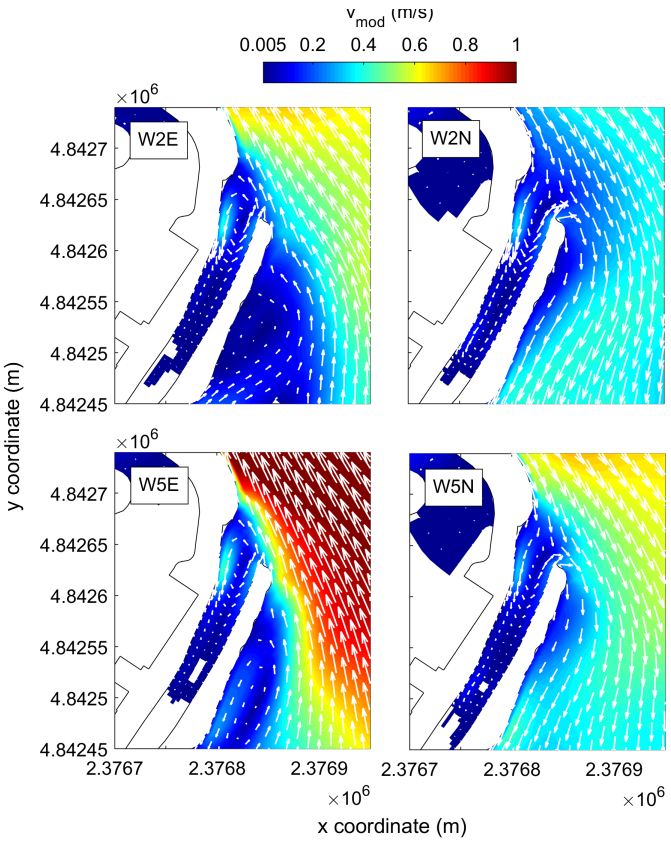

Figure 3.15: Maps of the wave-induced currents inside the MR channel. Arrows give the velocity direction. Currents below 0.005 m/s are not shown.

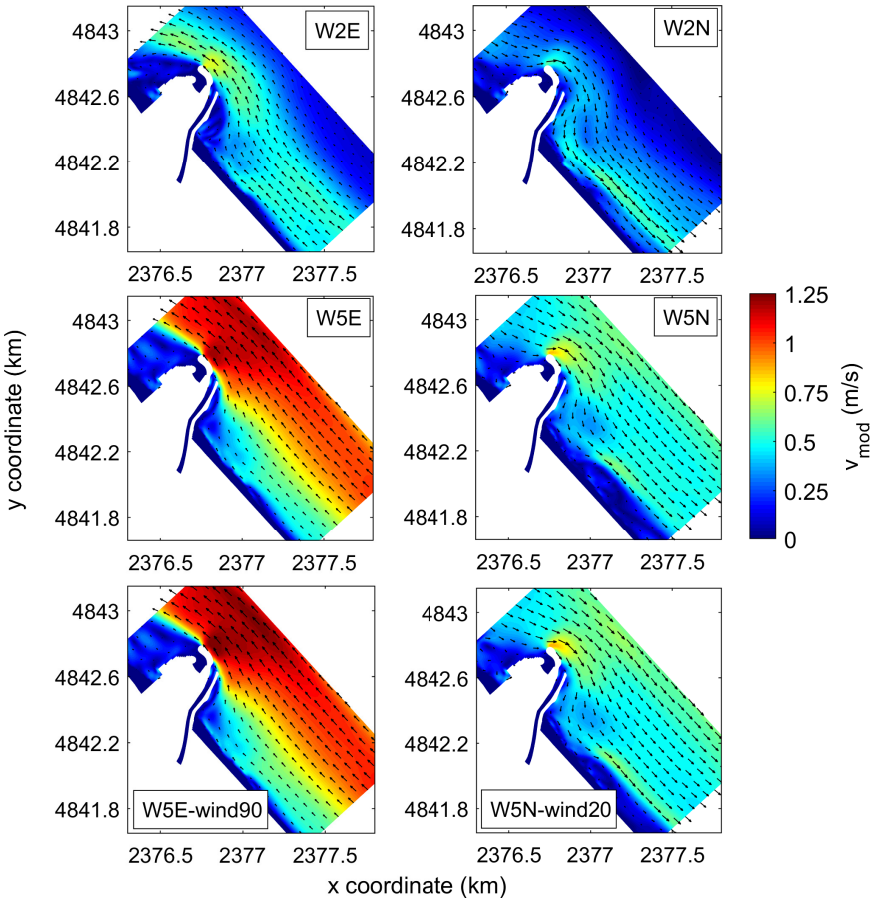

Figure 3.16: Maps of the wave-driven currents, with the arrows giving the velocity direction.

Comparison between the top and bottom panels of Figure 3.14 reveals that the wave height inside the channel does not change significantly (less than 10 cm) even if the value of the offshore wave height increases from 2 m to 5 m. This is a consequence of the wave breaking occurring at the river mouth that causes the reduction of the wave height and the dissipation of the wave energy. Such energy is in part transferred to longshore currents, visible in Figure 3.16. For both the analyzed wave directions, the current intensity increases with the wave height. Moreover, for the mildest waves, the currents develop just outside the river mouth and alongshore, within an area of around 300 m from the shoreline. On the other hand, the highest waves trigger a current field that extends farther offshore. This is again due to the wave breaking that occurs more offshore for the waves characterized by H_s=5 m. Hence, the energy of these waves is transferred to the currents at a larger distance from the shore. Currents generated by E waves are more intense than those triggered by NNE waves because of their longer fetch. Such difference is clearly noticeable in the middle panels of Figure 3.16, showing that the intensity of the E waves-driven currents is twice that produced by NNE waves. Furthermore, the comparison between the middle and bottom panels of Figure 3.16 reveals that the wind slightly contributes to increase the current velocities (up to 8%).

Finally, Figure 3.17 shows the maps of the dimensionless bed shear stress at the storms peak. The maximum values, of about 12 for both the wave directions, occur just inside the river mouth. Moving into the channel, waves from the NNE induce a shear stress higher than that caused by E waves. The comparison between the values in Figure 3.17 and those in Figure 3.12a highlights that the shear stress forced by 5 m-height waves, comparable with 10-years return period waves, is at least half of the maximum values produced by river discharges associated to return periods smaller than 1 year. This means that a yearly-typical river discharge generated a riverbed erosion more intense than that triggered by a 10-years return period wave storm.

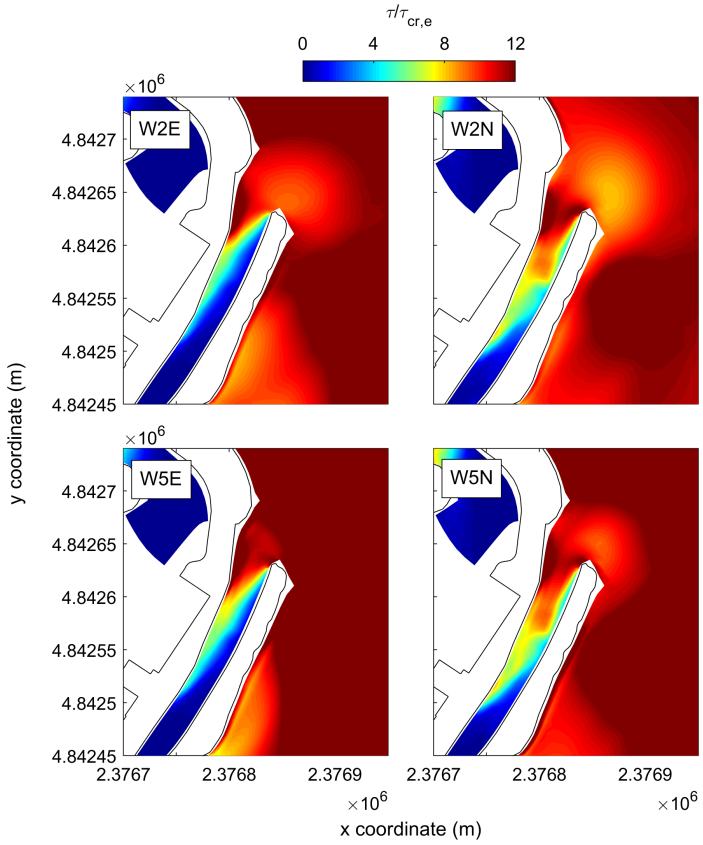

Figure 3.17: Maps of the bed shear stress made dimensionless with the critical shear stress for erosion.

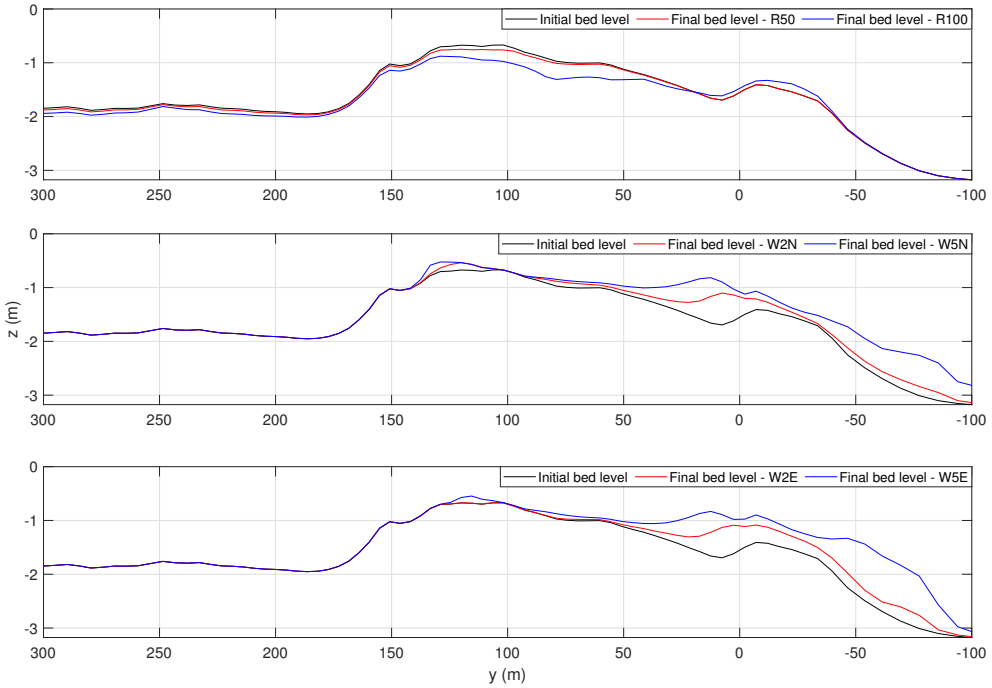

Figure 3.18: Results of the parametric simulations. The top panel shows the evolution of the bed for the river discharge only simulations: the black solid line represents the initial bed level; the red and blue lines represent the final bed level for the simulations with Q=50 m^3/s and Q=100 m^3/s, respectively. The middle and bottom panels show the evolution of the bed for the wave only simulations, respectively for NNE and E waves: the black solid line represents the initial bed level; the red and blue lines represent the final bed level for the simulations with 5 m and 2 m wave height, respectively. The bed level represents the distance from the mean water level to the riverbed, negative downward.

3.4.2 Parametric simulations - morphodynamics

The results of the parametric simulations, run to separately highlight the role of the river discharge and the waves, are illustrated in Figure 3.18, which reports the section along the left riverbank extracted from the bathymetry using the reference system of Figure 3.2a.

The top panel of Figure 3.18 shows the evolution of the riverbed for the simulations with input peak discharges equal to Q=50 m^3/s and Q=100 m^3/s. At the end of the simulation, the riverbed is eroded both in the upper channel and bar location, while deposition occurs just out of the river mouth. The highest discharge, comparable to the 1-year return period discharge, erodes about 9 cm along the river (6 more cm than the lowest discharge) and a maximum of 37 cm on the bar (27 more cm than the lowest discharge), this suggesting an erosion directly proportional to the discharge intensity. In particular, doubling the discharge leads to an erosion about four times larger. Such numerical results cannot directly be compared with the discharge events R1-R4 because of different bathymetries and durations. The real-life cases showed the evolution of an emerged bar during about five days, while the simulations gave the modification of the riverbed, characterized by a large submerged deposit, during two days. However, the behaviour modeled by the simulations is the same of the observed one, this reinforcing the results. In fact, the R1-R4 observed events showed the submersion of the bar due to the river discharge, this suggesting bar erosion, also predicted by the simulations. Moreover, the sediment displacement toward the sea is also recognizable, even if larger than the observed one, due to the differences between the modeled and observed scenarios. The modeled downriver bar migration was computed as the difference between the lowest eroded and highest deposited portions of the riverbed. The dimensionless displacements are in the order of 4 river widths, more than double of the observed migrations, which were all smaller than 2 river widths.

The middle and bottom panels of Figure 3.18 show the riverbed evolution for the simulations run with NNE and E waves, respectively. The waves bring sediments inside the river mouth, causing the crest of the most seaward bar to grow and move upriver. As for the river discharge, also the displacement due to the wave action increases with the forcing strength. Regardless of the direction, the most intense storms causes accretions of about 60 cm and displacements of 0.78 river widths of the most seaward bar. The accumulations determined by the mildest waves are smaller, around 30 cm, and the upriver shifts depend on the wave direction, being 0.58 and 0.39 river widths respectively from NNE and E waves. The portion of the bar located about 120 m upstream from the river mouth is also affected by waves, even if slightly. The 5 m-NNE waves causes the largest modification, increasing the crest height of 15 cm and pushing it upriver. The 2 m-NNE waves and the 5 m-E waves only produce an accumulation of sediments of around 10 cm, without triggering any displacement. Finally, the 2 m-E waves do not modify the bed level. These results confirm that the north-easterly waves could easily enter the estuary, reaching farther locations along the channel and thus modifying the upriver portion of the deposit more than easterly waves (see also Figures 3.14 and 3.15). On the other hand, storms from the E produce a larger deposition of sediment just outside of the river mouth. This is probably due to the geometry of the channel that let the E waves overstep the east jetty (shorter than the west jetty) and hit the west jetty, with a consequent accumulation of sediment adjacent to the left bank. Both waves do not affect the inner slope of the bar and the upriver evolution.

The effect of the tide is visible in Figure 3.19, where the blue and green lines represent the final bed level when the river discharge peak (or the wave storm peak) is simultaneous with the high and low tide, respectively, while the red line represent the final bed level for the river discharge only (or waves only) simulations. The tide phase shift to the discharge peak plays a significant role, as clearly visible in the top panel of Figure 3.19. When the discharge peak is simultaneous with the high tide, the erosion of the bar is some centimetres smaller than that caused by the discharge only (compare blue and red lines in the top panel of Figure 3.19). The high tide determines higher water levels in the estuary, this slowing the river current and reducing its effect on the bar. On the contrary, the river flow is speeded up by the low tide, causing larger bar erosion (green line in the top panel of Figure 3.19). Such tidal influence on the bar evolution was not observed in the real-life events because of the micro-tidal setting of the MRE, where 60 cm of tide excursion, as the one applied in the simulations, are rarely reached. Moreover, the entity of the erosion cannot be precisely quantified from the images that only provide qualitative information about the bar height.

The middle and bottom panels of Figure 3.19 reveal that the tide has a very minor influence on the wave action, being the red, blue and green lines almost superimposed.

The above analysis reveals that the 10-years return period waves induce a much smaller bar migration than the 1-year return period discharge, this clarifying the dominance of the sediment expulsion out of the river mouth by the river discharge over the upriver transport by the waves. Moreover, the simulation results confirm the important role of the bar location along the channel. In fact, the evolution of the most upriver bar, directly exposed to the river current, is more affected by the discharge than by the waves. On the contrary, the seaward portion of the deposit is largely modified by the wave action, while only slightly by the river flow. Finally, the tide phase shift to the discharge peak strengthens or reduces the effect of the river action, respectively when low or high tide occurs simultaneously with the discharge peak.

3.4.3 Real-life simulation

The real-life event of 18 March – 2 April 2018 was reproduced with Delft3D to model a combination of forces and critically compare the results of the numerical simulations with the observed data. The observed data (see Figure 3.6) showed the presence of the bar, with a very small, emerged area, for some days until 17 March. The centre of mass remained around 12 m along the y-axis, apart from 17 March, when the bar appeared at about 37 m. This suggested the presence of a larger submerged deposit,

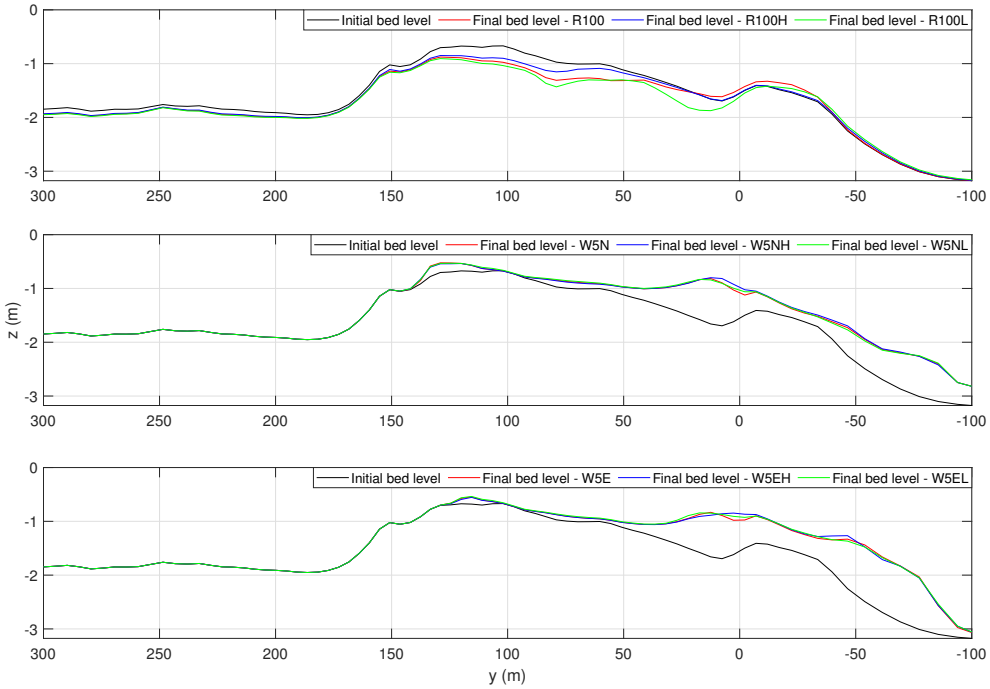

Figure 3.19: Results of the parametric simulations. The top panel shows the evolution of the bed for the river discharge only simulations and the combination of river discharge and tide. The black line represents the initial bed level; the red line represents the final bed level for the simulation with Q=100 m^3/s; the blue and green lines represent the final bed level for the simulations with Q=100 m^3/s simultaneous with high and low tide, respectively. The middle and bottom panels show the evolution of the bed for the wave only simulations and the combination of waves and tide, respectively for NNE and E waves. The black solid line represents the initial bed level; the red line represents the final bed level for the simulations with 5 m wave height; the blue and green lines represent the final bed level for the simulations with 5 m wave height simultaneous with high and low tide, respectively.

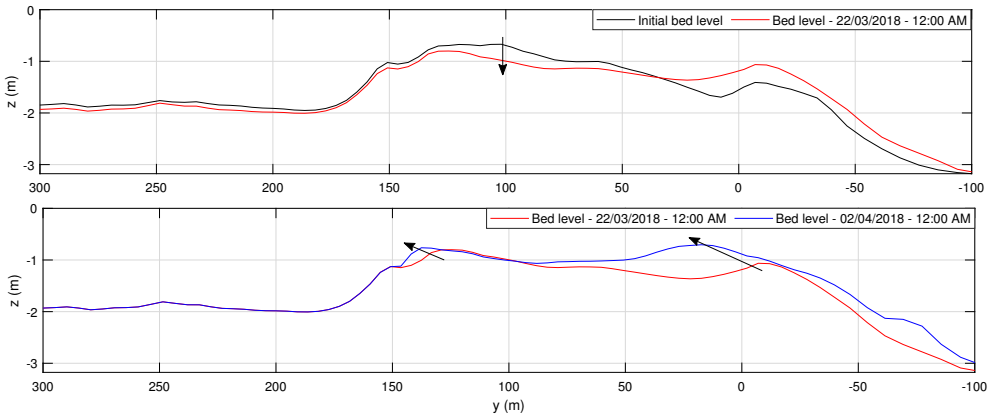

Figure 3.20: Results of the simulation of the real-life event: the panels report the riverbed evolution along the longitudinal section adjacent to the left riverbank (see Figure 3.4b. The bed level represents the distance from the mean water level to the riverbed, negative downward. The evolution of the riverbed was divided into two panels to better highlight the effects of the river discharge and of the waves.

emerging in different parts depending on the forcing condition. In fact, the small E wave storm that occurred on 16 March could have mobilized the sediment, letting the bar emerge more upriver. On 21 March, a storm with wave height peak of about 2.6 m occurred simultaneously with a river discharge reaching about 72 m^3/s. The effect of such event could not be observed directly from the images because the bar was submerged, but one could expect that the effect of the river discharge was not so intense because of the concurrent wave storm and the position of the bar, located quite downriver. Then, on 23 March a second storm, with a wave height peak of 2.8 m, occurred. The remodeling of the deposit by the discharge and the waves caused the bar to emerge again, on 25 March, very close to the river mouth, at around 8 m, as before 17 March. In the following days, the bar migrated upriver until reaching around 45 m on 2 April, under mild wave climate. During all the period, the x-coordinate of the centre of mass remained around 91 m, suggesting that the bar remained anchored to the west riverbank.

The simulation results should show both the effect of the river flow and the waves. In particular, since the peaks in discharge and wave height occurred on the same day and were followed by a second wave height peak two days later, it is expected that the river would not have caused a significant downriver sediment transport (as, for example, in 2017). However, the discharge is still supposed to cause some riverbed erosion. On the other hand, upriver sediment transport due to storm waves is expected.

Figure 3.20 shows the evolution of the modeled bed level along the longitudinal section adjacent to the west riverbank, where the bar is located. The black curve in the top panel represents the initial bed level, characterized by two main crests. The red line identifies the bed level after both the peaks in discharge and wave height; an accumulation (about 34 cm) of sediment occurred at the location of the most seaward crest, while the other crest, more directly exposed to the river flow, was eroded (max 31 cm, indicated by the black arrow). Moreover, the riverbed upstream of the bar was also slightly eroded (about 8 cm). As expected, some significant erosion of the bar occurred as due to the river discharge. Then, the storm occurred on 23 March 2018 pushed the sediments inside the river mouth and caused an increase in height of the outer crest, as shown in the bottom panel. The blue line represents the final bed level after the occurrence of the second wave storm and the following milder waves. It clearly shows the accretion and upriver translation of the crests (indicated by the black arrows). The simulations confirmed that waves were responsible for some upriver sediment transport and migration of the deposit. The most evident displacement and accumulation occurred for the most seaward bar crest, that translated some 24.4 m upstream and increased in height by about 35 cm.

Chapter 4

Study of the MR plume

The MR belongs to a small-scale river system with a typical torrential regime. Despite its modest dimension, it carries a large amount of sediment that spreads into the middle Adriatic Sea. This abundant sediment transport is mainly due to the erodibility of the fractured rocks that constitute the Apennine Mountains. However, some local mechanisms occurring at the river mouth could contribute to the riverbed mobilization and sediment resuspension. This study focuses on such local processes, with the aim of identifying the plume generation mechanisms. Besides the well-known link between the river flow and the plume occurrence, here the capability of waves to trigger some sediment resuspension is also investigated.

Once the plume exits the river mouth, its spreading in the sea is driven by some transport mechanisms, different from those affecting sediment dispersal in large-scale river systems. Moreover, being the MRE located in a micro-tidal environment, the tide is expected to play a minor role in the plume evolution.

Both generation and transport mechanisms have been studied through the integration of the observed data, described in Section 4.1, with the numerical simulations, included in Section 4.2. Sections 4.3 and 4.4 present the results.

4.1 Analysis of the video monitoring products

4.1.1 Tracking of the plume front

The orthorectified and stabilized images of the SGS video-monitoring station were used for a quantitative analysis of the plume extension. The plume front was manually tracked on the images (yellow line in Figure 4.2) and the offshore extent of the plume was computed as the maximum distance of the plume front from the y-axis of the local reference system chosen for the analysis (blue lines in Figure 4.2). The origin of the reference system was placed at the river mouth; the x-axis was in the alongriver direction, while the y-axis, perpendicular to the x-axis, was almost in the alongshore direction. Since the manual tracking of the plume front is a subjective operation, the error associated with such procedure was evaluated through the comparison of the fronts tracked by different people, for 183 cases. The mean absolute errors for the plume front position and extension were about 18 m and 14.4 m, respectively, while the mean relative error for the plume extension was about 5.6%.

Another check was done using the Sentinel-2 images (Figure 2.6b) of the MRE area, where the plume front was detected and its extension computed with the same procedure used for the SGS images. The temporal resolution of the Sentinel-2 products was of five days, this making it impossible to observe as many plume events as for the SGS images. Moreover, the cloud cover contributed to further reduce the number of usable satellite images. Anyway, for times when the two image types were available, the plume fronts tracked from SGS and satellite were compared and showed a good overlap, like that of Figure 4.2. Such a good agreement was not found for the plume extensions since that computed from the Sentinel-2 images was generally larger than that obtained from the SGS images (Table 4.1). This was because the satellite covered

Table 4.1: Comparison between the plume extensions computed from the SGS and the satellite images.

Date	**SGS extent**	**Satellite extent**
	m	m
7 Mar 2016	116	162
12 Mar 2017	326	494
21 Apr 2017	107	131
6 Apr 2018	332	451
31 Jan 2019	415	662
5 Feb 2019	84	83
17 Mar 2019	287	269
31 May 2019	177	246
8 Set 2019	312	1482
7 Dec 2019	180	255

a wider area, allowing to see the plume evolution further away from the MRE, where it might reach a dimension bigger than that observed near the video-monitoring system. Figure 4.1 reports the images of 8 September 2019, when the difference between the two extensions was the maximum observed.

Oblique images from the ISPRA video system (Figure 2.6a), available since May 2016, were used to qualitatively correlate with the findings from SGS and satellite images and to inspect the distance reached by the plume in the southeast direction.

4.1.2 Particle Tracking Velocimetry analyses

Particle Tracking Velocimetry (PTV) is a Lagrangian technique to measure velocities and trajectories of moving objects that are suspended in a fluid flow. In the last decades, the PTV has been increasingly used in fluvial setting. Originally developed to conduct hydraulic analysis in controlled, laboratory settings, PTV is becoming a novel approach for non-contact remote sensing of flow in rivers. This technique shares many principles to that of the lab-based image velocimetry, such as the seeding of the flow with neutrally buoyant particles, the video recording of the seeded flow and the computation of particle displacements by some detection/tracking algorithms. The key stages of a large-scale PTV are the capture optimisation, the pre-processing, the image processing and the post-processing [37].

Here, PTV analyses were performed on several videos acquired by the SGS station. Since the video-monitoring system was not installed with such aim, the capture setting was not designed to obtain optimal conditions for the PTV. However, SGS satisfies one of the most critical requirements for the success of the tracking algorithm. In fact, the size of the ground sampling distance, that is the distance between the centroid of two adjacent pixels, is smaller than the features to detect, this allowing their identification from the images. Moreover, the tracer characteristics were not ideal for PTV purposes because natural features were used as seeding, such as branches and debris floating on the water surface and advected by the flow. Therefore, the spatial and temporal distribution of tracers was not controlled, as well as their size and shape. The tracer particle should have a size/shape stable over time, while the natural seeding present in the videos could change shape because of the aggregation/disaggregation of the finer particles. One more problem was linked to the visibility of the floating objects, that could be altered by inhomogeneous lighting or fog that increased the noise and hindered the traceability of surface patterns. Moreover, in this particular application, the analyzed area was placed just upstream of the river mouth, thus the wave entering

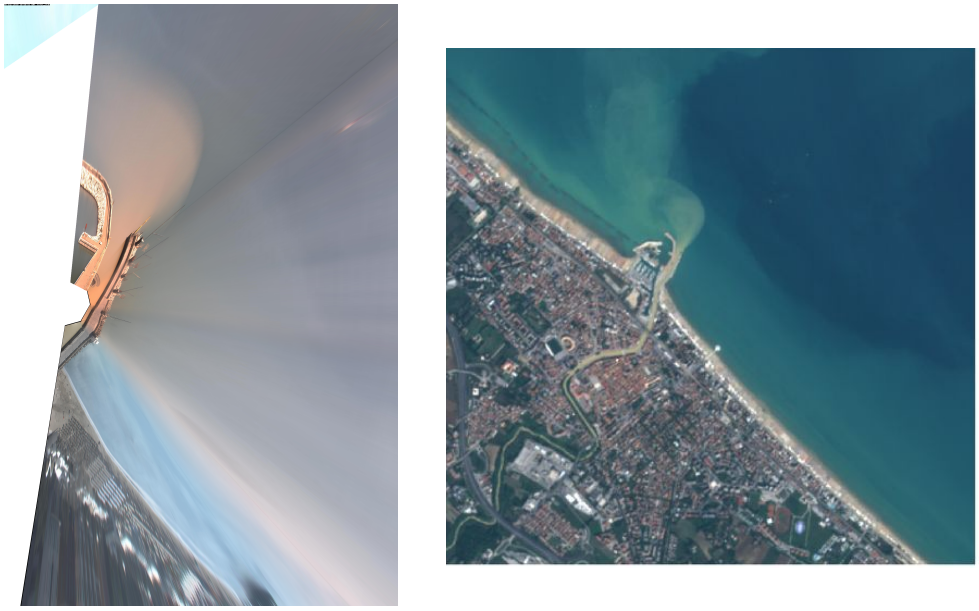

(a) (b)

Figure 4.1: Images acquired on 8 September 2019 at 10:00 AM by a) the SGS video-monitoring station and b) Sentinel-2.

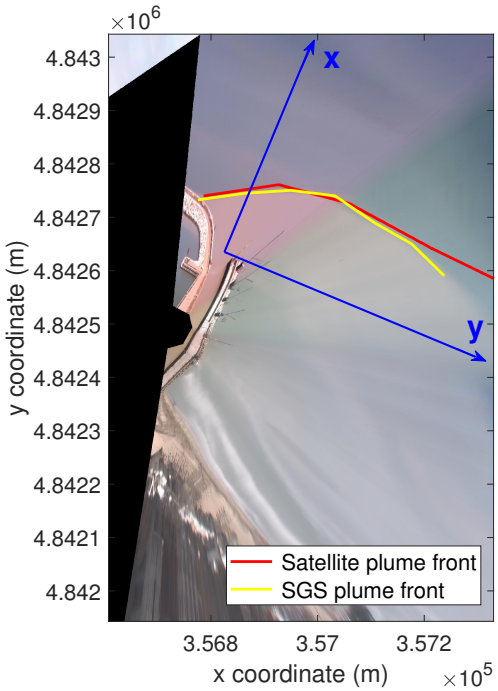

Figure 4.2: Plume front tracked from SGS (yellow line) and satellite (red line) images, superimposed on the Timex image of 31 May 2019 (10:00 AM), with the blue lines identifying the local reference system.

inside the estuary contributed to disturb the flow, submerging the tracers and causing the loss of tracer visibility.

Some suitable videos of camera C3 of the SGS station were chosen, as they showed visible floating material on the water surface. The decision of using only the C3 camera was made to: i) restrict the analyzed area to the final reach of the river to simplify the already difficult analysis and ii) exploit the camera with the best capture setting for PTV purposes. Video frames (Figure 4.3a) were extracted, stabilized and orthorectified. Image stabilization was important to correct the camera movement mainly caused by the wind, while the orthorectification could be applied either to the image before the analysis, like in this case, or to the resultant vector field. Then, the images were further pre-processed to reduce interferences and enhance visibility of the tracers. In fact, the PTV requires well-defined bright particles against a clean, dark background. The first operation performed was the conversion of the image from multi-band to grayscale by eliminating the saturation and hue, while keeping the luminance (Figure 4.3b). The second step consisted in applying the MATLAB function *fibermetric* [22] to highlight tubular or elongated shapes, thus allowing to emphasize the visibility of the floating material. After switching colours between background and foreground, setting a dark background and a bright foreground, the contrast of the images was improved to help tracers stand out as much as possible against their background. The intensity values in the input image that fell between a range defined by the user were mapped into values between 0 and 1 in the output image. This allowed us to highlight the floating material and to reduce some noise produced by wave breaking. However, some disturbances due to waves and water ripples remained. Therefore, a mask was applied to cover the jetties and, in the most critical cases, also the stretch of river disturbed by the waves (Figure 4.3c).

Once the images were modified, the analysis was carried out with the MATLAB software package *Part2Track*, developed at the Institute of Mechanics and Fluid Mechanics at the TU Bergakademie Freiberg [35]. *Part2Track* uses a four-frame matching algorithm to correctly identify and link particles from one image frame to the next. Thus, the information from four consecutive frames are exploited to establish links between particles in the middle two of the four frames, this technique being recognized as one of the most effective [46]. An accurate detection of the tracer is achieved by a Laplace or Gaussian filtering technique, depending on a single scale parameter δ_i. Such approach yields a filtered image with a strong positive response in the presence of objects of scale δ_i. Position of the object centroids are then obtained by searching for the local maximum in the filtered image. Sub-pixel resolution of the object position is achieved by fitting either a quadratic or a Gaussian function to the pixel intensity values around the centroid position, and finding, then, the position of the maximum of such function [31]. Furthermore, an outlier detection has been implemented in the form of the widely used "median test", which uses a detection threshold for spurious vector data specific to each experiment, or different flow regions within the domain. The advantage of the modification of the classical algorithm is the use of a single threshold that is applicable to a variety of flow conditions without any a priori knowledge of the flow characteristics [90].

Before running *Part2Track*, the user must provide some parameters that include information about the experiment (image acquisition mode, resolution of the recorded images, number of images, time separation, conversion scale mm/px and a pre-defined image mask) and the displacement calculation (a.o., particle size and brightness, matching method, field of search, size of particle neighbourhood, threshold for outlier detection). Such parameters must be adapted to each analyzed video.

The result of the analysis was a set of trajectories of the detected particles. Moreover, the velocity vectors associated to each detected particle in each computed frame were also provided. Interpolation of the scattered data on a regular grid provided the surface velocity field (Figure 4.3d). To correlate the velocity obtained by the PTV analysis with the river discharge, we extrapolated one single representative value of velocity for each video, computing a weighted mean of the velocity field, using as weights the number of particles detected by the *Part2Track* algorithm in each grid cell ("PTV velocity").

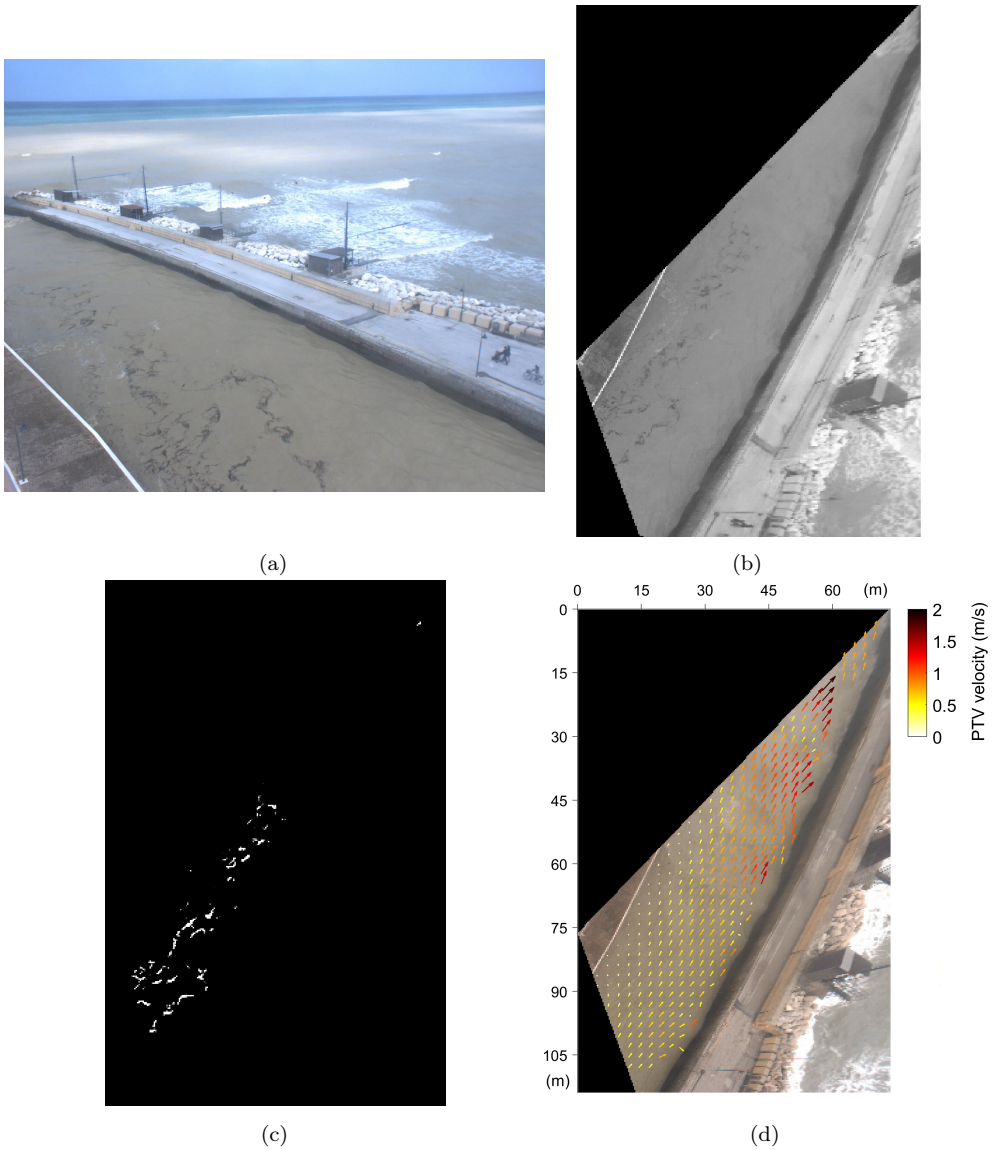

Figure 4.3: Phases of the PTV analysis: a) extraction of the oblique frames acquired by the camera C3; b) orthorectification, stabilization and conversion to grayscale; c) identification of the elongated shapes and contrast enhancement; d) interpolated surface velocity vector field.

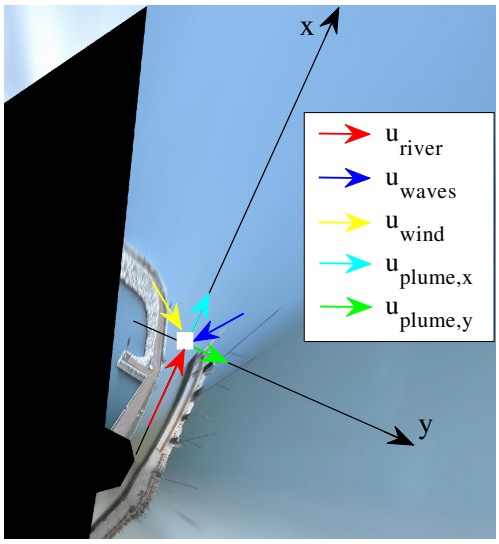

Figure 4.4: Reference scheme for the computation of the plume velocity components. The river flow contribution is represented by a red arrow, totally directed along the x-axis, while the blue and yellow arrows symbolize the waves and wind contributions with an arbitrary direction. The resultant x- and y-components of the plume surface velocity are identified with the cyan and green arrows.

4.1.3 Computation of the plume velocity components

A further analysis was, then, performed to look for a relationship between the plume extension and velocity. Since the plume evolution was affected by a combination of factors, the plume surface velocity, u_{plume}, was computed accounting not only for the action of the river, but also for the wave and wind forcing. The surface velocities due to such forces were calculated at the river mouth and decomposed along two orthogonal axes, shown in Figure 4.4: the x-axis was directed along the river, while the orthogonal y-axis pointed to SE and was directed almost alongshore. Figure 4.4 also gives a scheme of the forces involved, the red, blue and yellow arrows representing the river flow, the waves and the wind contributions, respectively, while the cyan and green arrows symbolizing the resultant plume velocity components. The effect of the tide was neglected because, for the analyzed cases, the tidal excursion was small, less than $\pm$ 0.15 m. Therefore, even if the tide could modify the plume extension as shown by the parametric simulations in Section 4.5.1, in the real cases studied here it was not regarded as one of the main factors.

The "PTV velocity" was taken as representative of the river surface velocity, u_{river}, and pointed in the positive x-direction.

The surface water velocity generated by the wind stress, u_{wind}, was related to the wind speed through a factor of 3.2% [29].

The surface water velocity due to the wave motion, u_{waves}, was computed as a Stokes drift [85], using the Ursell formula valid for general water depths:

$$u_{waves} = \frac{c_w (ak)^2 \cosh(2k(h+z))}{2\sinh^2(kh))} \tag{4.1}$$

where $c_w = \sqrt{\frac{g}{k}\tanh(kh)}$ is the phase speed, $k = \frac{2\pi}{\lambda}$ is the wave number, $a = \frac{H}{2}$ is the wave amplitude, h is the water depth and z is the vertical coordinate (equal to zero at the free surface). The wave height H at the mouth was obtained by transferring to shore, through Delft3D, the offshore data either measured at the Meda station or provided by Copernicus, depending on their availability (see Section 2.2); the wavelength λ was computed through the dispersion relation, given the water depth and the wave frequency. Both u_{wind} and u_{waves} were decomposed in the x and y-directions.

Finally, the surface plume velocity components were calculated:

$$u_{plume,x} = u_{river} + u_{waves,x} + u_{wind,x} \tag{4.2}$$

Table 4.2: Video-monitoring products used for the study of the MR plume

Data type	**Time coverage**	**Acquisition frequency**	**Use**
SGS images	2016–2019	13 images/day (5 AM–5 PM)	plume tracking/ plume extension computation
Satellite images	2016–2019	1 image/5 days	plume tracking/ plume extension computation
ISPRA images	2016–2019	13 images/day (5 AM–5 PM)	qualitative inspection of the plume southward alongshore extension
SGS video	2016–2019	13 videos/day* (10-minute duration)	PTV analysis, computation of the river surface velocity

* videos with visible floating material were chosen

$$u_{plume,y} = u_{waves,y} + u_{wind,y} \tag{4.3}$$

Table 4.2 reports an overview of the video-monitoring products used for this study.

4.2 Numerical modeling

Hydro-morphodynamic simulations were performed using the Delft3D software suite [44], a widely used 3D modeling suite to investigate hydrodynamics, sediment transport and morphology for fluvial, estuarine and coastal environments (see Section 3.2.1 for details). A two-dimensional, depth-averaged, model was implemented coupling the FLOW [14] and WAVE [15] modules, apart from the simulations forced only with the river discharge, for which the FLOW module was run alone. We run 2D simulations because the focus of the work was on the planar extension of the plume toward the offshore and alongshore and not on the vertical structure of the plume. Thus, even if aware of the importance of the water column stratification in the process of plume evolution, this aspect was not addressed here.

The following sections describe the model set up and simulations (4.2.1) and report some model calibration results relative to the suspended sediment concentration (4.2.2).

4.2.1 Simulations set up

Three regular grids, made by rectangular elements aligned with the coastline and the river axis, were created (Figure 4.5a). They were similar to those used for the study of the MR mouth bar (see Section 3.2.2), but extended more towards the south to observe the alongshore plume evolution. As standard for Delft3D, WAVE computations were run nesting a fine grid (*grid 3*) into a larger one (*grid 1*, whereas FLOW computations were performed using the domain decomposition approach (*grid 2* and *grid 3*). *grid 1* covered the coastal area in front of the Senigallia Harbour, it had a spatial resolution of around 30 m and extended about 7.8 km in the alongshore direction and 2.5 km in the offshore direction. *grid 2* was created from *grid 1* by cutting some cells at the offshore and lateral boundaries, while *grid 3* covered the final stretch of the MR and extended southwards reaching the beach in front of the ISPRA video system. It had

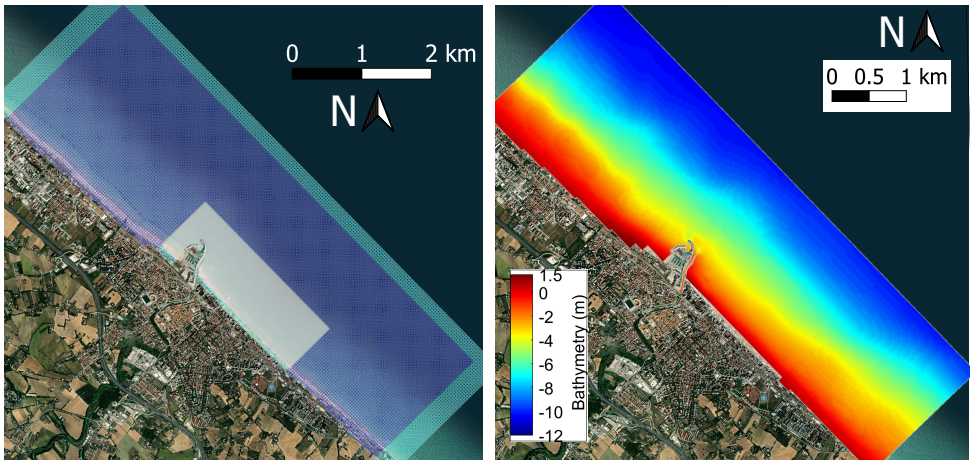

(a) (b)

Figure 4.5: Grids (a) and (b) bathymetry for the MR plume numerical simulations: *grid 1* in cyan, *grid 2* in blue, and *grid 3* in gray.

grid cell size variable from around 8 m in the offshore region to around 3 m along the river and it extended for about 2.5 km in the alongshore direction and 0.8 km in the offshore direction. The reference system used for the simulations was Monte Mario / Italy Zone 2.

The bathymetry was created by interpolating at the grid nodes the depth values coming from both the EMODnet bathymetry, available online, and a multibeam bathymetric survey of 1 m resolution carried out by the municipality of Senigallia in 2018. The survey extended 1 km offshore from the coastline, up to around 6 m depth, and 2.5 km in the alongshore direction, being the MRE at the centre of the survey (Figure 4.5b).

The bed stratigraphy was modeled using one mixed layer composed of a space-variable mix of gravel, fine sand and cohesive sediment. Based on in situ samplings [16], the upper stretch of the MR was characterized with 100% cohesive sediments, then, the presence of silt and clay decreased seaward until reaching 100% of sand in the sea area. Moreover, along the last stretch of the river, in correspondence of the inner bar location, a small percentage of gravel was added (2-3%). The sand and the gravel were characterized using a D_{50} of 0.18 mm and 6 mm, respectively, while for the cohesive sediments we set the critical shear stress for erosion equal to 0.3 N/m^2, the critical shear stress for deposition equal to 0.4 N/m^2 and the erosion parameter equal to 10^{-4} $kg/m^2/s$ (see Table 3.2) .

The boundary conditions generally depended on the aim of the simulation; real-life cases were forced with observed timeseries of the field conditions, whenever available, while test cases were run using "parametric" inputs. Just at the cross-shore edges of *grid 2*, the boundary condition remained the same for all the simulations, which is a Neumann-type condition of zero-water level gradient.

Two real-life simulations were run to compare the results with observations, the former reproducing a river discharge event occurred on 31 May 2019, the latter characterized by a sea storm happened on 12 March 2019 (Figure 4.6). The WAVE model was forced, at the seaward boundary of *grid 1*, with timeseries of wave parameters recorded by the Meda station. In the FLOW model, a total of four boundaries were defined. A total discharge boundary condition, computed through the rating curves of the Bettolelle hydrometer, was imposed at the upstream boundary of the river channel in *grid 3*. In the same section, a cohesive sediment concentration was added as defined in Section 4.2.2. The offshore boundary of *grid 2* was forced with a water level timeseries, using data recorded by the Senigallia tide gauge, while at the two cross-shore boundaries, zero-gradient water level (Neumann-type) boundary conditions were specified. Moreover, wind timeseries, provided by the Meda station, were used as input forcing, uniformly distributed over the domain. We chose not to implement

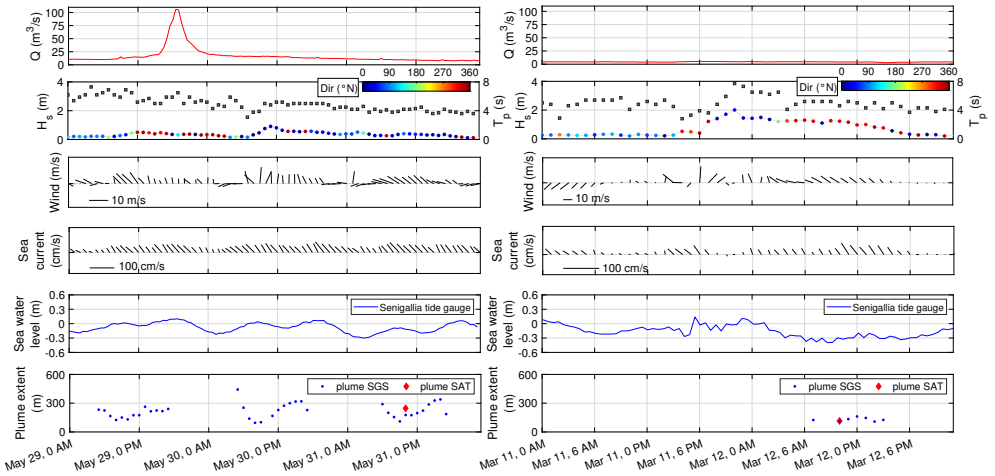

Figure 4.6: Timeseries of estuarine forcing observed during the plume events of 31 May 2019, generated by a river discharge (left panels), and 12 March 2019, generated by a sea storm (right panels): river discharge (top panel), wave height, period and direction (second panel), wind (third panel), sea current (fourth panel), tide (fifth panel). The bottom panels show the plume extent tracked form SGS images (blue dots) and Satellite (red diamond).

marine currents due to the Adriatic global circulation (e.g. Western Adriatic Currents) because the available data, acquired about 1 nautical mile offshore from the MRE and displaying a decreasing intensity toward the shoreline, would represent a very minor agent for the plume evolution. The primary role of the wind rather than the coastal circulation in affecting small plume evolution is also documented in the literature [61, 64]. Finally, we added a background concentration for the Northern Adriatic Sea environment equal to 0.05 kg/m^3 [6, 25] .

Field observations and real-life simulations were the outcome of a combination of several mechanisms acting synergically and affecting the plume evolution. To isolate the action of a specific forcing, test case-simulations were run using artificially-built conditions that reproduced the shape of typical flood hydrographs and storms. Since one of the aims of such simulations was to verify that both river discharge and waves can suspend sediments inside the river mouth, no input concentration was added. Thus, only the local plume generation mechanisms are accounted for. Three simulations forced only by river discharge timeseries, characterized by discharge peaks of 10 (R10), 50 (R50) and 100 m^3/s (R100) were performed using only the FLOW module. At the offshore boundary a zero-water level condition was imposed to neglect the effect of the tide. Then, the R50 case was associated with a uniformly distributed and constant wind coming from different directions, to study the effect of the wind on the plume spreading. The wind intensity was fixed at 10 m/s, while the investigated wind directions were 30, 135, 210 and 315°N, to observe the effect of winds directed toward the coast, NW, the offshore and SE, respectively (R50-wind30, R50-wind135, R50-wind210, R50-wind315). Further, two simulations were run to inspect the role of high and low tide coupled with the river discharge. This was done by creating a sinusoidal timeseries for the tide and by making the peak of the river discharge timeseries (R50) simultaneous once with the high tide (R50H) and once with the low tide (R50L). Finally, waves coming from NNE and E, typically impacting on the Senigallia coast (Figure 2.3a), were simulated, with peak wave height equal to either 2 m or 5 m (W2N, W5N, W2E, W5E). The wind was combined also with the strongest storms, imposing a wind direction in agreement with that of the waves (W5N-wind 20, W5E-wind90).

Table 4.3 reports an overview of all the parametric simulations performed.

4.2.2 Calibration of the model

The calibration of the model in terms of suspended sediment concentration was performed using some turbidity measurements acquired in the MRE during the

Table 4.3: Overview of the test case-simulations run for the plume analysis. Values reported are: the river discharge peak; the wave significant height, peak period and mean direction at the storm peak; the wind intensity and direction; the tide simultaneous with the river discharge/storm peak.

Simulation ID	**River discharge**	**Waves**	**Wind**	**Tide**
–	m^3/s	m, s, °N	m/s, °N	m
R10	10	–	–	–
R50	50	–	–	–
R100	100	–	–	–
R50-wind30	50	–	10, 30	–
R50-wind135	50	–	10, 135	–
R50-wind210	50	–	10, 210	–
R50-wind315	50	–	10, 315	–
R50H	50	–	–	0.3
R50L	50	–	–	−0.3
W2N	0	2, 8.1, 20	–	–
W5N	0	5, 8.4, 20	–	–
W5N-wind20	0	2, 8.4, 20	10, 20	–
W2E	0	2, 9.1, 90	–	–
W5E	0	5, 10.1, 90	–	–
W5E-wind90	0	2, 10.1, 90	10, 90	–

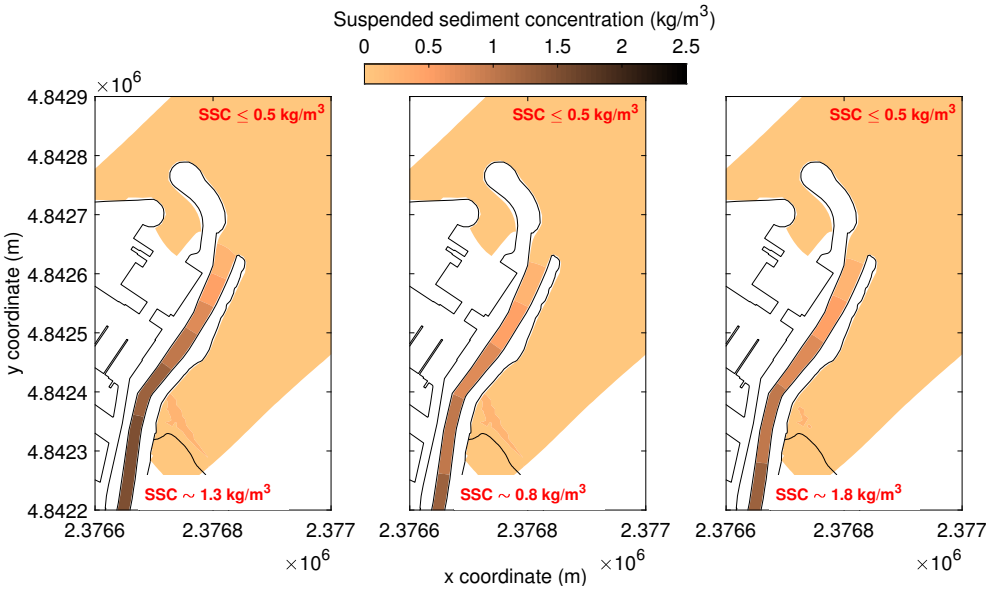

Figure 4.7: Calibration result: modeled suspended sediment concentration on 26, 27 and 29 January 2014. The SSC values reported in red refer to the measurements acquired during the EsCoSed field experiment.

EsCoSed experiment, carried out in 2014 [8]. Such procedure was needed to understand the amount of suspended matter transported by the river. The plume is in fact the result of both sediment transported by the river from the upstream part of the basin to the mouth and sediment suspended locally in the final stretch of the river by the river current and the waves. For that reason, to simulate real-life cases, an input concentration of the cohesive sediment fraction was imposed at the river section of *grid3*. To know the concentration values to assign, different simulations were run, comparing the results with the available measures, until reaching the best fit.

Such measurements consisted in vertical profiles of turbidity recorded by hand-deploying a Hach Quanta Hydrolab® at regular intervals in the river and the estuary. The depth-averaged turbidity measures were converted to suspended solid concentration (SSC), using a conversion factor of 1 NTU = 10 mg/l, to compare with simulation results. Based on previous MR studies, high SSC are in the region of 2500 mg/l and this was deemed equivalent to the maximum turbidity measured during the experiment, 250 NTUs [74].

The concentration was related to the river discharge using a power rating curve of the type $c = \alpha Q^{\beta}$ [2, 13], where c is the suspended sediment concentration, Q is the river discharge, α and β are two calibration factors. Imposing β=1, which is a reasonable value for Mediterranean small rivers characterized by relevant differences among mean daily flows and the extreme instantaneous flows during floods, a value of α=$\frac{1}{3}$ was found to best fit the observed concentration values. Such values were also in agreement with some historical data for the sediment transport in the Marche Region provided by Aquater [47].

The results of the calibration are reported in Figure 4.7, where the three panels show the modeled suspended sediment concentration on 26 (left), 27 (middle) and 29 (right) January 2014. The comparison with the values found during the EsCoSed campaign was quite good for the seaward area, where the observed concentration was always minor or equal to 0.5 kg/m^3. In the most upriver part, the observed concentrations were about 1.3 kg/m^3, 0.8 kg/m^3 and 1.8 kg/m^3, respectively for 26, 27 and 29 January [74]. The model well described the first two days, while underestimated the concentration of the last day. On such date, a turbidity maximum developed in the upper part of the MR, but the model did not capture its evolution because the flocculation was not accounted for.

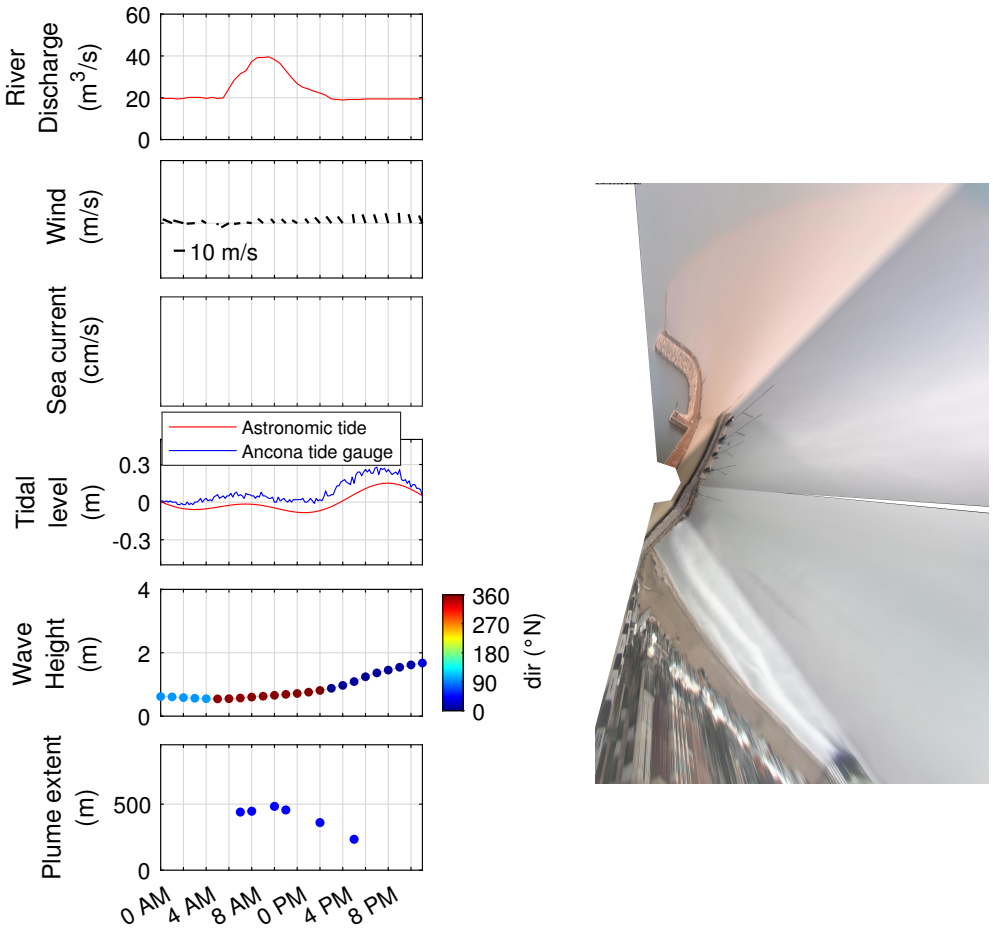

(a) (b)

Figure 4.8: Forcing conditions (a) and SGS image (b) of the plume event of 2 May 2016.

4.3 Observation results

The occurrence and extension of plumes derived from the images were correlated with the field data presented in Section 2.2 (Table 2.1) to identify the main generation and transport mechanisms. Three cases are presented in the following, which were classified on the basis of their generation mechanism, respectively the river discharge, NNE and E waves. Each type of plume has different characteristics, detectable from the images, so that one can conjecture the forcing conditions just looking at the images.

Figure 4.8 shows the plume event of 2 May 2016, caused by a river discharge: the SGS Timex image of 8 AM is reported on the right; the forcing conditions and plume extension are shown on the left. The plume appeared quite dense with sediment and reached a distance of around 500 m from the y-axis of the reference system in Figure 4.2. The river discharge was moderate (40 m^3/s), with a negligible concurrent tide. Waves started growing around 2 PM and, together with the raising of the flood tide, caused the reduction of the plume offshore extension down to 234 m. The wind blew mainly from NW, with a maximum speed of about 10 m/s, bending the plume toward SE. Current measures were not available for this event.

The correlation with the estuarine forcing revealed that also waves could generate plumes, even if lighter and smaller than those generated by a river discharge. Figure 4.9 shows an event occurred on 4 July 2016 under mild waves form the NNE (H_s <1) and a wind blowing from the same direction at a maximum speed of 5.3 m/s. The river forcing was negligible, and the sea current was weak with a mean daily intensity of 7.3 cm/s and an oscillatory direction changing from SE to NW. Moreover, the current was measured much further offshore than the area where the plume developed, thus it could not be directly related to the plume evolution. The plume was detectable

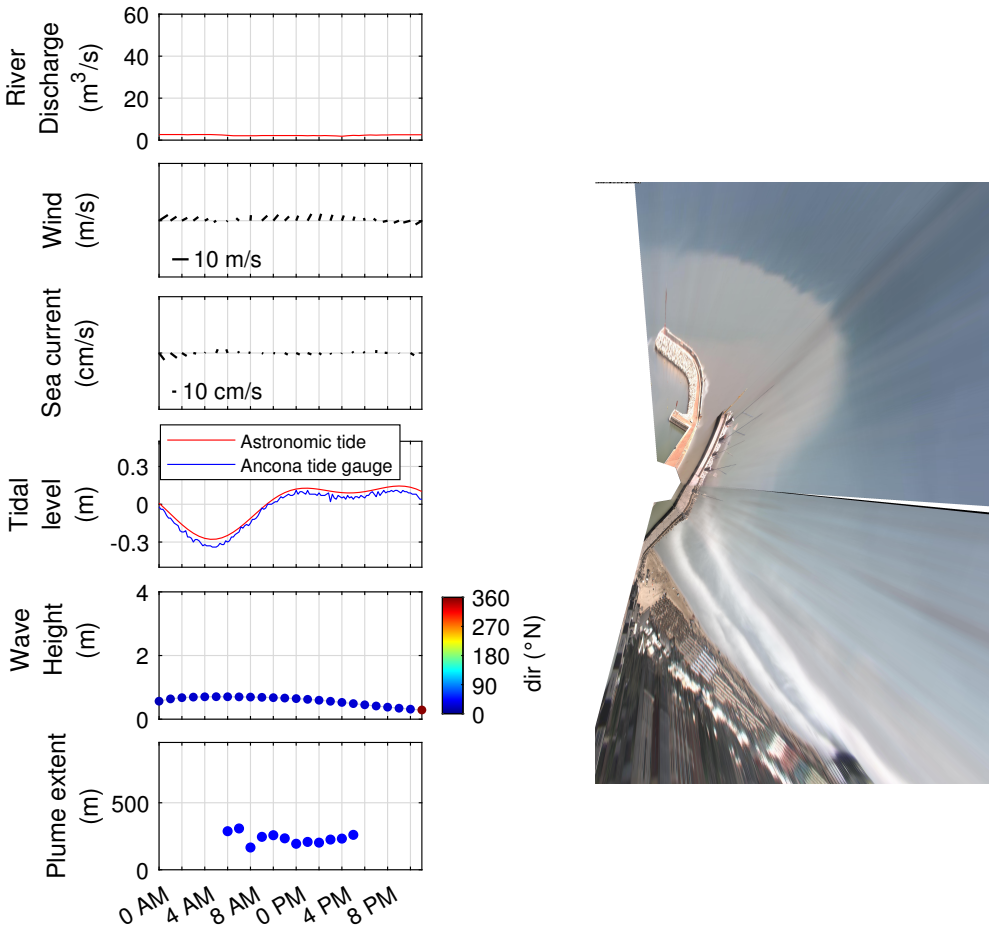

(a) (b)

Figure 4.9: Forcing conditions (a) and SGS image (b) of the plume event of 4 July 2016.

since 6 AM, when the tide started growing. The tidal excursion during the day was of about 40 cm but it did not affect much the plume extension. The SGS image of 10 AM shows a light plume, symmetrically diffused around the estuary and not largely extended toward the offshore (258 m). Moreover, breaking lines (lines of white pixels) are visible near the shore, confirming the presence of a weak wave storm. Based on such observations, NNE waves acted as i) a generation mechanism, by triggering some small sediment resuspension at the river mouth and ii) a transport mechanism, by keeping the plume confined around the estuary, preventing its offshore spreading.

Also waves from E-ESE seemed to be capable of resuspending sediments, as shown in Figure 4.10. This event occurred on 20 July 2016 under very mild waves. The pattern visible in the SGS image of 0 PM shows a plume of sediment diffused alongshore and just outside the river mouth. Based only on the observations, it was difficult to understand the origin of such sediments. Therefore, numerical simulations were run to clarify this and other aspects (see Section 4.5). The river discharge was negligible; both the wind and the sea current were directed toward the NW. Although the mean daily value of the sea current intensity was quite high (16.6 cm/s), it had a minimum of around 5 cm/s at 0 PM. On the contrary, at the same time, the wind reached a peak of 9.3 m/s. The plume extension varied from 191 m at 0 PM to 334 m at 5 PM without showing a clear correlation with the tide.

4.4 PTV results

To study the complex dynamics of the MRE, characterized by a combination of forces, PTV analyses were conducted on some video-recordings. Among all the available

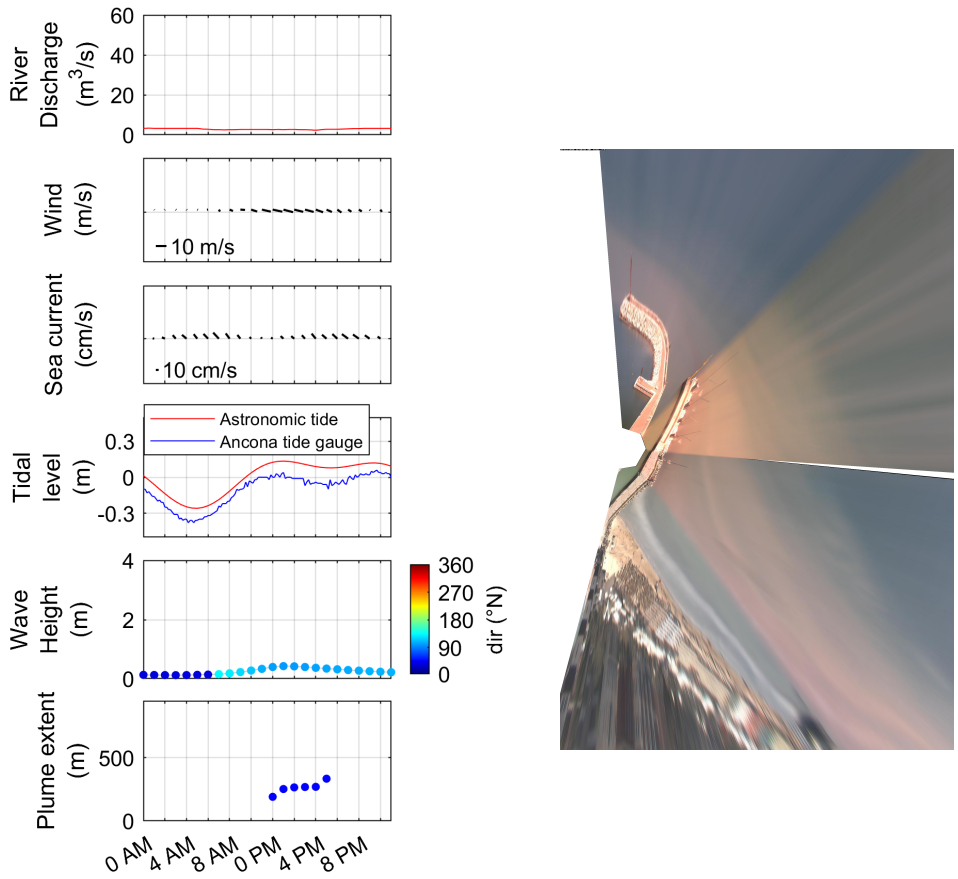

(a) (b)

Figure 4.10: Forcing conditions (a) and SGS image (b) of the plume event of 20 July 2016.

Table 4.4: List of the analyzed videos and forcing: the river discharge (Q), the wave parameters (H_s, T_p and wave dir.), the wind speed and direction (wind speed, wind dir.). The wave parameters (significant height, peak period and direction) were transferred to the river mouth by means of the Delft3D WAVE module. The last column reports the plume offshore extensions.

Video ID	**Date**	**Q**	**H_s**	**T_p**	**Wave dir**	**Wind speed**	**Wind dir**	**Extent**
		m^3/s	m	s	°N	m/s	°N	m^2
EV1	23 Mar 2016 11 AM	81.50	1.67	7.37	44.13	12.7	16.8	-
EV2	25 Apr 2016 10 AM	18.44	1.44	5.74	39.64	8.31	357	147
EV3	02 May 2016 11 AM	32.95	0.54	5.74	18.55	5.23	313	456
EV4	20 May 2016 02 PM	18.44	1.03	5.07	35.22	5.96	339	353
EV5	20 Jun 2016 04 PM	22.79	0.42	4.47	17.37	5.15	299	489
EV6	07 Mar 2017 12 PM	70.36	1.51	6.5	40.43	9.86	308	388
EV7	03 Feb 2018 08 AM	29.47	0.85	6.5	32.99	10	300	379
EV8	21 Mar 2018 09 AM	49.92	1.6	7.37	42.31	13	214	800
EV9	14 May 2019 09 AM	17.63	1.55	8.35	45.11	4.65	31.9	800

data, events where floating material detectable by the PTV was visible on the river surface were selected (Table 4.4). To correlate the velocity derived from the PTV analysis with the river discharge (Table 4.4), a weighted mean velocity was extrapolated for each video, as discussed in Section 4.1.2. Such value, hereinafter named "PTV velocity", was compared with a "manual velocity", which expressed the mean velocity of some particles that were manually tracked on each video. The "manual velocities" were used to check the accuracy of the PTV results, which were characterized by a relative error in the range 0.8-33%. Figure 4.11 shows the "PTV velocity" and the "manual velocity" with dots and asterisks, respectively, and their correlation with the river discharge. The surface velocities increased with the river discharge through a parabolic dependence ($v_{surface} = -0.00027Q^2 + 0.067Q - 0.037$). The R^2 coefficients are 0.77 and 0.87, respectively, for the "PTV velocity" and "manual velocity". The data scattering was due to the several forcing that acted in the estuarine area, e.g. wind, waves and tide, and that affected the surface velocity. Finally, the mean velocities of some drifters, launched within the EsCoSed project in 2014 (see [8]), were computed to compare their values with the PTV ones. The mean calculation was limited to the portion of the drifter trajectories that fell within the area framed by the videoimages. Such values (triangles in Figure 4.11) were in good agreement with the fitting curve, confirming the reliability of the PTV analyses also for low velocities, which are characterized by the largest relative errors. However, the action of the river was not the only force to affect the plume evolution. At a river mouth, the interplay of multiple factors determined the velocity of the flow and the consequent extension of the plume. Therefore, a further analysis was performed to compute the plume surface velocity, u_{plume}, accounting not only for the action of the river, but also for the wave and wind forcing (Table 4.4). The computations are explained in

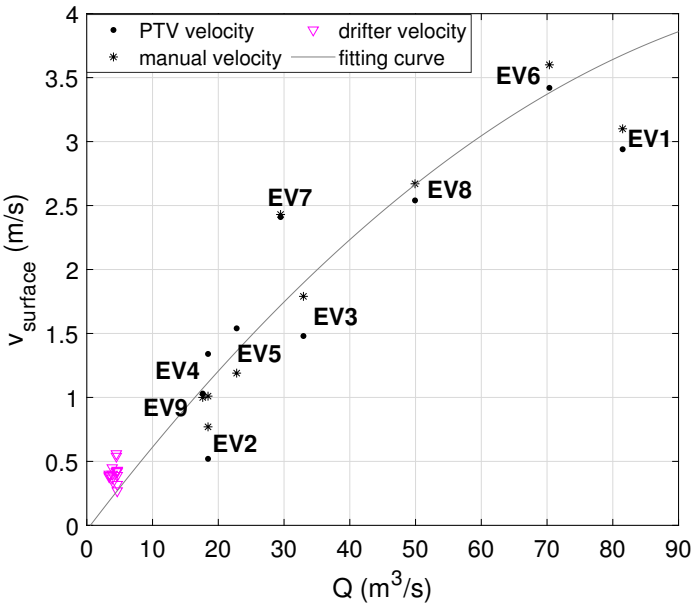

Figure 4.11: Correlation between particle velocity (v) and river discharge (Q). Dots and asterisks identify the PTV velocity and the manual velocity, respectively; the triangles represent the drifter velocity. The dotted line is the fitting curve for the PTV velocity data.

Section 4.1.3 and provided the results shown in Figure 4.12. Events EV1 and EV9 were discarded because either it was not possible to track the plume front due to poor image quality or the video was not in phase with the discharge peak, this impeding association of the plume velocity and extension (the latter influenced by the previous river discharge). Figure 4.12a shows the contributions giving the component of the plume surface velocity in the alongriver direction ($u_{plume,x}$). They are positive or negative if directed from the river toward the sea or viceversa. For the seven analyzed events, the main forcing was u_{river}, which was on average about an order of magnitude larger than $u_{waves,x}$ and two orders of magnitude larger than $u_{wind,x}$. Waves always opposed the river action, this suppressing the offshore propagation of the plume, while the wind could either contrast or enhance the river action depending on its direction. For the analyzed events, the wind contributed to the river action only for EV8. The contributions affecting the component of the plume surface velocity in the alongshore direction ($u_{plume,y}$) are illustrated in Figure 4.12b, positive/negative if directed toward SE/NW. The major forcing was $u_{wind,y}$, which was on average an order of magnitude larger than $u_{waves,y}$. The alongshore component of the waves is usually mild because refraction makes the wave fronts almost parallel to the coast. In fact, $u_{waves,x}$ was on average 7 times larger than $u_{waves,y}$. The ratio between the alongshore and cross-shore components of the wind is more variable because it depends on the wind direction. The sum of all contributions provided the components of the plume surface velocity, shown in Figure 4.12c. $u_{plume,x}$ was generally larger than $u_{plume,y}$, which was directed mainly toward SE. The extension of the plume is determined by the combination of the two velocity components, meaning that it depends on both the magnitude and direction of the plume velocity. Therefore, the plume extension was correlated with the absolute value of the ratio between $u_{plume,x}$ and $u_{plume,y}$, which represents the angle of the resulting velocity vector with the x-axis (Figure 4.4). The correlation coefficient between the two variables represented in Figure 4.12d was 0.87, meaning that they were strongly correlated. Thus, for fixed $u_{plume,y}$, the plume extension increased with $u_{plume,x}$, largely determined by the river velocity. On the other hand, for fixed $u_{plume,x}$, the plume extension decreased for increasing $u_{plume,y}$ because the alongshore current due to waves and wind deviated the plume toward either SE or NW, limiting its offshore extension (see Section 4.5.1). Moreover, being $u_{plume,x}$ mainly due to the wind forcing, the more the wind blew parallel to the coast the smallest was the plume extent, as also found in Section 4.5.1. The relation linking the two variables

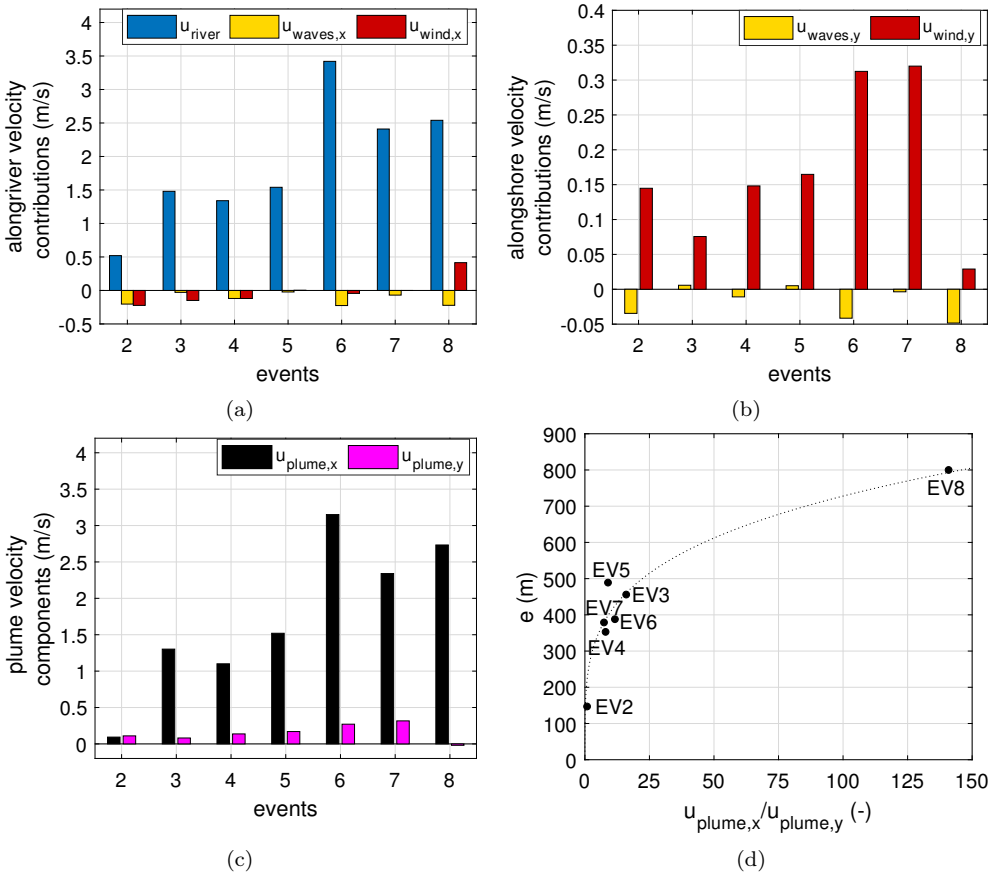

Figure 4.12: a) Contributions of river (blu), waves (yellow) and wind (red) to the alongriver plume velocity. b) Contribution of waves (yellow) and wind (red) to the alongshore plume velocity. c) Components of the plume surface velocity in the alongriver (black) and alongshore (magenta) directions. d) Correlation between the plume extension and the ratio between $u_{plume,x}$ and $u_{plume,y}$.

of Figure 4.12 was a power law with R^2=0.93:

$$e\left(\frac{u_{plume,x}}{u_{plume,y}}\right) = 230.2\left(\frac{u_{plume,x}}{u_{plume,y}}\right)^{1/4} \tag{4.4}$$

where e is the plume extension. Equation (4.4) can be used to estimate the plume offshore extension known the main forcing acting in the estuarine area, i.e. river discharge, waves and wind.

4.5 Simulation results

4.5.1 Parametric simulations

Two main mechanisms for the plume formation, i.e. mechanisms that directly put the riverbed sediments into suspension, were recognised in the first phase of the study (Section 4.3): the river discharge and the waves. The occurrence of a river discharge was always followed by a dense plume flowing out from the estuary mouth (Figure 4.8). Such plume appeared well marked in the images and it could be clearly tracked, since it caused a distinct change in the water colour from blue to brown. The high sediment concentration derived from: i) the material eroded and transported by the river from the upstream part of the basin to the mouth and ii) the local sediment suspended by the action of the river discharge and waves. However, since the aim of the parametric simulations was to inspect only the local generation of the plume at the river mouth, no input concentration was added at the river section of the model. Therefore, the following results show only the cohesive sediments suspended in the final stretch of the river mouth by different forcings. The non-cohesive (sand) contribution was neglected because it was an order of magnitude smaller than that of the cohesive fraction. The concentration was made dimensionless using the representative background concentration for the Northern Adriatic environment, c_{ref}=0.05 kg/m^3 [6, 25]. Therefore, the plume was identified as the area where the dimensionless concentration exceeded 1.

Simulations R10, R50 and R100, allowed us to find the discharge threshold above which sediment suspension began, identified as the minimum river discharge that led to exceeding the model critical shear stress for erosion (0.3 N/m^2). Such threshold is around 12 m^3/s that, considering a river section of about 32 m^2, corresponded to a depth-averaged velocity of 0.375 m/s. As already shown in Section 3.4.1, at the increase of the river discharge, the flow accelerates, exerting a larger shear stress over the riverbed. The more such stress exceeds the critical one for erosion, the larger is the amount of cohesive sediment resuspended. Therefore, as expected, the suspended sediment concentration increases with the river discharge, with maximum values occurring in the final stretch of the river, where the riverbed is characterized by a large deposit that causes the reduction of the section and the consequent increase of the velocity and of the bed shear stress. At such location, at peak time, the concentration is about 5 and 10 times the reference one, respectively for the 50 and 100 m^3/s peak river discharges, as shown in Figure 4.13b and Figure 4.13c, respectively. Furthermore, as a consequence of the increase of both the flow velocity and the sediment concentration, also the plume extension increases with the river discharge. Figure 4.13a shows the plume resulting from simulation R100 extending 24% more than that of R50.

In the simulations run only with river discharges, the plume obviously spreads symmetrically around the estuary, since no other action apart that of the river flow affects its evolution. Instead, when the wind is associated to the river discharge, the plume behaviour changes as illustrated in Figure 4.14a. South-easterly and north-westerly winds, blowing along the coast, deflect the plume toward NW and SE (red and green lines, respectively), as expected.This is also visible in the SGS images reported in Figure 4.14b and Figure 4.14c. When the wind blows toward the estuary, the plume is deviated toward SE (blue line), while the wind directed toward the sea deflects the plume toward NW (magenta line). This is because both the winds directed inside and outside the estuary have a component along the coastline, even if smaller than that of the south-easterly and north-westerly winds. The resulting plume offshore extensions

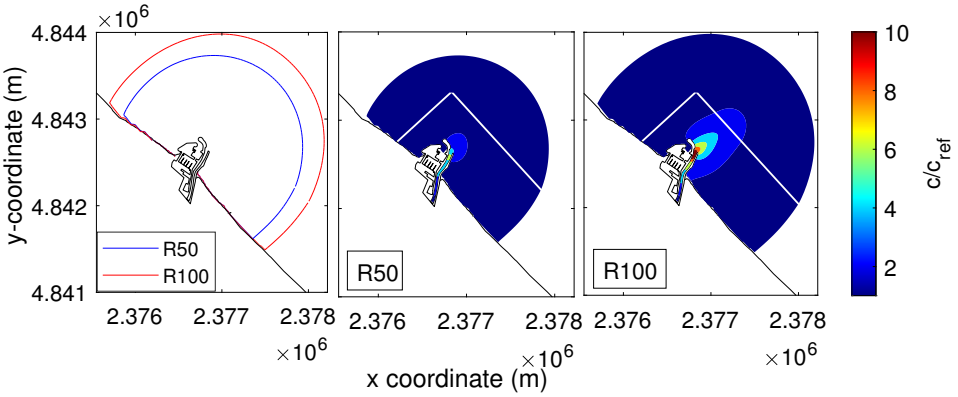

(a) (b) (c)

Figure 4.13: Plume fronts resulting from the simulations forced with the river discharge only (a). Suspended sediment concentration made dimensionless with the reference concentration for the R50 (b) and R100 (c) cases. The white lines represent the edge of *grid 3*.

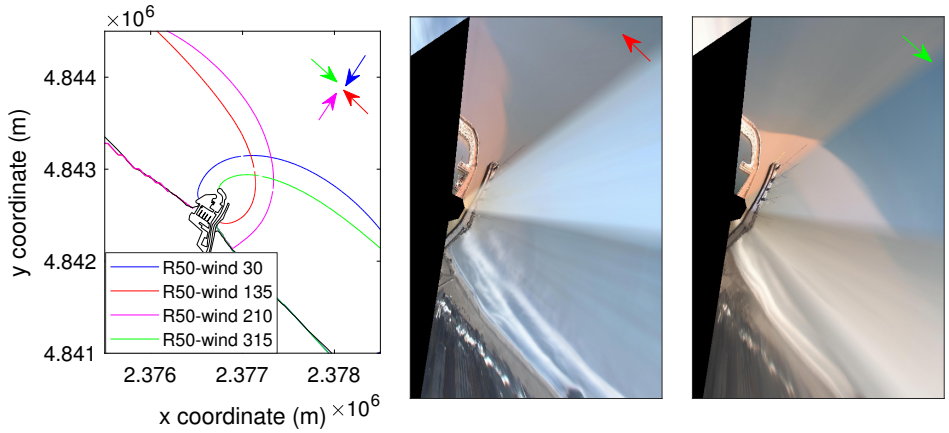

(a) (b) (c)

Figure 4.14: a) Plume fronts resulting from the simulations forced with a peak river discharge of 50 m^3/s and different wind directions, also represented with coloured arrows; b) SGS image of a plume transported toward NW by south-easterly winds; c) SGS image of a plume transported toward SE by north-westerly winds.

suggest that the higher is the alongshore component of the wind, the sharper is the plume deflection along the coast and, consequently, the smaller is its offshore extension. Plume events forced by waves coming from E and NNE are caused by the important stirring action of the riverbed sediments at the river mouth and appear less dense than RD ones. NNE wave-forced plumes spread around the river mouth, frequently assuming an arched shape immediately after exiting the river mouth (Figure 4.9), while E wave-forced plume deviate toward NW (Figure 4.10).

The comparison between Figure 3.12a and Figure 3.17 highlights that, even the most severe storms trigger a bed shear stress about a half of that by the simulation with a 50 m^3/s peak river discharge (Figure 3.12a). Therefore, the concentration generated by the waves, shown in Figure 4.15, is smaller than the concentration resulting from the river discharge simulations, reaching a maximum of 4.3 times the reference concentration under the NNE waves (H_s=5 m). Figure 4.15 shows the concentration maps at the storms peak, revealing that, in general, NNE waves resuspend more sediment than E waves. This comes from the fact that waves from the NNE approach the coast almost perpendicularly to the MRE, easily entering the estuary and causing an increase of both flow and bed shear stress up to about 200 m upriver, while E waves enter the estuary to a smaller extent. Moreover, the intensity of the stress caused by NNE waves is higher than that forced by E waves (see Figures 3.15 and 3.17).

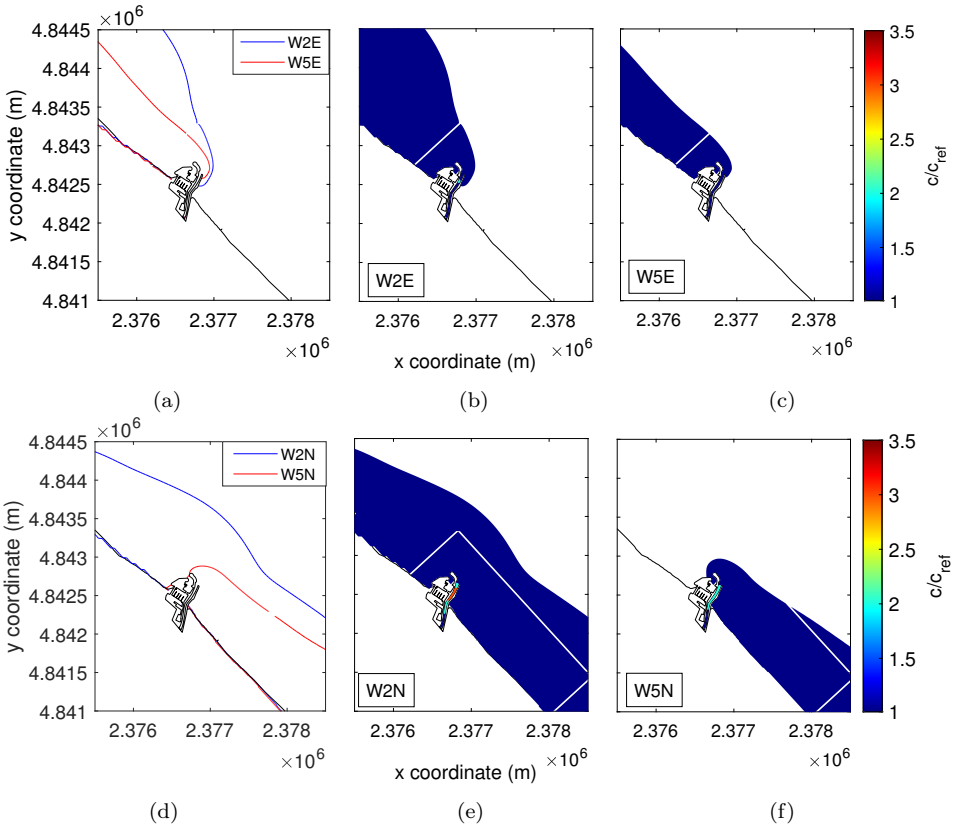

Figure 4.15: Plume fronts resulting from the simulations forced with E waves (a) and NNE waves (d). Suspended sediment concentration made dimensionless with the reference concentration for the W2E (b), W5E (c), W2N (e) and W5N (f) cases. The white lines represent the edge of *grid 3*.

Results also show that alongshore currents due to waves, presented in Section 3.4.1 (Figure 3.16), represent a transport mechanism for the plume. Blue and red lines in Figures 4.15a and 4.15d refer to $H_{s,max}$=2 m and $H_{s,max}$=5 m, respectively. They show that the plume extension both toward the offshore and alongshore is influenced by wave-generated currents. When such currents are mild, i.e. for $H_{s,max}$=2 m, the plume is more extended toward the offshore (blue lines). In particular, under small NNE waves, the plume remains symmetrically diffused around the estuary. Instead, intense currents, i.e. those caused by $H_{s,max}$=5 m, deviate the plume in the alongshore direction reducing its offshore extent (red lines).

To understand the role of the wind-wave interaction in affecting the plume dispersal, Figure 4.16 reports both results of simulations run with no wind (blue lines) and wind concordant with the wave directions (red lines). Solid and dashed lines identify instants before and after the storm peak (t=1 and t=2). Before the storm peak, when sea currents are not fully developed, the action of the wind causes the plume to strongly bend toward either NW or SE (red solid lines), reducing its offshore extension with respect to simulations with no wind (blue solid lines). Reaching the storm peak, the blue and red dashed lines get closer and closer, suggesting that the role of the wind in intensifying the effect of the wave-generated currents is no longer as effective.

The role of the tide in the plume generation and expansion was studied through two simulations where the 50 m^3/s discharge peak was taken to be simultaneous with high (H) and low (L) tide, respectively (Table 4.3). Figure 4.17 shows that when the river discharge peak is coincident with the high tide (red line), the plume extension is lower than the case with no tide. This is likely due to the reduction of the flow velocity and bed shear stress caused by the high tide (Figure 3.13).

Conversely, if the river discharge occurs concurrently with low tide (green line), the river flow velocity and bed shear stress are enhanced (Figure 3.13), this increasing

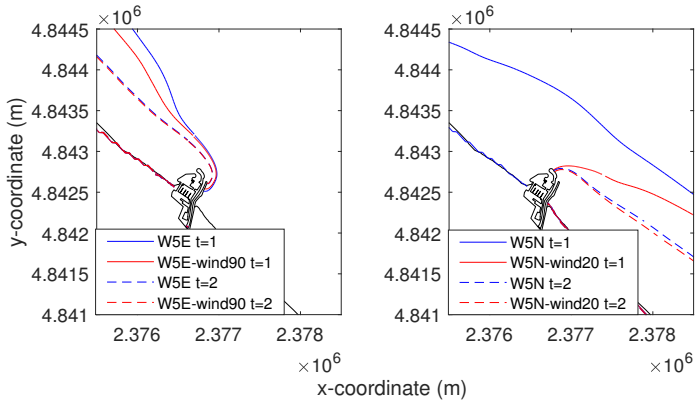

Figure 4.16: Plume fronts resulting from the simulations run with E waves (left) and NNE waves (right) characterized by wave height peak of 5 m, both alone (blue lines) and associated with a concordant wind (red lines). Solid and dashed lines refer to instants before and after the storm peak, respectively.

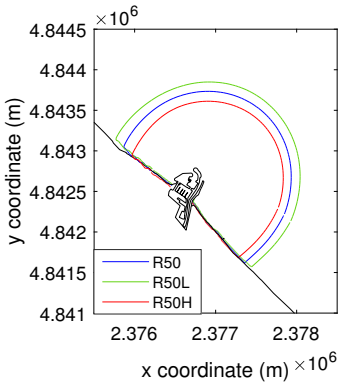

Figure 4.17: Plume fronts for simulations forced with a river discharge peak of 50 m^3/s and no tide (blue line), high tide (red line) or low tide (green line) concomitant with the river discharge peak.

the suspended concentration and the plume extension with respect to the simulation with no tide. In the simulated cases, the maximum tidal range for the MRE was used, that is 0.6 m. It produces a change in the plume extension (compared with the R50 case) of about $\pm$ 9.5% in the R50L case and R50H case, respectively.

4.5.2 Real-life simulations

We present results for an event generated by a river discharge and an event generated by waves coming from NNE, combining the observed data and the numerical simulations. It is clearly difficult to associate real-life events purely to one single mechanism, as often they are the outcome of a combination of physical phenomena. The events described in this section are, therefore, those that were characterized by the prevalence of one generation mechanism over the others. Moreover, the selected two events were well visible in both SGS and satellite images, to track the plume front. The Delft3D numerical results were used to compare the modeled and observed plume shapes and to highlight the differences between the discharge- and the wave-forced plumes. Simulations were run using recorded timeseries (see Figure 4.6).

The plume event shown in Figure 4.18 occurred on 29-31 May 2019 and was generated by a river discharge that reached 106 m^3/s on 29 May 2019, at 6:30 PM. The wave climate was characterized by a maximum significant wave height of 0.91 m, comparable with the 90^{th} percentile of the observations, and variable direction, mainly N and NE. Figures 4.18a and 4.18b show the plume from the SGS Timex image and from the satellite image, both acquired on 31 May 2019, at 10:00 AM and 10:08 AM

respectively. Since the images were acquired two days after the discharge event, a large quantity of sediment had already been washed out from the estuary, as confirmed by the bright area extending parallel to the coast. However, a dense plume could be distinguished from the background, meaning that the effect of the river discharge was still important after two days. The images showed that the plume was directed toward SE, this meaning that the prevailing transport mechanism was the wind coming from N-NNW at a maximum speed of about 9 m/s. Such value corresponded to the 95^{th} percentile of the observations. The sea current, directed toward NW, did not affect the plume direction in this case. Figure 4.18c shows the map of the modeled suspended sediment concentration (dominated by the cohesive fraction, as illustrated in Section 4.5.1). The simulated plume deflected toward SE, as in the images, and the tracked fronts fell between 0.1 and 0.07 concentration isolines, which reached the nearshore region in front of the ISPRA video system.

The plume event shown in Figure 4.19 occurred on 11-13 March 2019 and was characterized by a low river discharge of about 2 m^3/s and by N-NNE waves reaching 2 m, comparable to the 99^{th} percentile of the observations, on 11 March 2019 at 10:00 PM. The SGS (Figure 4.19a) and satellite (Figure 4.19b) images showed a light plume and breaking waves, which caused sand resuspension in the surf zone that mixed with the plume. Figure 4.19c shows the modeled suspended sediment concentration. The high concentrations near the shoreline were caused by the resuspension of the sand due to the wave action, while near the river mouth the plume was mainly composed by cohesive sediment. The simulation confirmed a density of the plume smaller than that generated by the river discharge, the plume front falling in correspondence of the 0.059 concentration isoline, which is about a half of the value found for the discharge-forced plume, and quantifying the marked density difference between the two types of plumes. The offshore extent of this wave-generated plume was around 30 meters smaller than that caused by the river discharge, restrained near the coast by the action of the waves. The wind coming from NNW contributed to the spreading of the plume mostly toward SE, as shown by the isolines.

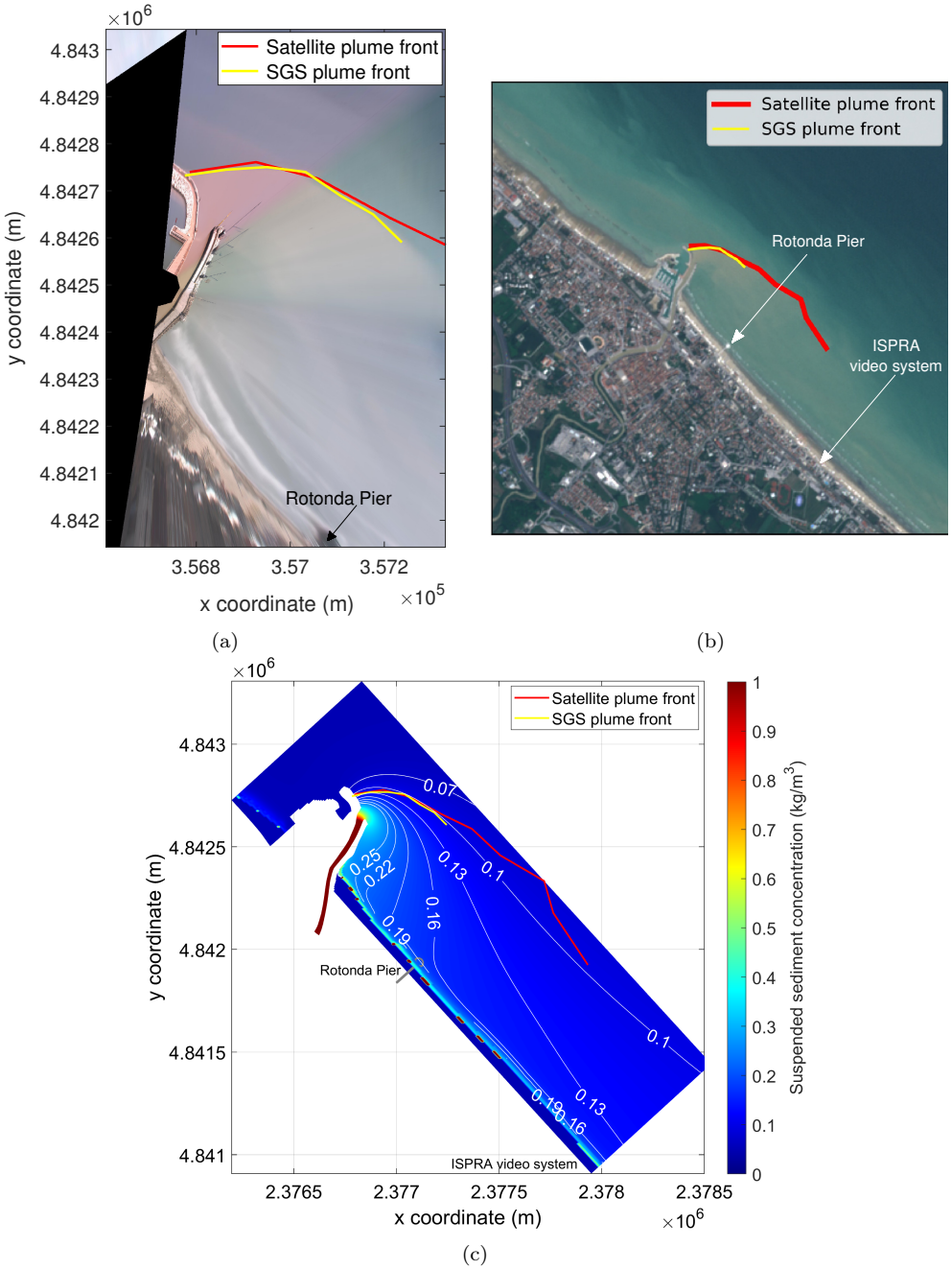

Figure 4.18: a) SGS Timex image of 31 May 2019 at 10:00 AM; b) Sentinel-2 image of 31 May 2019 at 10:08 AM (b); c) maps of the modeled suspended sediment concentration with some white contour lines. The fronts of the plume drawn on the SGS and satellite images are reported in yellow and red, respectively.

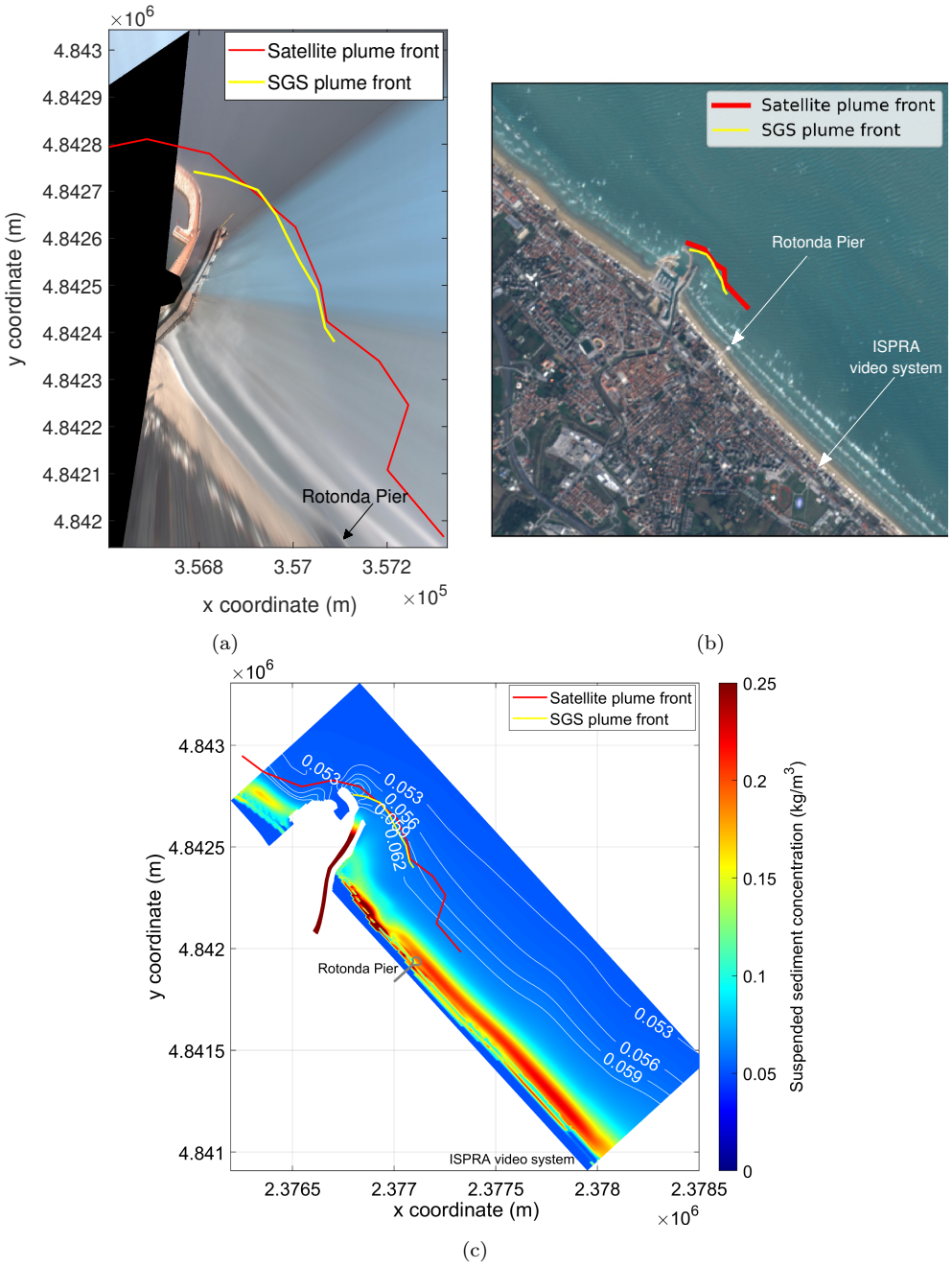

Figure 4.19: a) SGS Timex image of 12 March 2019 at 10:00 AM; b) Sentinel-2 image of 12 March 2019 at 10:08 AM (b); c) maps of the modeled suspended sediment concentration with some white contour lines. The fronts of the plume drawn on the SGS and satellite images are reported in yellow and red, respectively.

Chapter 5

Discussion

At river mouths, waves and outflowing riverine currents give rise to a very wide spectrum of interactions, which, in turn, has effects on the hydro-morphodynamics of coastal and estuarine environments. This study investigates some of such interactions occurring at the MRE and affecting its morphodynamic evolution. The MR is located in a micro-tidal environment since its relative tidal range RTR, defined as the ratio between the tidal range TR and the height of breaking waves H_b, is smaller than 3 [49]. Furthermore, the MR can be classified as a wave-dominated or river-dominated and wave-modified river mouth. The prevalence of the riverine or marine action can be assessed using two indices, the discharge index I_q [94] and the fluvial dominance ratio R [59]:

$$I_q = \frac{\textit{river liquid discharge per unit width of mouth}}{\textit{wave power per unit width of wave crest}} \tag{5.1}$$

$$R = \frac{\textit{river sand flux}}{\textit{max longshore sediment flux at river mouth}} \tag{5.2}$$

The former is a dimensional index (units of $m^3/W/s$) that increases of orders of magnitude from wave-dominated ($I_q \approx 10^{-5}$ $m^3/W/s$) to river-dominated ($I_q \approx 1$ $m^3/W/s$) systems, while the latter is a dimensionless index, also increasing from R<1 for wave-dominated to R>1 for river dominated systems.

The discharge index, computed using the results of the numerical simulations reproducing real-life events (Sections 3.4.3 and 4.5.2), confirms that the waves have a great impact on the MRE, with $I_q \approx 10^{-5}$ $m^3/W/s$ for the wave-driven plume event shown in Figure 4.19. However, the fluvial dominance ratio is always greater than 1. This apparent contradiction can be explained by looking at the meaning of each index: I_q takes into account the liquid river discharge, while R considers the solid river discharge. Therefore, even if the power of the river flow is smaller than that of waves, it transports much more sediment than that transported alongshore by waves. This agrees with the findings of Chapters 3 and 4, showing that the 1-year return period river discharge is more effective than the 10-years return period waves in both affecting the evolution of the MR mouth bar and resuspending plume sediments.

In the following, the main hydro-morphodynamic processes that affect the evolution of the MRE are described and discussed. The focus is on the effects produced at the river mouth by the action of the river discharge/waves alone or their combination. Attention is also given to other mechanisms, such as the tide and the wind, which modulate the processes triggered by the main forcing. First, the dynamics related to the MR inner mouth bar is analyzed, then the generation and transport mechanisms responsible for the formation and spreading of the MR plume are addressed.

5.1 MR mouth bar

In the absence of significant waves and tides, the hydrodynamics evolving outside of a river mouth usually consists of a bounded plane turbulent jet. Canestrelli et al. [9]

studied the hydrodynamic behaviour of a river jet debouching in a large quiescent water body using extensive numerical simulations. The authors mainly focused on the effects that bring to jet instability and on the consequences in the morphodynamics of river mouth bars and levees. Their results show that a jet can become unstable either by decreasing the stability number S_n or increasing the "river mouth" Reynolds number Re_B. The stability parameter embeds the strong dependence of jet stability on friction and aspect ratio and is defined as:

$$S_n = \frac{c_f}{2}\frac{B}{h} \tag{5.3}$$

where h is the water depth, B is the river width and c_f is the friction factor, defined as $c_f = \frac{2g}{C^2}$ being C the Chezy coefficient. The "river mouth" Reynolds number depends on the molecular viscosity ν, the width of the channel B, and the cross section-averaged velocity U_0 at the mouth:

$$Re_B = \frac{U_0 B}{\nu} \tag{5.4}$$

The MR is characterized by a stability number S_n=0.02 and, for river discharges in the range 10-100 m^3/s, the Reynolds number is of the order 10^1-10^2. Therefore, from the stability diagram for shallow jets ($B \geq h$) presented in [9], one can derive that the MR jet is stable. Once the river flow debouches into a quiescent sea, its centerline velocity reduces, the jet spreads and the sediments settle forming a mouth bar. The distance at which the bar forms increases with the jet momentum flux, the depth and the decrease in sediment size [17]. Moreover, the work of [9] reveals that frictional effects and jet stability play an important role when predicting mouth bar distance. A large jet stability causes a central bar to form closer to the river mouth and prevents the development of lateral levees, because the higher friction produces large dissipation, enhancing the spreading of the jet [58] and letting to sediment settling.

Previous studies on the MRE [8] confirm the presence of a central mouth bar at a distance of about two river widths from the river mouth [18]. In the past, the morphodynamics of the MRE was characterized by a typical cyclic behaviour with sediment deposition under weak river flow (summer conditions) and sediment erosion toward the sea under an intense river jet (winter conditions), as highlighted during field experiments performed in 2013 and 2014 [8]. However, over the last few years the deposition inside the river highly exceeded the erosion, leading to the emersion of a more stable deposit inside the channel since 2017. Figure 2.2b shows the growth of the riverbed from 2015 to 2020 due to the reduced amount of precipitation and river discharge occurred in the recent years. The large shoal in the final reach of the river usually emerges in a single location generating one single bar, but sometimes it can emerge in different areas generating complex morphological shapes, as happened in February 2019 (see Section 3.3.3). Moreover, the location where the bar typically forms derives also from a geometric effect. In fact, the bar is almost always adjacent to the west riverbank, that is the inner bank of a mild bend, where the flow decelerates allowing some sediment deposition. Finally, Brocchini et al. [8] observed a strong interaction of sea and river fluxes downstream of the main channel bend (final 290 m), this leading to sediment deposition at that location because of the convergence of downstream sediment transport and an upstream, nearbed advection of sediment induced by storm waves.

The opposite effect of river flow and waves on the MR sediment transport was also observed in the study of the MR mouth bar. Observations (Figure 3.8) showed that the bar migrated downriver when the estuary dynamics was dominated by the action of the river discharge. Even when the river discharge occurred simultaneously with a wave storm, the river action prevailed over the sea forcing, causing a downstream displacement of the bar. However, waves promoted a flow deceleration [18], thus reducing the migration. Furthermore, the more the bar was located upriver, the more intensively it is affected by the river flow action, while being sheltered from the action of the waves. This is also detectable in the real-life simulation (Section 3.4.3), characterized by almost concomitant river discharge and sea storm. The water river jet eroded the most upriver bar crest (upper panel of Figure 3.20) while an

accretion has been observed in the seaward area (lower panel or Figure 3.20), likely also impacted by the simultaneous wave action. Results confirmed that the effect of the river forcing was maximum on the portion of the bar located most upriver and almost null on the most downriver crest. Moreover, the simultaneous action of the waves did not significantly reduce the effect of the river discharge on the most upriver bar crest because it was located about 110 m upstream from the river mouth. For that case, the erosion of the bar crest was similar to that of the parametric simulation with Q=100 m^3/s, although the discharge was lower. This suggests that the waves did not greatly oppose the action of the river. The seaward sediment transport and consequent downriver migration of the bar always and only correlated with river discharge peaks, the upriver flow acceleration mobilizing the sediments and leading to erosion of the bar top and upstream face, the lee-side flow deceleration leading to sediment deposition [17].

The parametric simulations (Section 3.4.2), forced using two different river discharges of 50 m^3/s and 100 m^3/s, smaller in size than the 1-year return period discharge, show that the whole riverbed is eroded, with maximum erosion occurring at the most upriver bar crest and sediment accumulation taking place just downstream of such crest (upper panel of Figure 3.18), at a distance of around four river widths. This suggests the occurrence of downriver sediment transport due to the river forcing. These simulations also demonstrate that the amount of erosion and consequent deposition is directly proportional to the river discharge, although in a nonlinear fashion. Furthermore, they confirm that the effect of the river flow is more effective for the bar crest located more upriver, while it is negligible or smaller for the seaward portion of the bar.

When the river action was weak, the estuary dynamics was dominated by the sea action. A slow upriver migration of the bar occurred under a mild wave climate and negligible river discharges, as observed in Figure 3.9. While pushing sediment upriver, the waves modify the configuration of the bar [53] and give rise to complex morphodynamic shapes, as also observed from the images. In addition, storm waves, typically associated with storm surges, thus increasing sea and river water levels, triggered quick upriver migrations of the bar as observed during events W1-W4 (Figure 3.9. Such displacements were all smaller than one river width. As shown in Figures 3.14 and 3.15, the most frequent waves hitting the coast of Senigallia can enter the estuary, as also observed during an experiment in 2014 [8]. NNE waves, generated by the short-fetched northeasterly Bora winds blowing along the short axis of the Adriatic, represent short, steep swells propagating almost perpendicular to the shoreline, and directly into the MRE. Such swells generate intense breaking before and at the river mouth, suspending sediment and enhancing sediment transport. South-easterly winds instead blow along the Adriatic major axis, thus characterized by a longer fetch and producing long, narrow-spectrum, but comparatively weaker, less-steep swells that approach the coast with a wide incidence angle. ESE waves are then characterized by a longer shallow-water run and less intense breaking.

During the propagation from offshore toward the coast, waves undergo a number of transformations. When the waves start feeling the bottom variations, their height first decreases and subsequently increases, while their length first increases and then decreases. This process, known as wave shoaling, is followed by the wave steepening, and generally ends with the breaking of the wave, which can be enhanced by an opposing river current. Due to wave breaking, a decrease in the high-frequency energy content is observed on behalf of the lower wave frequencies, this leading to frequency downshift of the incoming waves. Recent studies revealed that a river mouth acts as a low-pass filter by removing, through breaking, sea and swell waves and letting long waves pass [3, 7, 50, 83]. Melito et al. [50] performed an analysis of infragravity (IG) waves propagation inside the MRE. The authors showed that sea/swell (SS) waves were strongly dissipated before entering the river mouth, through the combined action of wave breaking due to reducing depths and opposing river currents, while IG waves propagated upstream. Moving into the channel, IG waves gained a more relevant role over swell and wind waves. In fact, as the storm grew offshore, the IG band experienced the largest increment in flux energy density into the river while SS energy

was unaltered. The contribution of IG waves to the wave height in the river closely followed the offshore significant wave height and reached values of 0.5 m, 0.4 m and 0.3 m respectively 280 m, 400 m and 600 m from the river mouth. Parametric simulations run with waves as unique forcing showed that the wave height inside the channel reaches 0.5 m and 0.2 m, respectively for NNE and E waves, 150 m from the mouth (Figure 3.14). Waves are responsible for the upriver bar migration and accumulation of sediment offshore of the river mouth, as demonstrated by the parametric simulations (middle and bottom panels of Figure 3.18) and also by the real-life case (bottom panel of Figure 3.20). The highest waves, comparable to the 10-years return period waves, produce an upriver displacement of the most seaward bar crest of 0.78 river width, thus smaller than both the observed and simulated downriver migrations due to moderate river discharges (smaller than the 1-year return period discharge). This confirms the dominance of the river forcing over the waves on the bar evolution. The most upriver bar crest is moved slightly upriver by the highest NNE waves (H_s=5 m), while only a small accretion is observed as due to the 2 m-NNE waves and 5 m-E waves. Therefore, the north-easterly waves, approaching the estuary almost perpendicularly, can easily enter the estuary, being able to modify the upriver portion of the deposit more than easterly waves.

Based on the observation and simulation results, the main factors that govern the dynamics of the MR mouth bar are regarded to be the river discharge, the wave forcing, and their interaction, with the tidal forcing playing a secondary role, since the study area is characterized by small tidal variation. However, the tide was shown to represent a non-negligible factor even in micro- and meso-tidal environments. Ruiz-Reina and López-Ruiz [80] studied the hydrodynamic and morphodynamic effect of the time lag between the tide and the maximum river discharge, showing that it plays a very important role on the velocities, shear stresses, sediment transport and river mouth bar development. The maximum velocities depend mainly on the river discharge, increasing as the river discharge rises. The tidal lag plays a secondary role on these maximum values, which are higher when the peak discharge coincides with the low tide. This is also detectable in Figure 3.13, showing the increase/decrease of the maximum velocity just inside the river mouth, respectively when the river discharge peak is simultaneous with low/high tide. The bed shear stress and consequent sediment transport, directly related to the velocity, share the same behaviour, leading to a limited/maximum bar extension when the peak river discharge coincides with the tidal flood/ebb [80]. The results shown in the top panel of Figure 3.19 are concordant with those of [80], since they show the larger/lower bar modification under low/high tide. Finally, Ruiz-Reina and López-Ruiz [80] also found that the alongriver velocities peak at the location of the bar, followed by a sudden decrease as the flow exits the river mouth, this being in agreement with the result shown in Figure 3.12b. The tide has also a fundamental role in controlling the upriver propagation of IG waves in the MR micro-tidal estuary, similarly to what observed in macro-tidal environments [3]. In detail, propagation velocities are enhanced during flood tide and high tide, mainly due to an increase of water levels into the estuary [50]. However, the riverbed evolution does not show significant variations between the simulations forced only with the waves and those forced with waves and tide (middle and bottom panels of Figure 3.19). Moreover, despite the small tidal range at the MR (less than 0.6 m), tidal oscillations were observed up to 1.5 km from the river mouth [50]. The effect of such oscillations affects the emerged portion of the bar, reducing or increasing it as the tide rises or falls, respectively.

5.2 MR plume

The MR plume is representative of those small-scale river plumes that supply a large amount of sediment to sea. The dynamics and structure of plumes of small rivers differ considerably from those of large rivers, due to differences in the physical scales of the processes near the river mouth [24] and relatively short duration of floods occurring in small, torrential rivers compared to large river systems. The fate of sediments in large river systems, characterized by freshet periods that extend over months, depends on

forcing conditions over seasonal time scales. Small and intermediate-size rivers with steep drainage basins exhibit markedly different behavior: flooding events can evolve in extremely short time, occurring almost on the same time scale as the meteorological events that supply the precipitation. Thus, as shown by the analysis presented herein, the dynamics of a small-scale river plume are clearly influenced by the main local driving mechanisms, namely the freshwater discharge rate and the prevailing wind.

The first part of the discussion is dedicated to the local generation mechanisms, i.e. processes capable of suspending sediments at the river mouth. From the image analysis and the following correlation with the estuarine forcing (Section 4.3), two generation mechanisms were identified, the river discharge and the waves. While the former is well known and its relationship with the plume extension has been widely addressed in the literature, less attention has been given to the latter.

The hydrodynamic results of the parametric simulations show, as expected, that the current speed increases with the river discharge (Figure 3.12a). The maximum flow velocities occur in the final river stretch (Figure 3.12b) due to the gradual reduction of water depth caused by the presence of the submerged deposit. Then, the jet spreads outside of the river mouth, with a drastic reduction of the speed due to the sudden section widening and depth increase. Such behaviour is typical of a bounded jet flowing into a calm water body, as also observed by [51, 60]. As described in Section 3.4.1 and confirmed by Figure 4.13, as a consequence of the increased velocity in the final reach of the MR, the sediment resuspension is maximum at such location. Since the quantity of suspended cohesive sediments depends on the entity of the bed shear stress, in turn directly proportional to the river velocity, then the concentration increases with the river discharge. Doubling the discharge almost leads to the doubling of the maximum concentration, which reaches around 10 times the reference concentration under the 100 m^3/s-river discharge. When the river jet exits the mouth, its velocity reduces, and it expands in the sea [18] assuming a symmetrical shape (Figure 4.13). In fact, flowing into a quiescent water body, the plume is not subject to transport mechanisms that influence its spreading. In such a particular condition, the plume extension strictly depends on the river discharge, being their relationship characterized by a correlation coefficient $r \simeq 0.95$ and a determination coefficient $R^2 \simeq 0.91$. The direct proportionality between the river discharge and the plume extent is widely documented in the literature (a.o., [52, 61]), not only by modeled situations, but also by observations. As an example, a recent study by Lebedev et al. [42] showed the existence of a strong linear relationship ($R^2 = 0.99$) between the river runoff and the plume area for the Mzymta River, a small river debouching in the northeastern Black Sea. For the MR case, the results of the PTV analysis reveal that the plume offshore extent, other factors being equal, increases with the plume alongriver velocity (Figure 4.12d). Such speed is mainly determined by the river velocity (Figure 4.12a), which in turn is proportional to the river discharge, as shown in Figure 4.11.

As already discussed in Section 5.1, the tide can alter the velocities in the channel (Figure 3.13) and, in turn, the consequent shear stresses and sediment transport [80]. Figure 4.17 shows that the effect of the tide is that of increasing/reducing the plume extension ($\sim 10\%$), respectively when the discharge peak occurs simultaneously with low/high tide.

The results of Section 4.4 also demonstrate that the current speed at the river mouth is influenced not only by the river discharge, but also by other forcing acting at the estuary. The coefficient of determination between the surface velocity derived from the PTV analysis and the river discharge is 0.77, meaning that not all the variability of the velocity v can be attributed to the variability of the river discharge Q (Figure 4.11). Waves and wind are taken as the two other main forces affecting the plume surface velocity. Waves always oppose the river flow (Figures 3.14 and 4.12a), slowing it down and promoting jet expansion with a consequent more intense deposition close to the river mouth [18, 77]. Moreover, Olabarrieta et al. [60] found that waves push the river jet back to the coast, as also observed in the SGS images of plume events occurring under NNE waves. Such waves approach the coast almost perpendicularly and keep the plume restricted around the estuary preventing its offshore expansion (Figure 4.9). The study of the MR plume through the video-monitoring products

Table 5.1: Conceptual model by Kastner et al. [38].

Mode	**Condition**
Wave dominance	$L_{SZ} > L_{NF}$ and $L_{SZ} > L_C$
River dominance	$L_{NF} > L_{SZ}$
Bathymetric dominance	$L_C > L_{SZ}$

also reveals that waves, apart from acting in combination with the river discharge, represent themselves a generation mechanism for the plume. Such observation results are confirmed by numerical simulations showing that storm waves are capable of resuspending sediments at the river mouth (Figure 4.15), even if the concentrations are smaller than those triggered by river discharge events and reach maximum values of 4.3 times the reference concentration under the most severe NNE storm (H_s=5 m). Such result is consistent with what can be observed from the SGS images, that is the occurrence of more marked and dense plumes following a river discharge rather than a sea storm. Moreover, as already highlighted by the study of the MR mouth bar, the river action, even if comparable to the 1-year return period forcing, produces higher morphodynamic effects than the 10-years return period waves.

To determine the prevalence of the riverine/wave forcing in the fate of the MR plume, the conceptual model of Kastner et al. [38] can be applied, which is based on three length scales: the surf zone width, L_{SZ}; the near-field plume length, L_{NF}; and the cross-shore extent of the channel, L_C. The near-field is defined as the area over which the estuarine outflow is supercritical, where momentum effects dominate over buoyancy effects. The channel length is the cross-shore location where the channel formed by the seaward extension of the river channel into the nearshore bathymetry is no longer deeper than the surrounding bathymetry. It is either determined by sediment transport at a natural river mouth or set by dredging and/or the presence of jetties at an engineered river mouth. The relationships between these length scales determine three possible scenarios, reported in Table 5.1: i) when L_{SZ} is larger than both L_{NF} and L_C, the river plume is trapped in the surf zone by the wave forcing; ii) the plume exits the surf zone because its momentum overcomes the breaking wave forcing when $L_{NF} > L_{SZ}$; iii) if $L_C > L_{SZ}$, the plume reaches the inner shelf largely bypassing the wave forcing due to minimal wave breaking in the channel.

The surf zone width represents the cross-shore distance over which wave breaking occurs and was estimated as the corresponding cross-shore distance of d_b, the depth at breaking, computed following [38]:

$$d_b = \left(\frac{H_0 c_{g0}^{1/2}}{\gamma_b g^{1/4}} \right)^{4/5} \tag{5.5}$$

where H_0 is the offshore wave height, c_{g0} is the offshore group velocity, g is the gravitational acceleration and γ_b is the critical value of $\gamma = \frac{H_s}{h}$ for which no breaking occurs in the channel, with H_s the significant wave height and h the water depth.

The near-field plume length depends on the river mouth velocity u, the river discharge Q, the density difference between the river mouth and the ambient offshore water g' and the entrainment velocity w_e [30]:

$$L_{NF} = \frac{u^{3/2} Q^{1/4}}{g'^{1/2} w_e^{3/4}} \tag{5.6}$$

where $g' = \frac{g \Delta\rho}{\rho_0}$ and $w_e = \delta u$. $\Delta\rho$ represents the difference between the river mouth density ρ and the offshore water density ρ_0, while $\delta = 0.02(\frac{g' h_p}{u^2})^{-1/2}$, where h_p is the plume depth at the river mouth, here assumed equal to the water depth at such location.

The channel length, at an engineered river mouth, is set by the length of the jetties.

The model was applied to the real-life cases presented in Section 4.5.2. The river discharge (RD) case resulted to be bathymetry-dominated, since the length of the

channel (L_C = 300 m) was larger than both the width of the surf zone (L_{SZ} = 42 m) and the near-field plume length (L_{NF} = 70 m). In such conditions, wave breaking occurred inshore of the ends of the jetties and caused no opposition to the river momentum, thus the river water could escape from the surf zone (Figure 4.18). Conversely, the wave (W) case turned out to be wave-dominated, with L_{SZ} = 383 m larger than both L_C = 300 m and L_{NF} = 26 m. Under such conditions, the plume was trapped in the surf zone (Figure 4.19) because the wave-driven momentum, directly related to wave breaking, dominated over the river momentum. To confirm this statement, the dimensionless parameter S_w (wave stress ratio) was computed, following an approach similar to that by Zarzuelo et al. [96]. For the MR system, such parameter represented the ratio between the river and the wave actions and was defined by scaling the terms of the momentum equation related to such forces. The numerator was scaled as $\frac{U^2}{L}$, where U is the river depth averaged velocity and L is a length scale defined as the distance between the river section of the model and the river mouth. Melito et al. [50] showed that sea/swell waves are strongly dissipated before entering the river mouth and only IG waves do propagate upstream. The denominator was scaled as $\frac{F_s}{\rho_0 h}$, where F_s is the wave induced force per unit area. All quantities were evaluated at the river mouth using the numerical results at the peak of each event. The sign of the base 10 logarithm of S_w gives the greater importance of numerator or denominator. The RD case was characterized by a positive value, meaning that the river forcing prevailed over the waves, while a negative value was obtained for the W case, indicating wave prevalence. Moreover, given the high engineering of the MR, the role of the jetties strongly influenced the plume behaviour, as shown by a further analysis, performed by varying the wave parameters and keeping the river discharge fixed (Q = 2 m^3/s) and viceversa (with fixed H_s = 0.5 m and T = 5 s). Channel dominated conditions were found for all the RD cases tested and for the W cases characterized by $H_s \leq 1.6$ m. On the other hand, the W cases with $H_s \geq 2.4$ m were wave-dominated regardless of the wave period, while for H_s in the range 1.7 - 2.3 m, wave dominated conditions occurred only for some combinations of significant wave height and period, with larger periods being needed at the decrease of the wave height.

A very comprehensive, recent work by Anthony [1] provides a nice overview of the role of waves at river mouths. Waves remove fine sediments at the river mouth and flatten the delta by moving the sediment alongshore. Wave-induced currents generate longshore sediment transport, maximum for 45° wave attack. Such observations agree with the finding of this study, where waves are found to be also a transport mechanism for the plume. Figure 4.15 shows that waves move the suspended sediment along the coast, either toward NW or SE depending on the wave direction. The comparison between Figures 4.15b and 4.15e also demonstrates that the more the waves are oblique the more they are effective in deviating the plume alongshore. In the breaking zone, most of the momentum and energy of the short waves is transferred both to turbulent motion and to currents (Figures 3.15 and 3.16). Such currents are higher for E waves than for NNE waves, as shown in Figure 3.16, thus E waves cause the greater alongshore transport.

Wave-driven currents can be intensified by a concurrent wind (bottom panels of Figure 3.16), with a consequent reduction of the plume offshore extension (Figure 4.16. The influence of the wind is more effective when the waves, and therefore the wave-driven currents, are small (e.g. before reaching the storm peak, as shown in Figure 4.16). The relative role of wind and waves in defining the alongshore plume velocity was also investigated through the PTV analysis (Section 4.4), showing that, in real-life cases, the wind forcing is dominant with respect to the wave action (Figure 4.12b). A correlation of the alongshore wind speed with the alongshore surface currents and the plume velocity immediately offshore of the river mouths was documented by Warrick et al. [89], who found that the advection of plumes in the alongshore direction was dominated by local winds. The dominance of the wind forcing in determining the plume evolution is reported in various observational and modeling studies, for both large (e.g. [10, 21, 36, 91]) and small river systems (e.g. [11, 61, 73]). Ostrander et al. [64] found a strong correlation between drifters and wind direction in a river characterized

by outflows ranging between 50 and 100 m^3/s, similar to the MR, meaning that the surface water responded directly to the forcing of the wind, moving along its heading. Figure 4.14a shows that the direction toward which the plume flows is determined by the wind, as also confirmed by the SGS images (Figures 4.14b and 4.14c). Moreover, the larger is the alongshore component of the wind, the smaller is the plume offshore extension because the plume is strongly and rapidly transported along the coast and do not expand toward the offshore. A similar result is reported by Osadchiev and Sedakov [61], who studied the response of the Mzymta river plume to different forcing conditions. They showed that, for small rivers in micro-tidal environments, the near-field plume did not form a recirculating bulge adjacent to the river mouth, but directly transitioned to the wind-dominated, far-field plume. Moreover, they observed that the offshore extension of the plume was smaller under a wind blowing in the alongshore direction. Such results are also in agreement with the findings of the PTV analysis (Section 4.4), which highlight that the plume extension decreases with increasing alongshore velocity, mainly dominated by the wind force (Figure 4.12d).

Chapter 6

Conclusions

The present study addresses phenomena of importance for the estuarine dynamics of small-scale river systems, characterized by a torrential regime, located in micro-tidal environments. Example of such sites can be found along the Adriatic coast, among which the Misa River is a good representative, and all over the world (e.g.,[42, 52, 61]). Despite its small dimension, the MR expels large amounts of sediment to sea. The hydro-morphodynamics of the estuary is very complex since it is characterized by the interaction of multiple forcing. The analyses carried out in this work, focused on the evolution of the MR inner mouth bar and plume, aim at understanding the role of each force and of their combination on the river mouth dynamics.

River mouths constitute the transition between rivers and oceans, where tides and waves interact with river discharges transporting most of the sediment eroded on the continents to the oceans and forming deltas and depositional river mouth bars, resulting in one of the most dynamic environments on Earth [12]. These systems are usually densely populated hosting many human activities and complex ecosystems. Despite this critical role for society and life, many processes occurring at river mouths are still poorly understood, as for example the formation of mouth bars in front of fluvial distributaries. The present research investigated some mechanisms that govern the evolution of inner mouth bars because their understanding is fundamental for the optimum management of such depositional features. People living in river mouth areas today are increasingly exposed to many hazardous events, such as flooding, subsidence, and coastal erosion. The intensity and frequency of such events are increasing due to the effects of the climate change, to which the estuarine environments are highly exposed. In this scenario, the presence of an inner mouth bar represents a source of concern for people living near the river mouth and for the authorities responsible for the risk management of the area. In estuarine cities, like Senigallia, subject in the past to severe flooding that caused human losses, the major worry regards the obstruction of the river outflow by the sediment deposit with consequent increase of the flooding risk. The results of this work highlight that, even if waves have a great impact on the hydrodynamics of the MRE, the river forcing prevails in terms of sediment transport. The river discharge-induced sediment expulsion out of the river mouth dominates over the upriver transport by the waves. A significant erosive capacity of the river, which is maximum during flood events following extreme precipitations, was also detected through the SGS images under moderate river discharges comparable to or smaller than the 1-year return period discharge. Moreover, numerical simulations confirm that 1-year return period river discharges trigger downriver migrations larger than the upriver displacements caused by the 10-years return period waves. Since even small river discharges are able to transport sediments to sea, then the inner mouth bar does not impede the sediment outflow to sea. However, the disruption of the bar cyclic behaviour due to reduced rainfalls leads to the formation of very large deposits, which occupy the entire river section and obstacle the outflow during low-flow conditions. Therefore, the monitoring of the inner mouth bar evolution is useful to programme the maintenance operations of the channel in periods when the natural dredging of the riverbed cannot be done by the river itself. Optical imagery represents a valuable

tool for coastal monitoring since it offers the unique capability to collect high volumes of data at high temporal and spatial resolution with relatively low cost and over long periods. The integration of such technique with field data and numerical modeling provides a quite exhaustive set of information to support engineering projects and facilitate coastal management decisions.

The combination of multiple sources of data is the basis of the methodology used for this research and turned out to be effective also for the plume analysis. Despite the relatively small surface areas and volumes as compared to the saline ambient sea, river plumes govern land-ocean fluxes of buoyancy, heat, terrigenous sediments, nutrients and anthropogenic pollutants and, thus, significantly influence many physical, biological, and geochemical processes on the continental shelf. Therefore, the transport of cohesive sediments in coastal areas has significant impacts on both the economy (navigation, tourism, aquiculture, etc.) and the quality of the marine environment [39]. Consequently, the knowledge of the key factors governing the plume behaviour can provide relevant information for coastal resource management, environmental protection and for planning sustainable development of coastal areas. The MR, like many other rivers with a steep drainage basin, expels large quantity of sediment to sea during short flood events. The outcomes of the analysis showed that the river discharge represents the main plume generation mechanism and the major contribution to the alongriver plume velocity. Plumes generated by river discharges are characterized by higher concentrations and larger offshore extensions. Waves turned out to be capable of triggering some sediment resuspension at the river mouth and, together with the wind, affect the plume alongshore spreading. The transport mechanisms determine the plume alongshore velocity, whose increase causes the reduction of the plume offshore extent and pushes the plume to farther distances along the coast. Images reveal that sediments are mainly transported toward the south-east, reaching distances up to some kilometers from the river mouth, as also demonstrated by numerical simulations. This means that the sediments originating from the river basin likely contribute to some nourishment of the beaches to the south of the MRE. Also, this gives information about the paths followed by particles other than sediments, as nutrients and pollutants.

The hydro-morphodynamics at micro-tidal river mouths could be further explored by implementing a three-dimensional model to investigate physical mechanisms evolving in the water column, here neglected, and likely affecting the estuarine behaviour. Sediment characterization and dynamics also should be explored in detail, considering processes as flocculation, demonstrated to be of great importance for the MR estuary [74]. A quantitative assessment of sediment loads, as well as an understanding of the dynamic of suspended sediment transfer from lands to water courses, is fundamental for the design of an integrated water and soil management system. Furthermore, in the near future, the impacts of climate change will certainly affect the studied dynamics. Estuarine areas are subject to the combined action of riverine and sea forcing and will experience the amplified effects of both river discharges and sea storms due to the increase in frequency and intensity of extreme events. Therefore, further analyses are needed to assess the influence of climate change scenarios on the hydro-morphodynamics evolving at river mouths.

Bibliography

[1] E.J. Anthony. "Wave influence in the construction, shaping and destruction of river deltas: A review". In: *Marine Geology* 361 (2015), pp. 53–78. DOI: https://doi.org/10.1016/j.margeo.2014.12.004.

[2] N.E.M. Asselman. "Fitting and interpretation of sediment rating curves". In: *Journal of hydrology* 234.3-4 (2000), pp. 228–248. DOI: https://doi.org/10.1016/S0022-1694(00)00253-5.

[3] X. Bertin and M. Olabarrieta. "Relevance of infragravity waves in a wave-dominated inlet". In: *Journal of Geophysical Research: Oceans* 121.8 (2016), pp. 5418–5435. DOI: https://doi.org/10.1002/2015JC011444.

[4] J.P. Bhattacharya and L. Giosan. "Wave-influenced deltas: Geomorphological implications for facies reconstruction". In: *Sedimentology* 50.1 (2003), pp. 187–210. DOI: https://doi.org/10.1046/j.1365-3091.2003.00545.x.

[5] N.R.R.C. Booij, R.C. Ris, and L.H. Holthuijsen. "A third-generation wave model for coastal regions: 1. Model description and validation". In: *Journal of geophysical research: Oceans* 104.C4 (1999), pp. 7649–7666. DOI: https://doi.org/10.1029/98JC02622.

[6] V.E. Brando et al. "High-resolution satellite turbidity and sea surface temperature observations of river plume interactions during a significant flood event". In: *Ocean Science* 11.6 (2015), pp. 909–920. DOI: https://doi.org/10.5194/os-11-909-2015.

[7] M. Brocchini. "Wave-forced dynamics in the nearshore river mouths, and swash zones". In: *Earth Surface Processes and Landforms* 45.1 (2020), pp. 75–95. DOI: https://doi.org/10.1002/esp.4699.

[8] M. Brocchini et al. "Comparison between the wintertime and summertime dynamics of the Misa River estuary". In: *Marine Geology* 385 (2017), pp. 27–40. DOI: https://doi.org/10.1016/j.margeo.2016.12.005.

[9] A. Canestrelli et al. "Importance of frictional effects and jet instability on the morphodynamics of river mouth bars and levees". In: *Journal of Geophysical Research: Oceans* 119.1 (2014), pp. 509–522. DOI: https://doi.org/10.1002/2013JC009312.

[10] B.J. Choi and J.L. Wilkin. "The effect of wind on the dispersal of the Hudson River plume". In: *Journal of Physical Oceanography* 37.7 (2007), pp. 1878–1897. DOI: https://doi.org/10.1175/JPO3081.1.

[11] R. Cyriac et al. "Wind and tide effects on the Choctawhatchee Bay plume and implications for surface transport at Destin Inlet". In: *Regional studies in marine science* 35 (2020), p. 101131. DOI: https://doi.org/10.1016/j.rsma.2020.101131.

[12] R.W. Dalrymple and K. Choi. "Morphologic and facies trends through the fluvial–marine transition in tide-dominated depositional systems: a schematic framework for environmental and sequence-stratigraphic interpretation". In: *Earth-Science Reviews* 81.3-4 (2007), pp. 135–174. DOI: https://doi.org/10.1016/j.earscirev.2006.10.002.

[13] A.M. De Girolamo, G. Pappagallo, and A. Lo Porto. "Temporal variability of suspended sediment transport and rating curves in a Mediterranean river basin: The Celone (SE Italy)". In: *Catena* 128 (2015), pp. 135–143. DOI: https://doi.org/10.1016/j.catena.2014.09.020.

[14] Deltares. *Delft3D-Flow. Simulation of multi-dimensional hydrodynamic flows and transport phenomena, including sediments. User Manual*. 2022.

[15] Deltares. *Delft3D-Wave. Simulation of short-crested waves with SWAN. User Manual*. 2022.

[16] Consorzio di Bonifica delle Marche. *Dinamica della sedimentazione marina e impatto sulla costa.pdf*. 2020.

[17] D.A. Edmonds and R.L. Slingerland. "Mechanics of river mouth bar formation: Implications for the morphodynamics of delta distributary networks". In: *Journal of Geophysical Research: Earth Surface* 112.F2 (2007). DOI: https://doi.org/10.1029/2006JF000574.

[18] S. Fagherazzi et al. "Dynamics of river mouth deposits". In: *Reviews of Geophysics* 53.3 (2015), pp. 642–672. DOI: https://doi.org/10.1002/2014RG000451.

[19] F. Falcini et al. "Hydrodynamic and suspended sediment transport controls on river mouth morphology". In: *Journal of Geophysical Research: Earth Surface* 119.1 (2014), pp. 1–11. DOI: https://doi.org/10.1002/2013jf002831.

[20] P. Favali et al. "The 1930 earthquake and the town of Senigallia (Central Italy): an approach to seismic risk evaluation". In: *Annals of Geophysics* 38.5-6 (1995).

[21] D.A. Fong and W.R. Geyer. "Response of a river plume during an upwelling favorable wind event". In: *Journal of Geophysical Research: Oceans* 106.C1 (2001), pp. 1067–1084. DOI: https://doi.org/10.1029/2000JC900134.

[22] A.F. Frangi et al. "Multiscale vessel enhancement filtering". In: *International conference on medical image computing and computer-assisted intervention*. Springer. 1998, pp. 130–137. DOI: https://doi.org/10.1007/BFb0056195.

[23] M. Frignani et al. "Fine-sediment mass balance in the western Adriatic continental shelf over a century time scale". In: *Marine Geology* 222 (2005), pp. 113–133. DOI: https://doi.org/10.1016/j.margeo.2005.06.016.

[24] R.W. Garvine. "A dynamical system for classifying buoyant coastal discharges". In: *Continental Shelf Research* 15.13 (1995), pp. 1585–1596. DOI: https://doi.org/10.1016/0278-4343(94)00065-U.

[25] C.K. Harris et al. "Sediment dispersal in the northwestern Adriatic Sea". In: *Journal of Geophysical Research: Oceans* 113.C11 (2008). DOI: https://doi.org/10.1029/2006JC003868.

[26] R. Hartley and A. Zisserman. *Multiple view geometry in computer vision*. Cambridge university press, 2003. DOI: https://doi.org/10.1017/CBO9780511811685.

[27] K. Hasselmann et al. "Measurements of wind-wave growth and swell decay during the Joint North Sea Wave Project (JONSWAP)." In: *Ergaenzungsheft zur Deutschen Hydrographischen Zeitschrift, Reihe A* 12 (1973). DOI: https://hdl.handle.net/21.11116/0000-0007-DD3C-E.

[28] M.O. Hayes. "General morphology and sediment patterns in tidal inlets". In: *Sedimentary geology* 26.1-3 (1980), pp. 139–156. DOI: https://doi.org/10.1016/0037-0738(80)90009-3.

[29] B. Henderson-Sellers. "The dependence of surface velocity in water bodies on wind velocity and latitude". In: *Applied mathematical modelling* 12.2 (1988), pp. 202–203. DOI: https://doi.org/10.1016/0307-904X(88)90012-1.

[30] R.D. Hetland. "The effects of mixing and spreading on density in near-field river plumes". In: *Dynamics of Atmospheres and Oceans* 49.1 (2010), pp. 37–53. DOI: https://doi.org/10.1016/j.dynatmoce.2008.11.003.

[31] J. Heyman. "TracTrac: a fast multi-object tracking algorithm for motion estimation". In: *Computers & Geosciences* 128 (2019), pp. 11–18. DOI: https://doi.org/10.1016/j.cageo.2019.03.007.

[32] R. Holman and M.C. Haller. "Remote sensing of the nearshore". In: *Annual review of marine science* 5 (2013), pp. 95–113. DOI: 10.1146/annurev-marine-121211-172408.

[33] R. Holman, N. Plant, and T. Holland. "cBathy: A robust algorithm for estimating nearshore bathymetry". In: *Journal of geophysical research: Oceans* 118.5 (2013), pp. 2595–2609. DOI: https://doi.org/10.1002/jgrc.20199.

[34] R. A Holman and J. Stanley. "The history and technical capabilities of Argus". In: *Coastal engineering* 54.6-7 (2007), pp. 477–491. DOI: https://doi.org/10.1016/j.coastaleng.2007.01.003.

[35] T. Janke, R. Schwarze, and K. Bauer. "Part2track: a matlab package for double frame and time resolved particle tracking velocimetry". In: *SoftwareX* 11 (2020), p. 100413. DOI: https://doi.org/10.1016/j.softx.2020.100413.

[36] C.D. Janzen and K.C. Wong. "Wind-forced dynamics at the estuary-shelf interface of a large coastal plain estuary". In: *Journal of Geophysical Research: Oceans* 107.C10 (2002), pp. 2–1. DOI: https://doi.org/10.1029/2001JC000959.

[37] M.J. Jolley et al. "Considerations when applying large-scale PIV and PTV for determining diver flow velocity". In: *Frontiers in Water* 3 (2021), p. 709269. DOI: https://doi.org/10.3389/frwa.2021.709269.

[38] S.E. Kastner, A.R. Horner-Devine, and J.M. Thomson. "A conceptual model of a river plume in the surf zone". In: *Journal of Geophysical Research: Oceans* 124.11 (2019), pp. 8060–8078. DOI: https://doi.org/10.1029/2019JC015510.

[39] K. Kombiadou and Y.N. Krestenitis. "Fine sediment transport model for river influenced microtidal shelf seas with application to the Thermaikos Gulf (NW Aegean Sea)". In: *Continental Shelf Research* 36 (2012), pp. 41–62. DOI: https://doi.org/10.1016/j.csr.2012.01.009.

[40] G. Korres, M. Ravdas, and A. Zacharioudaki. "Mediterranean sea waves analysis and forecast (CMEMS MED-Waves)". In: (2019). DOI: https://doi.org/10.25423/CMCC/MEDSEA_ANALYSIS_FORECAST_WAV_006_017.

[41] P.T. Lan et al. "Application of Remote Sensing and GIS technology for monitoring coastal changes in estuary area of the Red river system, Vietnam". In: *Journal of the Korean Society of Surveying, Geodesy, Photogrammetry and Cartography* 31.6_2 (2013), pp. 529–538. DOI: https://doi.org/10.7848/ksgpc.2013.31.6-2.529.

[42] S.A. Lebedev et al. "On a relationship between the river runoff and the river plume area in the northeastern Black Sea". In: *International Journal of Remote Sensing* 41.15 (2020), pp. 5806–5818. DOI: https://doi.org/10.1080/01431161.2019.1685723.

[43] H.J. Lee and K.K. Liu. "Tidal effects on Changjiang plume dispersal in the East China Sea". In: *Journal of Marine Science and Technology* 21.3 (2013), p. 13. DOI: 10.6119/JMST-013-0207-1.

[44] G.R. Lesser et al. "Development and validation of a three-dimensional morphological model". In: *Coastal engineering* 51.8-9 (2004), pp. 883–915. DOI: https://doi.org/10.1016/j.coastaleng.2004.07.014.

[45] Y. Liu et al. "Evaluation of a coastal ocean circulation model for the Columbia River plume in summer 2004". In: *Journal of Geophysical Research: Oceans* 114.C2 (2009). DOI: https://doi.org/10.1029/2008JC004929.

[46] N.A. Malik, T.h. Dracos, and D.A. Papantoniou. "Particle tracking velocimetry in three-dimensional flows". In: *Experiments in fluids* 15.4 (1993), pp. 279–294. DOI: https://doi.org/10.1007/BF00223406.

[47] Aquater - Regione Marche. *Studio Generale per la difesa delle coste. Prima fase. Vol. II: rapporto di settore.* 1982.

[48] Regione Marche. *Assetto di progetto media e bassa valle del fiume Misa*. 2016. URL: https://www.regione.marche.it/Portals/0/Paesaggio_Territorio_Urbanistica/AdB/PAIMarche/DelComIst/allegati/del160325_67_ElaboratoA.pdf.

[49] G. Masselink and A.D. Short. "The effect of tide range on beach morphodynamics and morphology: a conceptual beach model". In: *Journal of coastal research* (1993), pp. 785–800. DOI: https://www.jstor.org/stable/4298129.

[50] L. Melito et al. "Hydrodynamics at a microtidal inlet: Analysis of propagation of the main wave components". In: *Estuarine, Coastal and Shelf Science* 235 (2020), p. 106603. DOI: https://doi.org/10.1016/j.ecss.2020.106603.

[51] L. Melito et al. "Waves and Currents at a River Mouth: The Role of Macrovortices, Sub-Grid Turbulence and Seabed Friction". In: *Water* 10.5 (2018), p. 550. DOI: https://doi.org/10.3390/w10050550.

[52] M. Mestres, J.P. Sierra, and A. Sánchez-Arcilla. "Factors influencing the spreading of a low-discharge river plume". In: *Continental Shelf Research* 27.16 (2007), pp. 2116–2134. DOI: https://doi.org/10.1016/j.csr.2007.05.008.

[53] V.N. Mikhailov. "Hydrology and formation of river mouth bars". In: *Problems of the Humid Tropical Zone Deltas* 1 (1966), pp. 59–64.

[54] J.D. Milliman and J.P. Syvitski. "Geomorphic/tectonic control of sediment discharge to the ocean: the importance of small mountainous rivers". In: *The journal of Geology* 100.5 (1992), pp. 525–544. DOI: https://doi.org/10.1086/629606.

[55] B. Mohamed et al. "Inter-annual variability and trends of sea level and sea surface temperature in the Mediterranean Sea over the last 25 years". In: *Pure and Applied Geophysics* 176.8 (2019), pp. 3787–3810. DOI: https://doi.org/10.1007/s00024-019-02156-w.

[56] D. Morichon et al. "Using a shore-based video system to hourly monitor storm water plumes (Adour River, Bay of Biscay)". In: *Journal of Coastal Research* 24 (10024) (2008), pp. 133–140. DOI: https://doi.org/10.2112/06-0705.1.

[57] W. Nardin and S. Fagherazzi. "The effect of wind waves on the development of river mouth bars". In: *Geophysical research letters* 39.12 (2012). DOI: https://doi.org/10.1029/2012GL051788.

[58] W. Nardin et al. "Growth of river mouth bars in sheltered bays in the presence of frontal waves". In: *Journal of Geophysical Research: Earth Surface* 118.2 (2013), pp. 872–886. DOI: https://doi.org/10.1002/jgrf.20057.

[59] J.H. Nienhuis, A.D. Ashton, and L. Giosan. "What makes a delta wave-dominated?" In: *Geology* 43.6 (2015), pp. 511–514. DOI: https://doi.org/10.1130/G36518.1.

[60] M. Olabarrieta, W.R. Geyer, and N. Kumar. "The role of morphology and wave-current interaction at tidal inlets: An idealized modeling analysis". In: *Journal of Geophysical Research: Oceans* 119.12 (2014), pp. 8818–8837. DOI: https://doi.org/10.1002/2014JC010191.

[61] A. Osadchiev and R. Sedakov. "Spreading dynamics of small river plumes off the northeastern coast of the Black Sea observed by Landsat 8 and Sentinel-2". In: *Remote Sensing of Environment* 221 (2019), pp. 522–533. DOI: https://doi.org/10.1016/j.rse.2018.11.043.

[62] A. Osadchiev et al. "Spatial structure, short-temporal variability, and dynamical features of small river plumes as observed by aerial drones: Case study of the Kodor and Bzyp river plumes". In: *Remote Sensing* 12.18 (2020), p. 3079. DOI: https://doi.org/10.3390/rs12183079.

[63] A.A. Osadchiev and P.O. Zavialov. "Structure and dynamics of plumes generated by small rivers". In: *Estuaries and Coastal Zones: Dynamics and Response to Environmental Changes* 87843 (2019), pp. 125–144. DOI: https://dx.doi.org/10.5772/intechopen.87843.

[64] C.E. Ostrander et al. “Temporal and spatial variability of freshwater plumes in a semienclosed estuarine–bay system”. In: *Estuaries and Coasts* 31.1 (2008), pp. 192–203. DOI: https://doi.org/10.1007/s12237-007-9001-z.

[65] N. Otsu. “A threshold selection method from gray-level histograms”. In: *IEEE transactions on systems, man, and cybernetics* 9.1 (1979), pp. 62–66.

[66] L. Parlagreco et al. “Monitoring for coastal resilience: preliminary data from five italian sandy beaches”. In: *Sensors* 19.8 (2019), p. 1854. DOI: https://doi.org/10.3390/s19081854.

[67] E. Partheniades. “Erosion and deposition of cohesive soils”. In: *Journal of the Hydraulics Division* 91.1 (1965), pp. 105–139. DOI: https://doi.org/10.1061/JYCEAJ.0001165.

[68] E. Perugini. “The application of video-monitoring data to understand coastal and estuarine processes”. PhD thesis. Università Politecnica delle Marche, 2019. DOI: http://hdl.handle.net/11566/263695.

[69] E. Perugini et al. “A new video monitoring station along the adriatic coast”. In: *Atti del XXXVI Convegno Nazionale di Idraulica e Costruzioni Idrauliche* (2018).

[70] E. Perugini et al. “Linear depth inversion sensitivity to wave viewing angle using synthetic optical video”. In: *Coastal Engineering* 152 (2019), p. 103535. DOI: https://doi.org/10.1016/j.coastaleng.2019.103535.

[71] C. Pianca, R. Holman, and E. Siegle. “Mobility of meso-scale morphology on a microtidal ebb delta measured using remote sensing”. In: *Marine Geology* 357 (2014), pp. 334–343. DOI: https://doi.org/10.1016/j.margeo.2014.09.045.

[72] B. Pigorini. “Sources and dispersion of recent sediments of the Adriatic Sea”. In: *Marine Geology* 6.3 (1968), pp. 187–229. DOI: https://doi.org/10.1016/0025-3227(68)90031-5.

[73] A. Piñones et al. “Wind-induced diurnal variability in river plume motion”. In: *Estuarine, Coastal and Shelf Science* 65.3 (2005), pp. 513–525. DOI: https://doi.org/10.1016/j.ecss.2005.06.016.

[74] M. Postacchini et al. “A storm driven turbidity maximum in a microtidal estuary.” In: *Estuarine, Coastal and Shelf Science* (2023), p. 108350. DOI: https://doi.org/10.1016/j.ecss.2023.108350.

[75] M. Postacchini et al. “Medium-term dynamics of a middle Adriatic barred beach”. In: *Ocean Science* 13.5 (2017), pp. 719–734. DOI: https://doi.org/10.5194/os-13-719-2017.

[76] M. Ravaioli et al. “La rete scientifica italiana di siti fissi per l’osservazione del mare – IFON”. In: *CNR Pubblicazioni 2017* (2017).

[77] A.R. Rodriguez, S.N. Giddings, and N. Kumar. “Impacts of nearshore wave-current interaction on transport and mixing of small-scale buoyant plumes”. In: *Geophysical Research Letters* 45.16 (2018), pp. 8379–8389. DOI: https://doi.org/10.1029/2018GL078328.

[78] J.A. Roelvink and G.K.F.M. Van Banning. “Design and development of DELFT3D and application to coastal morphodynamics”. In: *Oceanographic Literature Review* 11.42 (1995), p. 925.

[79] G. Rolandi et al. “The 79 AD eruption of Somma: The relationship between the date of the eruption and the southeast tephra dispersion”. In: *Journal of Volcanology and Geothermal Research* 169.1-2 (2008), pp. 87–98. DOI: https://doi.org/10.1016/j.jvolgeores.2007.08.020.

[80] A. Ruiz-Reina and A. López-Ruiz. “Short-term river mouth bar development during extreme river discharge events: The role of the phase difference between the peak discharge and the tidal level”. In: *Coastal Engineering* 170 (2021), p. 103982. DOI: https://doi.org/10.1016/j.coastaleng.2021.103982.

[81] J.H. Simpson et al. “Periodic stratification in the rhine ROFI in the north-sea”. In: *Oceanologica Acta* 16.1 (1993), pp. 23–32. DOI: https://archimer.ifremer.fr/doc/00099/21050/.

[82] E. Soosaar et al. “River bulge evolution and dynamics in a non-tidal sea–Daugava River plume in the Gulf of Riga, Baltic Sea”. In: *Ocean Science* 12.2 (2016), pp. 417–432. DOI: https://doi.org/10.5194/os-12-417-2016.

[83] R.J. Uncles, J.A. Stephens, and C. Harris. “Infragravity currents in a small ría: Estuary-amplified coastal edge waves?” In: *Estuarine, Coastal and Shelf Science* 150 (2014), pp. 242–251. DOI: https://doi.org/10.1016/j.ecss.2014.04.019.

[84] A. Valle-Levinson. *Contemporary issues in estuarine physics*. Cambridge University Press, 2010. DOI: https://doi.org/10.1017/CBO9780511676567.

[85] T.S. van den Bremer and Ø. Breivik. “Stokes drift”. In: *Philosophical Transactions of the Royal Society A: Mathematical, Physical and Engineering Sciences* 376.2111 (2018), p. 20170104. DOI: https://doi.org/10.1098/rsta.2017.0104.

[86] M. van der Wegen. *Modeling morphodynamic evolution in alluvial estuaries*. CRC Press, 2010.

[87] L.C. van Rijn et al. *Principles of sediment transport in rivers, estuaries and coastal seas*. Aqua publications Amsterdam, 1993.

[88] L.C. van Rijn et al. “The predictability of cross-shore bed evolution of sandy beaches at the time scale of storms and seasons using process-based profile models”. In: *Coastal Engineering* 47.3 (2003), pp. 295–327. DOI: https://doi.org/10.1016/S0378-3839(02)00120-5.

[89] J.A. Warrick et al. “River plume patterns and dynamics within the Southern California Bight”. In: *Continental Shelf Research* 27.19 (2007), pp. 2427–2448. DOI: https://doi.org/10.1016/j.csr.2007.06.015.

[90] J. Westerweel and F. Scarano. “Universal outlier detection for PIV data”. In: *Experiments in fluids* 39.6 (2005), pp. 1096–1100. DOI: https://doi.org/10.1007/s00348-005-0016-6.

[91] M.M. Whitney and R.W. Garvine. “Wind influence on a coastal buoyant outflow”. In: *Journal of Geophysical Research: Oceans* 110.C3 (2005). DOI: https://doi.org/10.1029/2003JC002261.

[92] M. Witting, C. Wehmeyer, and H.D. Niemeyer. “Medium-term morphodynamic modeling of mixed mud and sand in the tidal basin Jadebusen.” In: *Coastal Engineering Proceedings* 32 (2010), pp. 65–65. DOI: https://doi.org/10.9753/icce.v32.sediment.65.

[93] L.D. Wright. “Sediment transport and deposition at river mouths: a synthesis”. In: *Geological Society of America Bulletin* 88.6 (1977), pp. 857–868. DOI: https://doi.org/10.1130/0016-7606(1977)88<857:STADAR>2.0.CO;2.

[94] L.D. Wright, J.M. Coleman, and M.W. Erickson. *Analysis of major river systems and their deltas: Morphologic and process comparisons*. Tech. rep. LOUISIANA STATE UNIV BATON ROUGE COASTAL STUDIES INST, 1974.

[95] A.E. Yankovsky and D.C. Chapman. “A simple theory for the fate of buoyant coastal discharges”. In: *Journal of Physical oceanography* 27.7 (1997), pp. 1386–1401. DOI: https://journals.ametsoc.org/view/journals/phoc/27/7/1520-0485_1997_027_1386_astftf_2.0.co_2.xml.

[96] C. Zarzuelo, A. López-Ruiz, and M. Ortega-Sánchez. “The role of waves and heat exchange in the hydrodynamics of multi-basin bays: the example of Cádiz Bay (Southern Spain)”. In: *Journal of Geophysical Research: Oceans* 126.2 (2021), e2020JC016346. DOI: https://doi.org/10.1029/2020JC016346.

[97] K. Zuiderveld. “Contrast Limited Adaptive Histogram Equalization”. In: *Graphics Gems*. Academic Press, 1994, pp. 474–485. DOI: https://doi.org/10.1016/B978-0-12-336156-1.50061-6.